

POLITECNICO DI TORINO

Master's Degree in Civil Engineering



Master thesis

Ductile-to-brittle transition in fiber-reinforced materials: Effects of dimensional scale and fiber volume ratio

Tutors

Prof. Ing. Alberto CARPINTERI

Dr. Ing. Federico ACCORNERO

Candidate

Luigi ALEDDA

Academic Year 2018-2019

Aknowledge

The industrial support of AZICHEM srl is gratefully acknowledged. Special thanks are due to Roberto Rosignoli, the CTO and R&D Manager of AZICHEM srl.

Abstract

The employment of Fiber Reinforced Concrete (FRC) in the building industry is becoming more and more prominent as numerous research have demonstrate its effectiveness in many structural applications. FRC has been particularly used in structural elements when crack propagation control is of primary importance. The role of fibers is essentially to arrest any advancing cracks and increase the ductility and post-cracking stiffness of the structural element right up to failure, which results in narrowed crack widths and substantially less deformation. The secondary phase provides crack control and improves the fracture toughness of the brittle matrices, by means of a bridging action affecting the matrix macro- and micro-cracks. In the micro-cracked process zone, ahead of the matrix macro-crack, the bridging action affects the propagation and coalescence of the micro-cracks, thus controlling the macro-crack extension. In the wake of the macro-crack, a real stitching action prevents the crack face opening and control the crack growth. This mechanism increases the energy demand for the crack advancement.

Several guidelines and codes for FRC structures are under development in different Countries. Moreover, several models have been recently developed in order to predict the flexural behavior of the FRC. The present Master Thesis focuses on Bridged Crack Model (Carpinteri, 1981). The results of several numerical analyses, and of some experimental campaigns carried out by international research groups, are compared in order to validate the proposed model. In order to enhance the analytical model validation, an experimental campaign on FRC beams in bending has been carried out at Fracture Mechanics Laboratory of Politecnico di Torino during the past months.

In the first part of this work, the Bridged Crack Model is described. This model takes into account both compatibility and equilibrium equations, and it allows to clearly explore the influence of several different parameters in fibre reinforced brittle matrix composites. The problem of a composite rectangular-section beam subjected to bending is analysed. The matrix is elastic-perfectly brittle, whereas the fibres are characterized by a rigid-perfectly plastic law, that can represent either yielding or reinforcement slippage. The value of the moment that produces the fibre plasticization and the one that causes the crack propagation are evaluated. The crack propagation is taken into account assuming an approach based on Linear Elastic Fracture Mechanics, and a review of stress intensity factors formulas is carried out in order to check their influence on the result. Then, the Bridged Crack algorithm is illustrated in detail, and it is utilized in order to perform the present study.

The second part of this thesis consists in a detailed review of the results of several experimental campaigns aimed at studying the effects of fibre reinforcements on the flexural behaviour of full scale concrete beams. Then, these experimental results are used to validate the Bridged Crack Model.

In the third part of this work, the details of the experimental campaign carried out during the past months at Fracture Mechanics Laboratory of Politecnico di Torino, in partnership with AZICHEM srl and FABLAB TORINO, are described in detail. The flexural response

of 24 FRC beams is investigated through Three Point Bending (TPB) tests, varying the beam sizes and the fiber volume fraction in the concrete matrix.

The experimental campaign has been carried out in two different stages. The first stage involves 12 FRC beams made of normal concrete ($R_{ck} = 30 \text{ N/mm}^2$). Three beam sizes have been considered: 5 x 5 x 30 cm; 10 x 10 x 60 cm; 20 x 10 x 120 cm. Three different lengths of steel fiber reinforcement are considered in the first stage: $L_f=1.5 \text{ cm}$; $L_f=3.5 \text{ cm}$; $L_f=5 \text{ cm}$. A specific yield strength equal to 1100 N/mm^2 characterizes these fiber reinforcements, in order to have an efficient control of the cracking process. Fiber reinforcements have been added to the concrete matrix in four different volume fractions: 0.08%; 0.20%; 0.96%; 1.28%.

The second stage of the experimental campaign involves 12 FRC beams made of high performance concrete ($R_{ck} > 120 \text{ N/mm}^2$). Also in this case, three beam sizes have been considered: 5 x 5 x 30 cm; 10 x 10 x 60 cm; 20 x 10 x 120 cm. Brass fiber reinforcements have been adopted in this case. Due to their enhanced high-bonding capability, brass fibers are supposed to increase the load carrying capacity of FRC members. Brass fibers substantially reduce the brittleness of the concrete matrix, and improve its engineering properties, such as tensile, flexural, impact resistance, fatigue, load bearing capacity after cracking, and toughness.

The experimental results show how the effect of the size scale, as predicted by the Bridged Crack Model, is found to be fundamental for the global or local structural behavior of the FRC beams, which can range from ductile to catastrophic simply with the variation of the brittleness number, N_p . The brittleness number is function of the toughness of the matrix, of the yielding or slippage limit of the fiber-reinforcement, of the fiber volume fraction, and of the characteristic structural size. Moreover, the minimum reinforcement condition of the structural FRC element is investigated both theoretically and experimentally: it allows the crack propagation phenomenon to be globally stable, i.e., when the fracturing moment is equal to the ultimate resistance developed by the FRC beam, and it leads to an optimization of the structural components.

Table of contents

Aknowledge	I
Abstract.....	II
Introduction	1
1. Modelling of fiber reinforced materials	2
1.1 Fiber reinforced materials	2
1.2 Review of the models	2
1.3 Bridged crack model.....	3
1.3.1 Geometry and hypotheses	3
1.3.2 Shape functions and stress intensity factor	4
1.3.3 Compliances of a cracked beam element	7
1.3.4 Crack openings	9
1.3.5 Rotation.....	9
1.3.6 Compatibility equation	10
1.3.7 Plastic moments	11
1.3.8 Crack propagation condition.....	12
1.3.9 Forces and bending moment at crack propagation	13
1.3.10 Brittleness number and dimensionless analysis.....	13
1.3.11 Ultimate bending moment	14
1.4 Monotonic loading	15
1.4.1 Crack Length Control Scheme (CLCS)	15
1.4.2 Parametric study	18
1.4.3 Numerical errors.....	22
2. Experimental campaigns critical review	25
2.1 Plizzari experimental work.....	25
2.2.1 Material and experimental setup	25
2.1.2 Results and discussion.....	28
2.2 Carpinteri experimental work.....	31
2.2.1 Material and experimental setup	31
2.2.2 Results and discussion.....	33
2.3 Swamy experimental work.....	37
2.3.1 Material and experimental setup	38
2.3.2 Results and discussion.....	40

2.4 Olivito experimental work.....	41
2.4.1 Material and experimental setup	41
2.4.2 Results and discussion.....	44
2.5 Kang experimental work	47
2.5.1 Material and experimental setup	50
2.5.2 Results and discussion.....	51
3. Experimental validation of the Bridged Crack Model	54
3.1 Material.....	54
3.2 Experimental results and numerical simulations.....	56
3.3 Discussion and conclusions.....	61
3.4 Concluding remarks.....	64
References	66

Introduction

This dissertation deals with the behavior of the fiber reinforced concrete materials subjected to monotonic loads. In particular, the aim of this investigation is to verify if the Bridged Crack Model can be used to analyse a FRC materials.

The first part is focused on the modelling of these materials. In section [1.1] a description of their improved mechanical properties is given and in section [1.2] the different models used to study their behaviour are reviewed. In section [1.3] the Bridged Crack model is chosen to perform the analysis and it is described in detail regarding the problem of monotonic loading. Section [1.4] is about In section the numerical algorithms and the results of the parametric analysis.

The second part presents the results of the bibliographic research performed during this Thesis work. Experimental campaigns aimed at studying the effects of fibre reinforcements on the flexural behaviour of full scale concrete beams are reviewed: Plizzari et al. [2.1]; Carpinteri et al. [2.2]; Swamy et al. [2.3]; Olivito et al. [2.4]; Kang et al. [2.5].

In the third part of this work, the details of the experimental campaign carried out during this Master Thesis, at Fracture Mechanics Laboratory of Politecnico di Torino, are described in detail. In section [3.1] a description of materials and mix design is given and section [3.2] presents the result of the three-point bending tests. Finally, a discussion about the results achieved and the concluding remarks are provided in section [3.3] and [3.4] respectively.

1. Modelling of fiber reinforced materials

In this chapter the characteristics of fiber reinforced materials and the models used for their analysis are illustrated in section [1.1] and [1.2]. Then the Bridged Crack model is chosen to study their behaviour and it is explained in detail in section [1.3] and [1.4].

1.1 Fiber reinforced materials

A composite material is obtained through the combination of two or more different constituents, whose interfaces remain recognizable. The properties of the composite are usually enhanced in comparison with the ones of the initial materials. They are used in many different applications and they are usually optimized to achieve a particular balance of properties for a given range of applications.

From a mechanical point of view, it is possible to distinguish a matrix in which a reinforcement material is spread.

Different classifications of composite materials are possible. One of the most used is that based on the matrix characterization. In this case three different groups are identified: polymer, ceramic and metal matrix composites. Another one is based on the shape of the strengthening phase and it is possible to distinguish three classes: grained composites, fiber reinforced composites and laminar composites.

In this dissertation only the case of fibrous composite with brittle matrix is considered. The presence of fibers improves strength, ductility, cracking resistance and fatigue strength.

Reinforced concrete is a well-known example of this class of composites. The matrix is characterized by low tensile strength and poor fracture toughness, but the presence of reinforcements acts against the nucleation of cracks thanks to their bridging action. At the same time the matrix offers resistance to the corrosion of reinforcements.

1.2 Review of the models

Independently of the matrix, fibrous composites present a common feature: the bridging action exerted by the fibers. This behaviour is the focus of the mechanical models used for the analysis of these materials on the basis of fracture mechanics.

There are several ways to classify the models: for example those based on the fiber type (continuous or discontinuous fibers), on the cracking regime (multiple cracking or single crack), on the crack opening conditions (steady-state or non steady-state cracking), on the matrix properties (perfectly brittle or strain-softening), on the bridging actions (continuous or discontinuous), on the loading condition (tensile loading, compressive loading, bending).

The models based on interface mechanics and fracture mechanics are the most common.

In the first case the focus is on the interface between the matrix and the fibers. The bond is studied with micromechanical models, that sometimes take into account the principle of fracture mechanics too.

The second family can be divided into two types: the Bridged Crack model and the cohesive crack model. They have been unified in a single formulation (Carpinteri, Massabò, 1996) and it has been demonstrated that they predict the same overall behaviour.

The cohesive crack model, in accordance with the ones proposed by Barenblatt (1962) for the analysis of brittle heterogeneous materials and then by Dugdale (1960) for the analysis of ductile materials, replaces the bridging zone by a fictitious crack, where a closing action is present (cohesive law).

On the contrary the Bridged Crack model considers localized closing tractions.

The first model assumes a finite stress field at the crack tip, while in the second case the stress field is singular.

1.3 Bridged crack model

The Bridged Crack model was proposed initially for the case of a monotonic loading applied to beams with a single reinforcement (Carpinteri, 1984). Later it was extended to the case of multiple reinforcements (Carpinteri, Massabò, 1996, 1997) and to the one of cyclic loading with a single reinforcement (Carpinteri, 1984) or two reinforcements (Carpinteri, Puzzi, 2003).

1.3.1 Geometry and hypotheses

The Bridged Crack model considers a fiber reinforced rectangular-section beam subjected to the bending moment M and with an edge crack. The dimensions of the beam (h , b), the initial crack depth a and the position of the fibers c_i are shown in Fig. (1.1). Only the fibers crossing the crack are active and their number is equal to m .

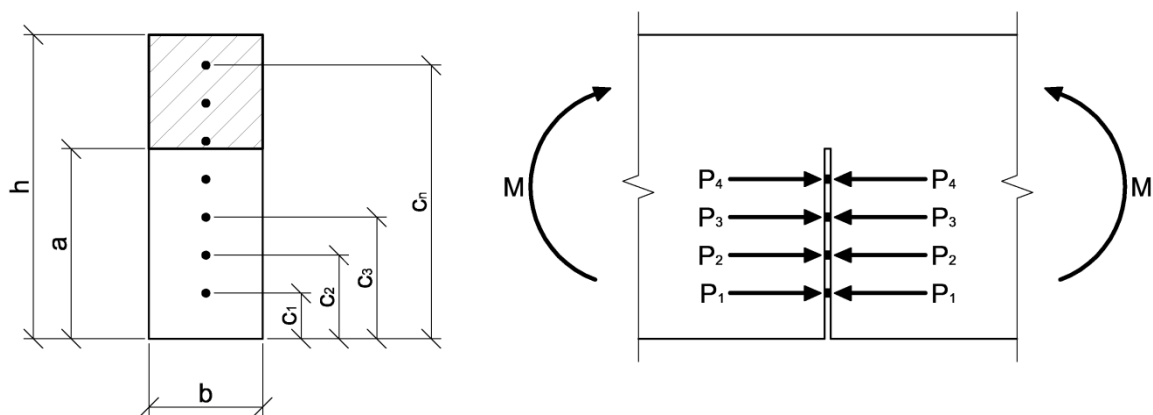


Figure 1.1: Geometry of the fiber reinforced beam

It is possible to define the normalized crack depth, Eq. (1.1), and the normalized position of a generic reinforcement, Eq. (1.2), with respect to the bottom of the beam.

$$\xi = a/h \quad (1.1)$$

$$\zeta_i = c_i/h \quad (1.2)$$

The reinforcements exert a bridging action across the crack described by the forces $P_{P,i}$.

The matrix is assumed elastic-perfectly brittle and it is described by the fracture toughness K_{IC} and by the Young Modulus E , while the reinforcements are considered rigid-perfectly plastic and their ultimate force is equal to $P_{P,i}$. The rigid-perfectly plastic law of the fibers can describe either their slippage or their yielding. In the first case the value of $P_{P,i}$ is related to fibre circumference, d_f , fibre length, l_f , and to frictional bonding force between the matrix and the reinforcement, τ_{max} , according to Eq. (1.3). Where, the peak value of the bond strength in a pull-out failure mode, τ_{max} , is function of the concrete strength, f_{cm} , according to Model Code 2010, Eq. (1.4).

$$P_{P,i} = d_f l_f \tau_{max} \quad (1.3)$$

$$\tau_{max} = 2,5\sqrt{f_{cm}} \quad (1.4)$$

While in the second case it represents the force that makes the fiber plastically flow. This force is proportional to the area of the reinforcement A_i and to the yielding stress $\sigma_{y,i}$ of its material, Eq. (1.5). The same value is assumed both in tension and in compression.

$$P_{P,i} = A_i \sigma_{y,i} \quad (1.5)$$

In other words this means that the elastic deformation of the fiber is disregarded.

The beam is made of a composite material, but its matrix is homogeneous and isotropic if it is considered isolated.

The model takes into account both equilibrium and compatibility equations. If the beam section length vanishes, its compliance is due only to the cracked section. So, it is necessary to evaluate the compliance of a cracked element in order to calculate the openings of the crack and the rotation of the section. The model disregards the contribution to the deformability given by the beam which the cracked section belongs to.

1.3.2 Shape functions and stress intensity factor

In this section the formulas of the stress intensity factor are reported. They are a measure of the singular stress field in the crack tip proximity. They will be needed to calculate the compliances of a cracked element and to take into account the crack propagation based on linear elastic fracture mechanics. Only the crack opening (Mode I) is considered while the problem of the shear and the crack sliding (Mode II) is disregarded.

The stress intensity factors due respectively to the bending moment and to a concentrated force applied on the crack face (Tada, Paris Irwin, 1985) are:

$$K_{IM} = \frac{M}{h^{3/2}b} Y_M(\xi) \quad (1.6)$$

$$K_{IP} = \frac{P}{h^{1/2}b} Y_P(\xi, \zeta_i) \quad (1.7)$$

In the previous equations the shape functions Y_M and Y_P appear. They depend on the crack depth and their value can be found in different stress intensity factors handbook. For example, the shape function for the bending moment Y_M is defined by different authors in various way.

Tada, Paris, Irwin (1985)

$$Y_M(\xi) = \begin{cases} 6(1,99\xi^{0,5} - 2,47\xi^{1,5} + 12,97\xi^{2,5} - 23,17\xi^{3,5} + 24,8\xi^{4,5}) & \xi \leq 0,6 \\ 3,99(1 - \xi)^{-1,5} & \xi > 0,6 \end{cases} \quad (1.8)$$

Wilson (1970) ($1/2 \leq \xi \leq 4/5$)

$$Y_M(\xi) = \frac{6\sqrt{\pi}}{(1 - \xi)^{3/2}} c \quad (1.9)$$

$$c = 0,375 \quad (1.10)$$

Paris, Sih (1965) ($\xi < 1$)

$$Y_M(\xi) = \frac{6\sqrt{\pi}}{(1 - \xi)^{3/2}} c \quad (1.11)$$

$$c = \frac{2(\pi - 2)}{3(\pi^2 - 8)} \quad (1.12)$$

Sinclair, Messner, Meda (1996) ($\xi < 1$)

$$Y_M(\xi) = \frac{6\sqrt{\pi}}{(1 - \xi)^{3/2}} c \quad (1.13)$$

$$c = 0,375 + \frac{0,108}{10^4} \left[e^{24\left(\frac{4}{3}\xi - 1\right)} - 1 \right] \quad (1.14)$$

Guinea, Pastor, Planas, Elices (1998) ($\xi < 1$)

$$Y_M(\xi) = \frac{6\sqrt{\xi}}{(1 - \xi)^{3/2}(1 + 3\xi)} p_\infty \quad (1.15)$$

$$p_\infty = 1,99 + 0,83\xi - 0,31\xi^2 + 0,14\xi^3 \quad (1.16)$$

A comparison between Eq. (1.8) and (1.15) is shown in Fig. (1.2). It can be noticed that the values of the shape functions are almost identical for $\xi > 0,2$ and in any case the little difference does not affect the numerical results of the analysis. The shape function Y_M has a vertical asymptote at $\xi = 1$.

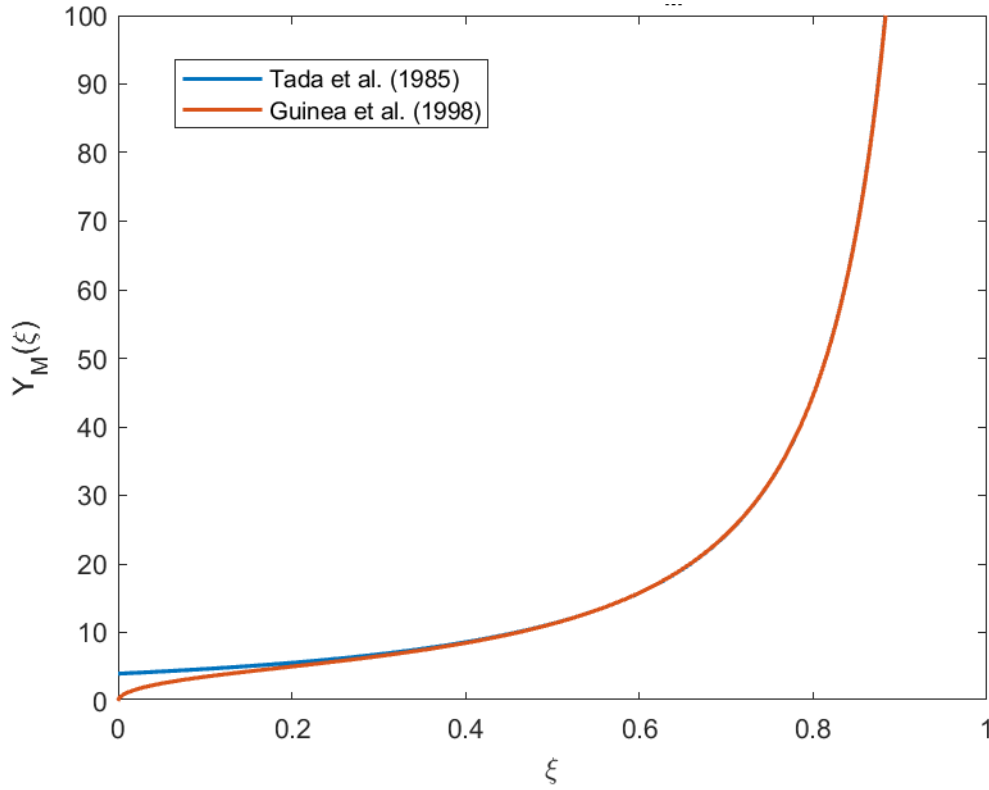


Figure 1. 2: Shape function $Y_M(\xi)$ according to Eq. (1.8) and (1.15)

The other equation graphs are very similar to the one of Eq. (1.8), even if they are valid only for a limited range of crack depth values. All the results shown in the present analysis are attained using Eq. (1.15). Eq. (1.8) should not be used because of its discontinuity in $\xi = 0,6$, that gives rise to numerical problems.

Regarding the shape function for the load Y_p only the following expression is considered in the analysis (Tada, Paris, Irwin, 1985):

$$Y_p(\xi, \zeta_i) = \frac{2}{\sqrt{\pi\xi}} \frac{1}{(1-\xi)^{1,5} \sqrt{1 - \left(\frac{\zeta_i}{\xi}\right)^2}} G(\xi, \zeta_i) \quad \xi \geq \zeta_i \quad (1.17)$$

$$G(\xi, \zeta_i) = g_1(\xi) + g_2(\xi) \frac{\zeta_i}{\xi} + g_3(\xi) \left(\frac{\zeta_i}{\xi}\right)^2 + g_4(\xi) \left(\frac{\zeta_i}{\xi}\right)^3 \quad (1.18)$$

$$g_1(\xi) = 0,46 + 3,06\xi + 0,84(1-\xi)^5 + 0,66\xi^2(1-\xi)^2 \quad (1.19)$$

$$g_2(\xi) = -3,52\xi^2 \quad (1.20)$$

$$g_3(\xi) = 6,17 - 28,22\xi + 34,54\xi^2 - 14,39\xi^3 - (1-\xi)^{1,5} - 5,88(1-\xi)^5 - 2,64\xi^2(1-\xi)^2 \quad (1.21)$$

$$g_4(\xi) = -6,63 + 25,16\xi - 31,04\xi^2 + 14,41\xi^3 + 2(1-\xi)^{1,5} + 5,04(1-\xi)^5 + 1,98\xi^2(1-\xi)^2 \quad (1.22)$$

In Fig. (1.3) the graph of Y_P is shown for different positions of the fiber. It is characterized by two vertical asymptotes: one located at the position of the fiber and another one located at $\xi = 1$.

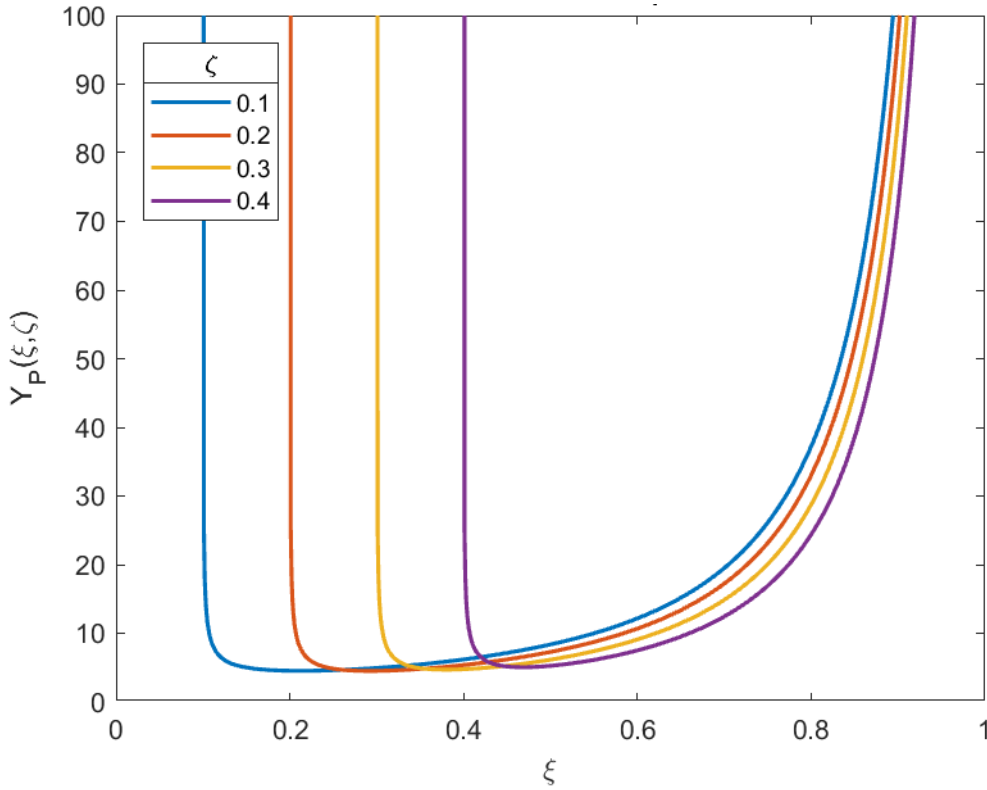


Figure 1. 3: Shape function $Y_P(\xi, \zeta_i)$ according to Eq. (1.17)

1.3.3 Compliances of a cracked beam element

If the beam has only one fiber, the rotation ϕ and the crack opening w are connected to the bending moment M and the reinforcement reaction P by the compliance matrix.

$$\begin{Bmatrix} \phi \\ w \end{Bmatrix} = \begin{bmatrix} \lambda_{MM} & \lambda_{MP} \\ \lambda_{PM} & \lambda_{PP} \end{bmatrix} \begin{Bmatrix} M \\ P \end{Bmatrix} \quad (1.23)$$

The matrix in Eq. (1.23) is symmetric because $\lambda_{MP} = \lambda_{PM}$ for the Betty's theorem.

By using Clapeyron's theorem and superposition principle it is possible to evaluate the energy variation.

$$-\Delta W = \frac{1}{2} M \phi + \frac{1}{2} P w \quad (1.24)$$

$$-\Delta W = \frac{1}{2} \lambda_{MM} M^2 + \frac{1}{2} \lambda_{PP} P^2 + \lambda_{MP} M P \quad (1.25)$$

Then, the strain energy release rate and the relation between G_I and K_I are introduced.

$$G_I = -\frac{dW}{dA} \quad (1.26)$$

$$\mathcal{G}_I = \frac{K_I^2}{E} \quad (1.27)$$

Now the energy variation can be expressed by:

$$\begin{aligned} -\Delta W &= \int_0^a \mathcal{G}_I b \, dh = \int_0^a \frac{K_I^2}{E} b \, dh = \int_0^a \frac{(K_{IM} + K_{IP})^2}{E} b \, dh \\ &= \int_0^a \frac{K_{IM}^2}{E} b \, dh + \int_0^a \frac{K_{IP}^2}{E} b \, dh + 2 \int_0^a \frac{K_{IM}K_{IP}}{E} b \, dh \end{aligned} \quad (1.28)$$

Then using Eq. (1.6) and Eq. (1.7)

$$-\Delta W = \frac{M^2}{b^2 h E} \int_0^\xi Y_M^2(\xi) d\xi + \frac{P^2}{h E} \int_0^\xi Y_P^2(\xi) d\xi + \frac{2MP}{bh E} \int_0^\xi Y_M(\xi) Y_P(\xi) d\xi \quad (1.29)$$

The expressions of the compliances are attained by comparing Eq.(1.25) and Eq. (1.29) and using the identity principle of polynomials.

$$\lambda_{MM} = \frac{2}{E h^2 b} \int_0^\xi Y_M^2(\xi) d\xi \quad (1.30)$$

$$\lambda_{MP} = \frac{2}{hb E} \int_0^\xi Y_P(\xi) Y_M(\xi) d\xi \quad (1.31)$$

$$\lambda_{PP} = \frac{2}{b E} \int_0^\xi Y_P^2(\xi) d\xi \quad (1.32)$$

In the case of more than one fiber the following relations can be obtained (Massabò, 1997).

$$\lambda_{MM} = \frac{2}{E h^2 b} \int_0^\xi Y_M^2(\xi) d\xi \quad (1.33)$$

$$\lambda_{iM} = \frac{2}{hb E} \int_{\zeta_i}^\xi Y_P(\xi, \zeta_i) Y_M(\xi) d\xi \quad (1.34)$$

$$\lambda_{ij} = \frac{2}{b E} \int_{\max(\zeta_i, \zeta_j)}^\xi Y_P(\xi, \zeta_i) Y_P(\xi, \zeta_j) d\xi \quad (1.35)$$

The integral of Eq. (1.34) and Eq. (1.35) are improper because the integrand has a singularity at the lower bound of integration. In the first case the singularity is only apparent, while in the second it is not removable when $i = j$. However, in this second case it is possible to consider a distribution of stresses instead of a concentrated force to model the fiber action (Massabò, 1997) achieving the following equation:

$$\lambda_{ii} = \frac{2}{b E} \int_{\zeta_i + \delta}^\xi Y_P^2(\xi, \zeta_i) d\xi \quad (1.36)$$

Where δ is a cut-off distance that can be assumed equal to 10^{-5} .

1.3.4 Crack openings

The crack openings at the level of the reinforcements can be evaluated by using the superposition principle: it is necessary to sum the contribution due to the bending moment and the one due to the concentrated forces applied on the crack faces [Eq. (1.37)].

$$w_i = \lambda_{iM}M - \sum_{j=1}^m \lambda_{ij}P_j \quad (1.37)$$

In the previous equation the minus sign is related to the fact that a positive bending moment tries to open the crack, while a positive force tries to close the crack. The compliance λ_{iM} is the displacement at the fiber level i due to a unit bending moment, while the compliance λ_{ij} is the displacement at the fiber level i due to a unit force applied at the fiber level j .

Equation (1.37) can be rewritten in matrix form:

$$\{w\} = \{\lambda_M\}M - [\lambda]\{P\} \quad (1.38)$$

where $\{w\}$ is the vector of the crack openings at the level of the reinforcements, $\{\lambda_M\}$ is the vector of the compliance λ_{iM} , $[\lambda]$ is the symmetric square matrix of the compliance λ_{ij} and $\{P\}$ is the vector of the fiber reactions.

It is also possible to evaluate the crack opening at the generic level ζ , Eq. (1.39), and it can be useful to draw the entire profile of the crack faces.

$$w(\zeta) = \lambda_{\zeta M}M - \sum_{j=1}^m \lambda_{\zeta j}P_j \quad (1.39)$$

1.3.5 Rotation

The rotation of the section is calculated in the same way as the crack openings:

$$\phi = \lambda_{MM}M - \sum_{j=1}^m \lambda_{jM}P_j \quad (1.40)$$

where the compliance λ_{MM} is the rotation due to a unit bending moment, while the compliance λ_{jM} is the rotation due to a unit force applied at the fiber level j .

Again Eq. (1.40) can be written in matrix form:

$$\phi = \lambda_{MM}M - \{\lambda_M\}^T\{P\} \quad (1.41)$$

where $\{\lambda_M\}$ is the vector of the compliance λ_{jM} and $\{P\}$ is the vector of the fiber reactions.

1.3.6 Compatibility equation

The problem is statically indeterminate because the forces in the fibers are unknown and so the compatibility equation is introduced to solve it.

Because of the hypothesis of rigid-perfectly plastic law of the fibers, the crack openings at their level remain equal to zero until the ultimate force $P_{P,i}$ is reached in one of them. These m conditions are expressed by:

$$\{w\} = \{\lambda_M\}M - [\lambda]\{P\} = \{0\} \quad (1.42)$$

If the bending moment is known, the reactions in the reinforcements $\{P\}$ can be calculated by solving the linear system:

$$[\lambda]\{P\} = \{\lambda_M\}M \quad (1.43)$$

When a generic fiber i reaches its ultimate force, the crack openings at its level starts increasing and the previous compatibility equation is not valid any more. The force in the fiber becomes known and equal to $P_{P,i}$, while the corresponding opening displacement w_i becomes unknown. However, the compatibility equation is valid for the $m - 1$ fibers, that are not yielded, and also the number of static unknowns is equal to $m - 1$. So, it is possible to solve again the problem whose size is reduced by one.

Considering a generic situation and naming f (free displacements) the plasticized fibers and c (constrained displacements) the elastic fibers, it is possible to split the problem in two parts: one statically indeterminate and one statically determinate.

$$\begin{Bmatrix} w_f \\ w_c \end{Bmatrix} = \begin{Bmatrix} \lambda_{Mf} \\ \lambda_{Mc} \end{Bmatrix} M - \begin{bmatrix} \lambda_{ff} & \lambda_{fc} \\ \lambda_{cf} & \lambda_{cc} \end{bmatrix} \begin{Bmatrix} P_f \\ P_c \end{Bmatrix} \quad (1.44)$$

The displacements of the elastic fibers $\{w_c\}$ and the ultimate forces of the yielded fibers $\{P_f\}$ are known and equal respectively to $\{0\}$ and $\{P_{P,f}\}$.

If the second equation of (1.44) is considered:

$$\{w_c\} = \{\lambda_{Mc}\}M - ([\lambda_{cf}]\{P_{P,f}\} + [\lambda_{cc}]\{P_c\}) = \{0\} \quad (1.45)$$

it is possible to find the value of the forces in the elastic fibers $\{P_c\}$ by solving the linear system:

$$[\lambda_{cc}]\{P_c\} = \{\lambda_{Mc}\}M - [\lambda_{cf}]\{P_{P,f}\} \quad (1.46)$$

Then, considering the first equation of (1.44) with the conditions $\{P_f\} = \{P_{P,f}\}$ and $\{w_c\} = \{0\}$ and substituting the value of $\{P_c\}$ from (1.46), it is possible to compute the displacements of the plasticized fibers $\{w_f\}$.

$$\{w_f\} = \{\lambda_{Mf}\}M - ([\lambda_{ff}]\{P_{P,f}\} + [\lambda_{fc}]\{P_c\}) \quad (1.47)$$

In any case it is necessary to know the plasticized reinforcements a priori and this means that the problem should be solved step by step. The procedure used in this analysis will be explained in the section of the numerical algorithm.

From an overall point of view the problem presents $2m$ unknowns in a first stage: m static unknowns, the reactions $\{P\}$, and m kinematic unknowns, the displacements $\{w\}$. Thanks to the m compatibility conditions all the kinematic unknowns become known and so the problem can be solved using the m equations of system (1.43). At a subsequent stage characterized by the yielding of one fiber, the number of static unknowns is reduced by one, because the force in this fiber becomes known and equal to its limit value. The number of compatibility conditions is reduced by one too, because the yielded fiber displacement starts increasing and it remains unknown. Anyway, the problem can be solved using the $m - 1$ equations of system (1.46) to find the reactions and Eq. (1.47) to find the only unknown displacement.

1.3.7 Plastic moments

If all the fibers are still in the elastic field, the bending moment value, that makes only one fiber yield, can be calculated by imposing each reinforcement reaction equal to its ultimate force. The first fiber, that plasticizes, is the one corresponding to the minimum bending moment. In order to find this value, the ultimate forces $P_{P,i}$ are substituted in each equation of (1.43) and then the bending moments are computed. The first plastic moment is the minimum.

First of all, the reactions are calculated from Eq. (1.43).

$$\{P\} = [\lambda]^{-1}\{\lambda_M\}M \quad (1.48)$$

$$P_i = [\lambda]_i^{-1}\{\lambda_M\}M \quad (1.49)$$

Then the condition $P_i = P_{P,i}$ is considered and the correspondingly bending moment is evaluated.

$$P_{P,i} = [\lambda]_i^{-1}\{\lambda_M\}M_{P,i} \quad (1.50)$$

$$M_{P,i} = \frac{P_{P,i}}{[\lambda]_i^{-1}\{\lambda_M\}} \quad (1.51)$$

As previously remarked the first plastic moment is the minimum among these values.

$$M_{P,1} = \min_{i=1,m} \frac{P_{P,i}}{[\lambda]_i^{-1}\{\lambda_M\}} \quad (1.52)$$

In the previous equations the subscript i of the matrix $[\lambda]^{-1}$ indicates that only the i row is considered.

At a following stage, when at least one fiber is yielded, it is possible to do the same but considering Eq. (1.46) instead of Eq. (1.43).

$$\{P_c\} = [\lambda_{cc}]^{-1}[\{\lambda_{Mc}\}M - [\lambda_{cf}]\{P_{P,f}\}] \quad (1.53)$$

$$P_i = [\lambda_{cc}]_i^{-1}[\{\lambda_{Mc}\}M - [\lambda_{cf}]\{P_{P,f}\}] \quad (1.54)$$

Then the condition $P_i = P_{P,i}$ is considered and the correspondingly bending moment is evaluated.

$$P_{P,i} = [\lambda_{cc}]_i^{-1}[\{\lambda_{Mc}\}M_{P,i} - [\lambda_{cf}]\{P_{P,f}\}] \quad (1.55)$$

$$M_{P,i} = \frac{P_{P,i} + [\lambda_{cc}]_i^{-1}[\lambda_{cf}]\{P_{P,f}\}}{[\lambda_{cc}]_i^{-1}\{\lambda_{Mc}\}} \quad (1.56)$$

So, the j -th plastic moment is given by the equation:

$$M_{P,j} = \min_{i=1, n_c} \frac{P_{P,i} + [\lambda_{cc}]_i^{-1}[\lambda_{cf}]\{P_{P,f}\}}{[\lambda_{cc}]_i^{-1}\{\lambda_{Mc}\}} \quad j = 2, \dots, m \quad (1.57)$$

1.3.8 Crack propagation condition

The crack propagation condition is evaluated regarding linear elastic fracture mechanics. The crack propagates when the stress intensity factor K_I reaches its critical value, that is the fracture toughness of the material K_{IC} .

$$K_I = K_{IC} \quad (1.58)$$

The stress intensity factor is the sum of two contributions: one due to the applied bending moment and another due to the reactions of reinforcements.

$$K_I = K_{I,M} - \sum_{i=1}^m K_{I,i} \quad (1.59)$$

The minus sign is related to the fact that a positive bending moment acts opening the crack, while a positive force acts closing it. Eq. (1.59) can be rewritten taking into account the expressions of the stress intensity factors for the moment and the force given in [1.3.2] and by using the scalar product for the summation.

$$K_I = \frac{M}{h^{3/2}b} Y_M - \frac{\{Y_P\}^T \{P\}}{h^{1/2}b} = K_{IC} \quad (1.60)$$

where $\{Y_P\}$ is the vector of the shape functions related to the concentrated forces.

The stress intensity factor due to bending moment is only function of the normalized crack depth, while the one related to the forces is function of the normalized position of the fiber too.

$$Y_M = Y_M(\xi) \quad (1.61)$$

$$Y_{P,i} = Y_P(\xi, \zeta_i) \quad (1.62)$$

The value of the moment, that makes the crack propagate, is:

$$M_F = \frac{h^{3/2}b}{Y_M} \left(K_{IC} + \frac{\{Y_P\}^T \{P\}}{h^{1/2}b} \right) = \frac{h^{3/2}b}{Y_M} K_{IC} + \frac{h}{Y_M} \{Y_P\}^T \{P\} = R_1 + R_2 \{Y_P\}^T \{P\} \quad (1.63)$$

In the previous equation the parameters R_1 and R_2 are introduced in order to write the relation in a more compact way.

1.3.9 Forces and bending moment at crack propagation

The value of the moment M_F causing fracture propagation is function of the reinforcement reactions $\{P\}$, Eq. (1.60), but these forces are function of the applied bending moment because of the compatibility equation.

So, by imposing the condition $M = M_F$ it is possible to calculate the values of the fiber reactions at crack propagation.

If all the fibers are in the elastic field, this result can be attained substituting the value of the moment from Eq. (1.63) in Eq. (1.43).

$$[\lambda]\{P\} = \{\lambda_M\}(R_1 + R_2\{Y_P\}^T\{P\}) \quad (1.64)$$

Then the following linear system is obtained:

$$([\lambda] - R_2\{\lambda_M\}\{Y_P\}^T)\{P\} = R_1\{\lambda_M\} \quad (1.65)$$

If at least one fiber is plasticized, it is necessary to use Eq. (1.46) instead of Eq. (1.43).

$$[\lambda_{cc}]\{P_c\} = \{\lambda_{Mc}\}(R_1 + R_2\{Y_P\}^T\{P\}) - [\lambda_{cf}]\{P_{P,f}\} \quad (1.66)$$

In order to obtain a linear system, the vectors $\{Y_P\}$ and $\{P\}$ are split into two parts as done before in the case of Eq. (1.44).

$$[\lambda_{cc}]\{P_c\} = \{\lambda_{Mc}\} \left[R_1 + R_2 \left(\{Y_{P,f}\}^T \{P_{P,f}\} + \{Y_{P,c}\}^T \{P_c\} \right) \right] - [\lambda_{cf}]\{P_{P,f}\} \quad (1.67)$$

Eventually the following linear system is achieved:

$$\left([\lambda_{cc}] - R_2\{\lambda_{Mc}\}\{Y_{P,c}\}^T \right) \{P_c\} = \{\lambda_{Mc}\} \left(R_1 + R_2\{Y_{P,f}\}^T \{P_{P,f}\} \right) - [\lambda_{cf}]\{P_{P,f}\} \quad (1.68)$$

By solving system (1.65) or (1.68) the values of the forces at crack propagation are found. In the second case the condition $\{P_f\} = \{P_{P,f}\}$ is still valid and it lets calculate all the reactions and not only the ones of the elastic fibers $\{P_c\}$. Then, by substituting back the values of the forces $\{P\}$ in Eq. (1.63), it is possible to attain the value of the applied bending moment, that makes the crack advance.

1.3.10 Brittleness number and dimensionless analysis

If all the reinforcements are equal, Eq. (1.60) can be rewritten in the following form:

$$\frac{M_F}{K_{IC}h^{3/2}b} = \frac{1}{Y_M(\xi)} \left(1 + \frac{N_P}{\rho} \sum_{i=1}^m \rho_i \alpha_i(\xi, \zeta_i) Y_P(\xi, \zeta_i) \right) \quad (1.69)$$

where

$$N_P = \frac{\rho \sigma_y h^{1/2}}{K_{IC}} = \frac{m P_{P,i}}{K_{IC} h^{1/2} b} \quad (1.70)$$

$$\rho_i = \frac{A_i}{bh} \quad (1.71)$$

$$\rho = \frac{mA_i}{bh} \quad (1.72)$$

$$\alpha_i(\xi, \zeta_i) = \frac{P_i}{P_{P,i}} \quad (1.73)$$

The non-dimensional parameter N_P is named brittleness number (Carpinteri 1981, 1984) and its value is responsible for the behaviour of the system. The higher N_P is, the more ductile the behaviour of the structure will be and vice versa.

In the results of the present work also the following quantities will be sometimes normalized.

$$\tilde{M} = \frac{M}{K_{IC}h^{3/2}b} \quad (1.74)$$

$$\tilde{P} = \frac{P}{K_{IC}h^{1/2}b} \quad (1.75)$$

$$\tilde{\phi} = \frac{\phi E h^{1/2}}{K_{IC}} \quad (1.76)$$

$$\tilde{w} = \frac{wE}{K_{IC}h^{1/2}} \quad (1.77)$$

If the properties are different from one reinforcement to another, Eq. (1.70) can be generalized in the following way:

$$N_P = \frac{\sum_{i=1}^m P_{P,i}}{K_{IC}h^{1/2}b} \quad (1.78)$$

1.3.11 Ultimate bending moment

When the section is completely cracked and the depth of the fracture is equal to the beam height, it is possible to compute the ultimate bending moment the structure is able to bear.

At this final stage characterized by large displacements all the fibers are plasticized in tension, while the resultant of compressions is applied in a single point as shown in Fig. (1.4).

If all the fibers are equal and ζ_G is the normalized depth of their barycentre, the ultimate bending moment is given by:

$$M_u = mP_p b_U = mP_p h(1 - \zeta_G) = N_p K_{IC} h^{3/2} b(1 - \zeta_G) \quad (1.79)$$

This value is slightly overestimate because the arm reduction due to the rotation ϕ is disregarded. In any case this situation is only hypothetical because the point of the matrix, where the reaction is applied, should bear an infinite stress.

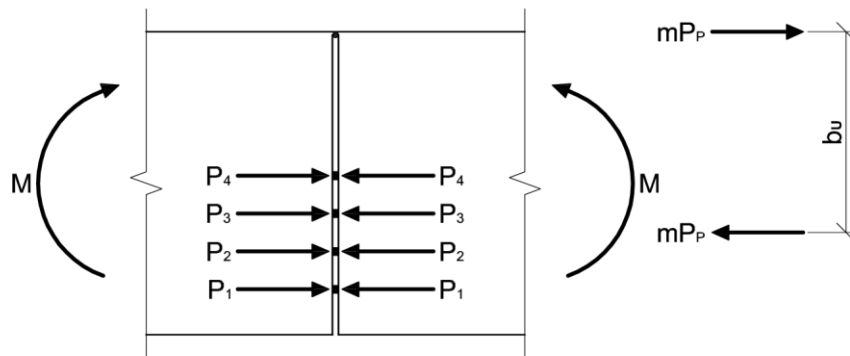


Figure 1.4: Geometry corresponding to the ultimate bending moment

M_u can be computed also with different types of fibers, considering the equilibrium around the point of the matrix where the compression reaction is applied.

1.4 Monotonic loading

In this section the numerical algorithm is described in detail for the case of a monotonic loading applied controlling the crack length is analysed. Using this technique, it is possible to describe completely the softening branches even with a positive slope of the moment-rotation response of the system.

1.4.1 Crack Length Control Scheme (CLCS)

The presented procedure is based on the fact that the value of the applied bending moment should be equal to the cracking moment in order to make fracture advance. So, for each value of the crack depth, starting from an initial value and up to a stopping value fixed in advance, the cracking moment is computed using the expressions shown in [1.3.9]. The relation between the bending moment and the crack depth is obtained. Then, to describe the moment-rotation response it is necessary to notice that a fiber can attain its ultimate force even if the crack is not advancing and this changes the stiffness of the system and the slope of the graph. So, the plastic moments of all the reinforcements should be computed for a given depth of the crack, but only the ones lower than the cracking moment and higher than one computed for the previous depth should be taken

into account. These values of moments and their respective rotations are added to the graph. The plastic moments are evaluated regarding [1.3.7].

Now the numerical algorithm is described in detail. The following input parameters have to be considered:

- Beam geometry
 - b – section thickness
 - h – section depth
 - a_{start} – crack initial depth (or ξ_{start} - normalized initial crack depth)
- Reinforcements geometry
 - m – number of fibers
 - c_{min} – position of first fiber (or ζ_{min} – normalized position of first fiber)
 - c_{max} – position of last fiber (or ζ_{max} – normalized position of last fiber)
- Matrix material
 - E – Young Modulus
 - K_{IC} – matrix fracture toughness
- Reinforcement material
 - $P_{P,i}$ – fiber ultimate force

The value of the ultimate force of the fiber can be given directly or it can be computed starting from these additional parameters (round fiber):

- r_i – fiber radius
- $\sigma_{y,i}$ – fiber yielding tension

$$P_{P,i} = (\pi r_i^2) \sigma_{y,i} \quad \text{or} \quad P_{P,i} = d_f l_f \tau_{max,i} \quad (1.80)$$

The fibers are considered equally spaced between c_{min} and c_{max} , but it is possible to define the position of each reinforcement too.

Further parameters are necessary to define the crack depths for which the cracking moment will be computed:

- a_{stop} – stopping crack depth (or ξ_{stop} - normalized stopping crack depth)
- $\Delta\xi$ – normalized crack depth increment at each calculation step

For each value of the crack depth it is necessary to find the active fibers crossing the crack. If the crack tip is too close to a fiber, the crack length should be increased of a fraction of $\Delta\xi$ in order to avoid numerical issues because of the shape function $Y_P(\xi, \zeta_i)$ singularity in correspondence of a fiber. The active fibers are identified by the following relation:

$$\zeta_i < \xi^{(k)} \quad (1.81)$$

Where the apex k indicates the generic calculation step.

Then, using Eq. (1.15) and (1.17) the shape functions for the bending moment $Y_M(\xi^{(k)})$ and for the reactions $Y_P(\xi^{(k)}, \zeta_i)$ are attained.

The compliances are evaluated with Eq. (1.33), (1.34), (1.35) and (1.36) considering only the active fibers and if necessary they are arranged in a matrix or in a vector.

$$\lambda_{MM}^{(k)} = \lambda_{MM}(E, b, h, \xi^{(k)}) \quad (1.82)$$

$$\{\lambda_M^{(k)}\} = \{\lambda_M(E, b, h, \xi^{(k)}, \zeta_i)\} \quad (1.83)$$

$$[\lambda^{(k)}] = [\lambda(E, b, \xi^{(k)}, \zeta_i, \zeta_j)] \quad (1.84)$$

The problem partition described in [1.3.6] is introduced using two vectors $\{c\}$ and $\{f\}$ containing respectively the indexes of the elastic and plasticized fibers. At the beginning of each step k all the reinforcements are in the elastic field. So $\{c\}$ is the vector of the active fibers, while $\{f\}$ is empty. Hence it is possible to obtain $\{\lambda_{M,c}\}$, $\{\lambda_{M,f}\}$, $[\lambda_{cc}]$, $[\lambda_{cf}] = [\lambda_{fc}]$ and $[\lambda_{ff}]$.

The values of the reactions at crack propagation are attained solving linear system (1.65). If at least a force in one fiber is higher than its ultimate value, the most loaded fiber is considered yielded, its force is set equal to $P_{P,i}$, $\{c\}$ and $\{f\}$ are update and consequently the partitioned matrix or vector of compliances are updated too. The reactions at crack propagation are calculated again, but now using Eq. (1.68). Until all the forces are lower or equal to their ultimate value, it is necessary to repeat the calculation, updating the yielded fibers. At the end the bending moment $M_F^{(k)}$ and the rotation $\phi_F^{(k)}$ are achieved with Eq. (1.63) and (1.41).

Now using a similar iterative procedure, the plastic moments and the respective rotations are evaluated by using Eq. (1.52), Eq. (1.57) and Eq. (1.41). Only the moments, that respect the following condition, are taken into account:

$$M_F^{(k-1)} < M_{P,i}^{(k)} < M_F^{(k)} \quad (1.85)$$

Then the crack length can be updated and the procedure can be repeated with the new value.

$$\xi^{(k+1)} = \xi^{(k)} + \Delta\xi \quad (1.86)$$

At each step the crack openings could be computed too. This can be done with Eq. (1.39).

It is possible to summarize the algorithm in the following way:

1. Initialization
2. For each value of crack depth $\xi^{(k)}$
 - a. Calculation of shape functions and compliances
 - b. Initialization of $\{c\}$ and $\{f\}$
 - c. Iterative procedure to find the cracking moment $M_F^{(k)}$
 - i. Computation of cracking forces with Eq. (1.65) or (1.68)
 - ii. Update $\{c\}$ and $\{f\}$, partitioned matrix and vector and reactions of yielded fibers
 - iii. Stop if all the reactions are lower or equal to their ultimate value
 - d. Computation of $M_F^{(k)}$ and $\phi_F^{(k)}$ with Eq. (1.63) and (1.68)
 - e. Computation of plastic moments with Eq. (1.52) and (1.57) and rotations with Eq. (1.41)
 - f. Add plastic moments that satisfy Eq. (1.85)
3. Update crack depth according to Eq. (1.86) and return to 2 if $\xi^{(k+1)} < \xi_{stop}$
4. Plot $M - \phi$ values

1.4.2 Parametric study

In this paragraph, the results of several parametric studies that have been made by means of the algorithm will be commented.

First, there is a clear transition in the failure phenomena from brittle to ductile as the fiber content increases, whatever the constitutive law adopted. It can be clearly seen in Fig. (1.5 and 1.6), where the curves have been obtained by varying the fiber content, V_f , and all other parameters stay the same.

Moreover, particular importance has been given to the minimum reinforcement purpose, marked in red in Figs. (1.5 and 1.6), The parametric studies reveals that using a yielding constitutive law for the fiber, when the structural size decreases the percentage of fibers, ρ , to get the minimum reinforcement increases, Fig. (1.5). This can be explained by the Brittleness Number (Eq. 1.71). On the other hand, it has be noted that using a slippage constitutive law for the fiber, when the structural size (h) decreases the fiber percentage, ρ , to get minimum reinforcement remains almost constant Fig. (1.6). This can be explained by substituting the Eq. (1.3) in the Eq. (1.70), in order to show that the Brittleness Number is not related to h , Eq. (1.87).

$$\begin{aligned}
 N_P &= \frac{\sum_{i=1}^m P_{P,i}}{K_{IC}\sqrt{h} b} = \frac{mP_{P,i}}{K_{IC}\sqrt{h} b} = \frac{md_f l_f \tau_{max}}{K_{IC}\sqrt{h} b} = \frac{m \left(2\pi \sqrt{\frac{A}{\pi}} \right)_i l_f \tau_{max}}{K_{IC}\sqrt{h} b} = \frac{2\sqrt{\pi} m \tau_{max} l_f \sqrt{A}_i}{K_{IC}\sqrt{h} b} \\
 &= \frac{2\sqrt{\pi} m \tau_{max} l_f \sqrt{\frac{bh\rho}{m}}}{K_{IC}\sqrt{h} b} = 2 \sqrt{\frac{\pi m \rho}{b}} \frac{\tau_{max}}{K_{IC}} l_f
 \end{aligned} \tag{1.87}$$

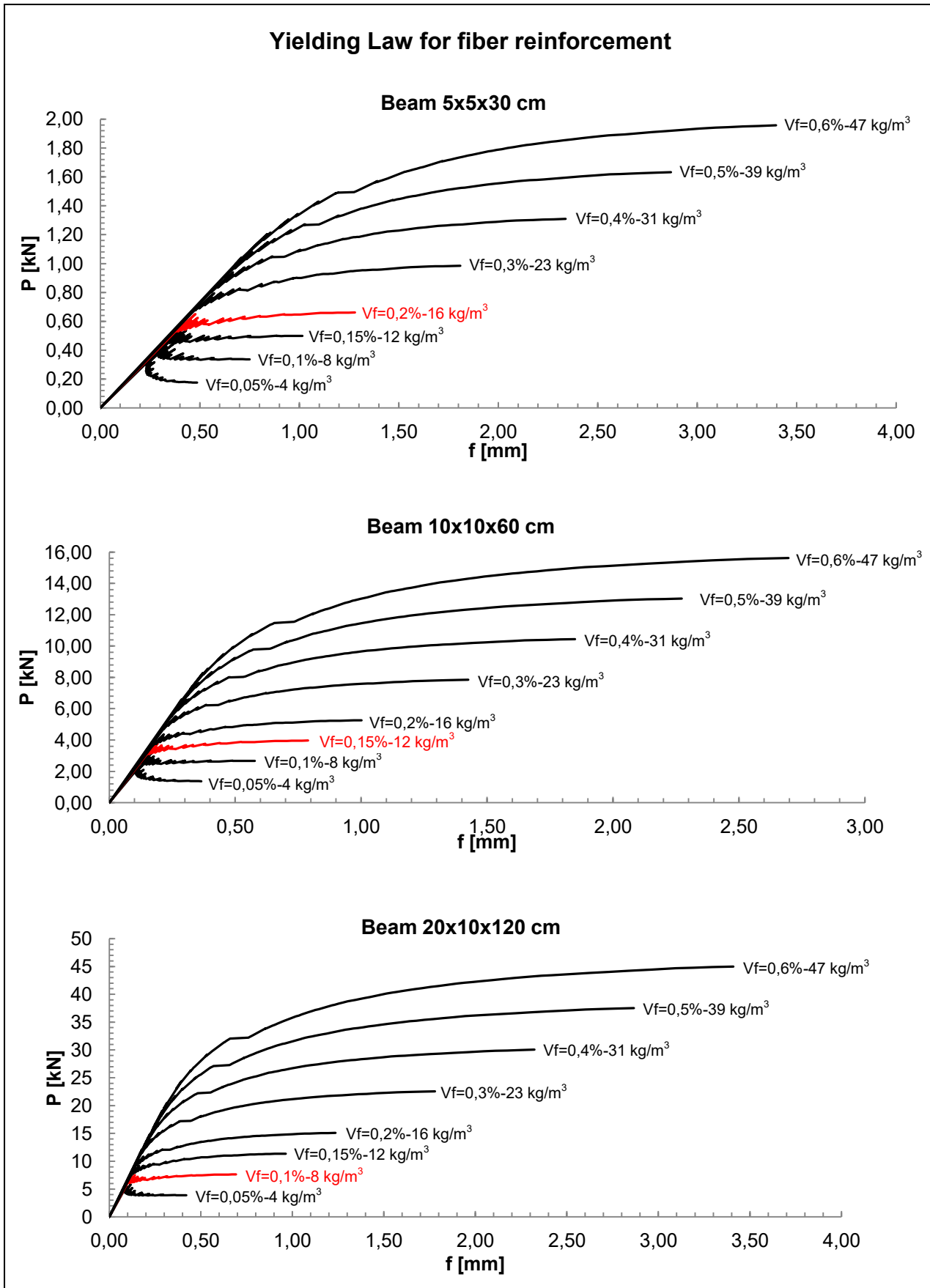


Figure 1.5: Fiber content influence in the failure phenomena. Figures have been obtained by implementing a Slippage constitutive law for the fiber reinforcement and by setting: $K_{IC}=60 \text{ daNcm}^{-1.5}$, $a_o=5 \text{ cm}$, $E=31500 \text{ MPa}$, $f_{cm}=33 \text{ MPa}$, $f_y=1100 \text{ MPa}$, $m=20$

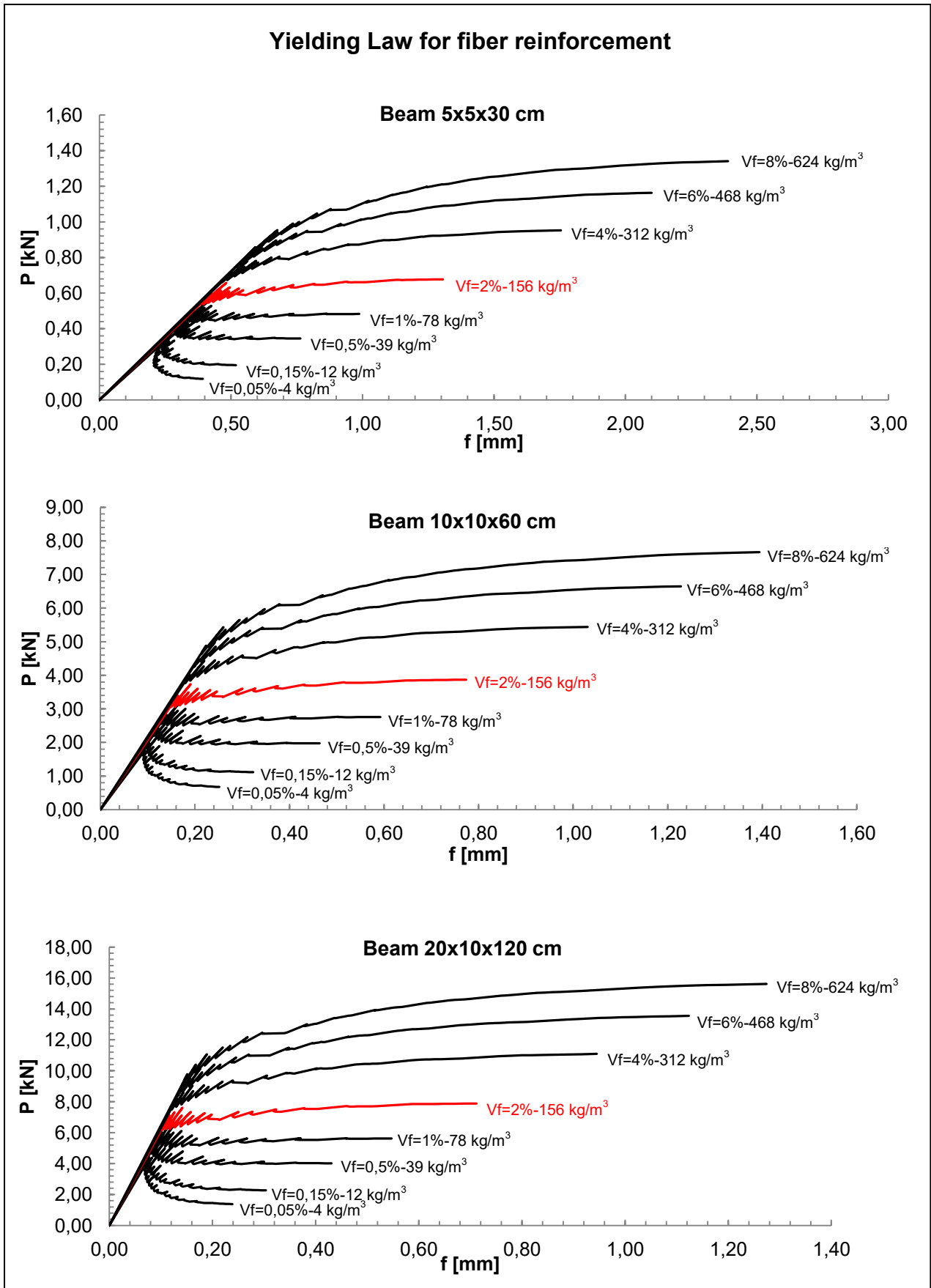


Figure 1.6: Fiber content influence in the failure phenomena. Figures have been obtained by implementing a yielding constitutive law for the fiber reinforcement and by setting: $K_{IC}=60 \text{ daNcm}^{-1.5}$, $a_0=5 \text{ cm}$, $E=31500 \text{ MPa}$, $f_{cm}=33 \text{ MPa}$, $f_y=1100 \text{ MPa}$, $m=20$

As regards the critic value of the Stress Intensity Factor, the load peak moves up and to the right when K_{IC} increases in the load versus deflection diagram, Fig. (1.7). At the same time, the asymptotic behavior doesn't change. In the case of strong hardening behavior, the role played by K_{IC} is negligible. Fig. (1.7) has been evaluated by setting : $b=10$ cm; $h=20$ cm; $L=120$ cm; $a_o=5$ cm; $E=31500$ MPa; $f_{cm}=33$ MPa; $f_y=1100$ MPa; $m=20$ and by assigning a constitutive yielding law to the fiber content. However, this claim is still valid with the variations in dimension scale and in the constitutive law adopted.

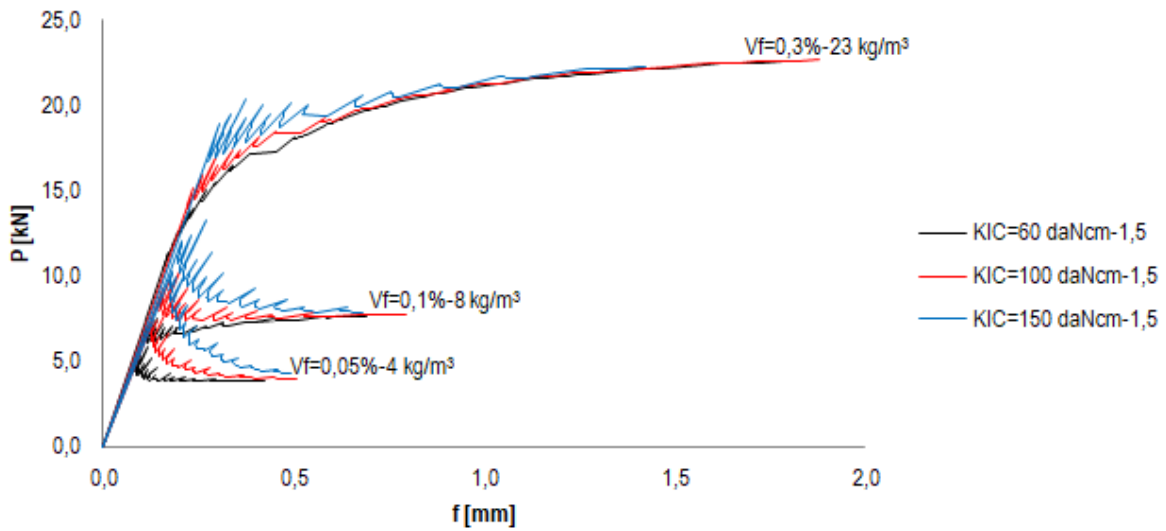


Figure 1.7: Results of the parametric study related to K_{IC}

The yielding stress, f_y , or the frictional bonding force between the matrix and the reinforcement, τ_{max} , also affect the shape of the curves. In particular, the load peak and asymptote move up when f_y or τ_{max} increases, as shown in Fig (1.8). As in the case of K_{IC} , this assertion is true whatever the dimensional scale.

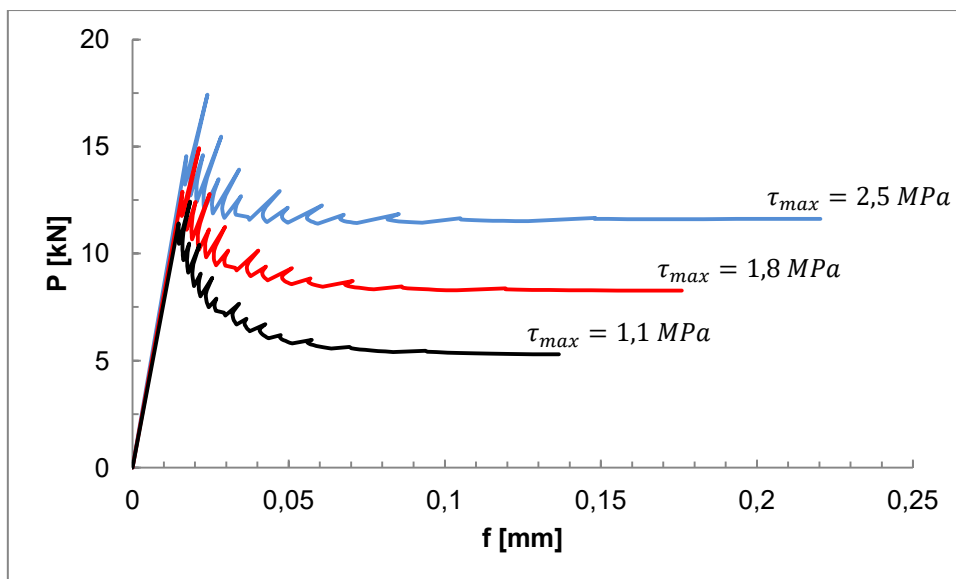


Figure 1.8: Results of the parametric study related to τ_{max}

The last two remarks are related to the initial crack length. First, for $m > 20$, the condition of complete diffusion of the fibers is represented ($m = \infty$). N_p value involving a ductile-to-brittle transition depends on the initial crack length a (concrete cover). i.e. for $m > 20$: when $a/h \cong 0.1$, we get $N_p = 1.3$; when $a/h \cong 0.3$, we get $N_p = 0.8$.

Second, when the initial crack length, a , is small compared to the beam height, h , the global structural behavior is brittle. Consequently, the ductile-to-brittle transition arises for high values of N_p , and hence also of ρ . On the other hand, when a is large, the structural behavior appears to be ductile. Consequently, the ductile-to-brittle transition arises for low values of N_p . In conclusion, we need to set an initial crack length larger than $\frac{1}{4} \div \frac{1}{3} h$ in order to have a ductile behavior.

1.4.3 Numerical errors

The value of the increment $\Delta\xi$ and the distance between the crack tip and the closest active fiber have a strong influence on the numerical results.

In particular if $\Delta\xi$ is too high, the graph $M - \phi$ loses its meaning and it is not possible any more to identify the peaks due to the bridging action of the fibers. On the contrary, if its value is too small, the graph is described accurately, but computational time increases.

As seen in section [1.3.2], the shape function $Y_p(\xi, \zeta_i)$ has a singularity for $\xi = \zeta_i$, in correspondence of the position of the fiber. Fig (1.3) shows that the function tends to infinity very quickly and this causes the numerical issues. It is sufficient that $\xi - \zeta_i < 1 \cdot 10^{-4}$ to observe the peaks of the curve rising very much losing their meaning.

In the present analysis the following values are normally used:

$$\Delta\xi = 0,005 \quad (1.88)$$

$$\xi - \zeta_i > 0,05 \Delta\xi \quad (1.89)$$

These issues are showed in Fig. (1.9) and Fig. (1.10) using a beam with the following characteristics:

$$b = 25 \text{ cm}$$

$$h = 40 \text{ cm}$$

$$a/h = 0,1$$

$$E = 30 \text{ GPa}$$

$$K_{IC} = 100 \text{ daNcm}^{-3/2}$$

$$\sigma_y = 450 \text{ MPa}$$

$$m = 3$$

$$\zeta_{min} = 0,1$$

$$\zeta_{max} = 0,3$$

$$r_i = 3,86 \text{ mm}$$

$$N_p = 0,40$$

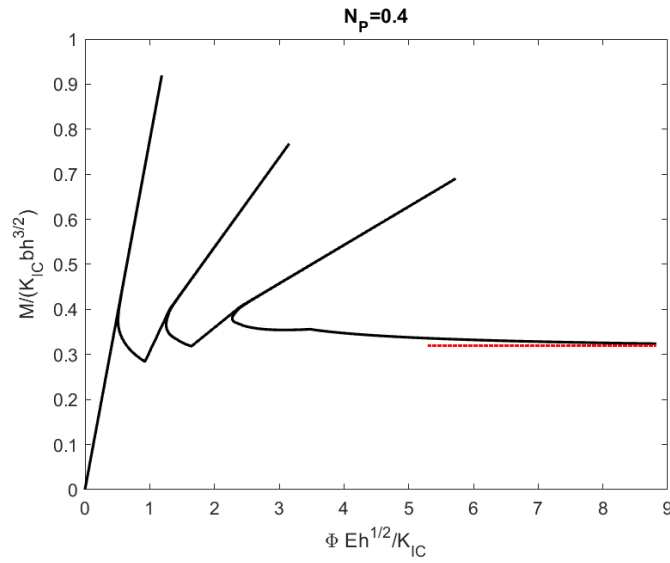


Figure 1.9: Moment-rotation diagram affected by the numerical singularity

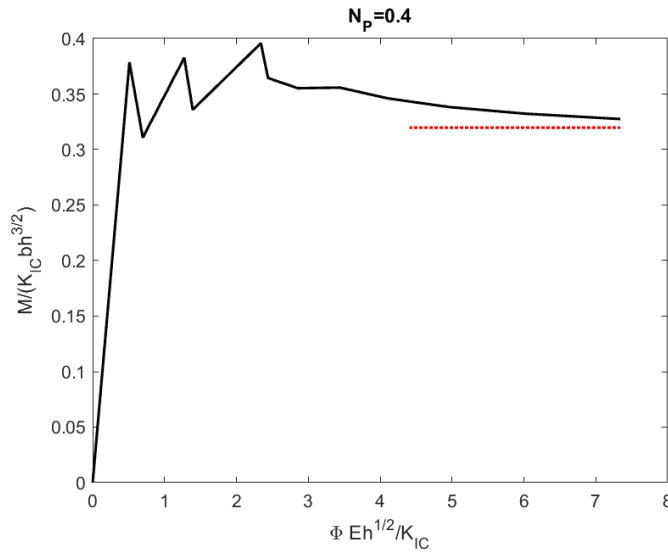


Figure 1.10: Moment-rotation diagram affected by an insufficient number of points

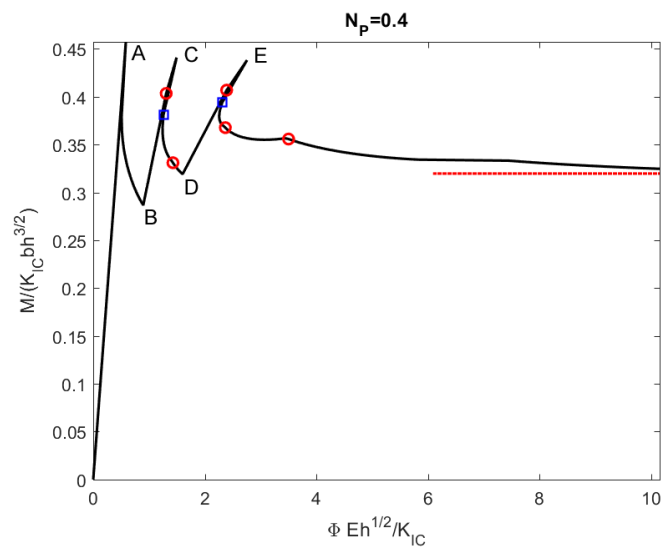


Figure 1.11: The correct moment-rotation diagram

The first picture is obtained with a value of $\Delta\xi$ lower than usual and equal to 0,0005. In this case it is possible to notice the peaks becoming too high because of the shape function $Y_p(\xi, \zeta_i)$ singularity when the crack tip is too close to a fiber. On the contrary in the second picture the interval $\Delta\xi$ is too high (0,05) and the peaks are not any more recognizable. The right $M - \phi$ response is the one showed in Fig. (1.11) achieved with a $\Delta\xi$ equal to 0,005.

2. Experimental campaigns critical review

A lot of effort, during this work, has been put to make a bibliographic research for the purpose of collecting data to check and validate the Bridged Crack Model. In this chapter search results are reviewed. In particular, the following experimental campaigns aimed at studying the effects of fibre reinforcements on the flexural behaviour of full scale concrete beams are presented: Plizzari et al. [2.1]; Carpinteri et al. [2.2]; Swamy et al. [2.3]; Olivito et al. [2.4]; Kang et al. [2.5].

2.1 Plizzari experimental work

Based on the idea of taking simultaneous advantage of the effects of different types of fibers, new materials called hybrid fiber reinforced concretes have been developed by combining fibers of different geometry and material. In the paper, authors evaluate the benefits in terms of concrete toughness from a combination of micro- and macro-steel fibers, under both bending and uniaxial tensile tests on specimens of different sizes. Concrete toughness is better determined by performing uniaxial tensile tests but the experimental difficulties related to these tests suggested several code makers to propose bending tests instead (either with three or four point loading).

The aim of the present work is to investigate the possibility of optimizing concrete toughness by combining steel fibers of two different sizes. Concrete toughness was determined by means of both uniaxial and bending tests on notched specimens. Freely rotating platens with spherical hinges were adopted as boundary conditions in the uniaxial tests to better control the crack development. Bending tests were carried out on beam specimens having two different geometries and different notch length/beam depth ratios. Moreover, authors worked on the determination of a good approximation of the post-cracking behavior based on a polylinear law and the suitability of adopting a bilinear law (for concrete with a single type of fiber) and a trilinear law (for concrete with two types of fiber) has been studied. In fact, since fibers of different lengths become efficient at different stages of the cracking process, the smaller fibers control the microcrack growth whereas the longer fibers become active for larger crack openings.

Below, a synthetic description of the authors experimental tests is followed by the comparison of experimental figures and numerical analysis carried out by the Bridged Crack Model.

2.2.1 Material and experimental setup

Experiments were carried out on specimens made of a normal strength concrete with 355 kg/m³ of cement [CEM II/A-LL 32.5R according to UNI-EN 197 (CEN 2000)], 180 kg/m³ of water (water-cement ratio of 0.55), 3.9 L/m³ of superplasticiser, and 1,900 kg/m³ of aggregates with a maximum size of 15 mm. A grain size distribution close to the Bolomey curve was used. Two different types of steel fibers were adopted: the first one had a length (L_f) of 30 mm and a diameter (ϕ) of 0.6 mm whereas the second one was a shorter fiber having a length of 12 mm and a diameter of 0.18 mm; these fibers will be named as

“macrofiber” and “microfiber,” respectively. The geometrical and mechanical characteristics of the fibers used in the present work are reported in Table 2.1. Fibers were added to the concrete matrix in four different combinations as shown in Table 2.2: one plain concrete and three concretes having a volume fraction of fibers often used in practice, equal to 0.38% (30 kg/m³), in all cases. Table 2.2 also shows concrete compressive strength measured after 28 days of curing on cube specimens (150 x 150 x 150 mm) and the slump of the fresh concrete; the slight decrease of workability of FRC can be observed. The specimens were cured in a fog room until the time of the test and a vaseline layer was applied on the crack section in order to limit shrinkage cracking.

Properties	Macrofiber	Microfiber
Length (L_f) (mm)	30	12
Diameter (ϕ_f) (mm)	0.60	0.18
Aspect ratio (L_f/ϕ_f)	50	67
Tensile strength (MPa)	1,100	1,800
Young's modulus (GPa)	210	210

Table 2.1: Proprieties of Steel Fibers

Material	Steel fiber		Total volume fraction $V_{f,tot}$ (%) _{vol.}	Compressive strength $f_{c,cube}$ (MPa)	Slump s (mm)
	30/0.6 (%) _{vol.}	12/0.18 (%) _{vol.}			
Plain	—	—	—	28.3	150
Macrofiber	0.38	—	0.38	29.3	110
Microfiber	—	0.38	0.38	31.9	130
Hybrid	0.19	0.19	0.38	33.0	130

Table 2.2: Fiber Combinations, Compressive Strength, and Workability (Slump) for the Concrete

In order to investigate the fiber effects on concrete behavior, fracture tests should be performed and a stable control of the test is necessary. For this reason, a 500 kN hydraulic testing machine (Instron 8500+) with a proportional integrative derivative (PID) closed loop control that permits to compensate the finite stiffness of the load system was adopted. The crack mouth opening displacement (CMOD), measured by a clip gauge, was adopted as feedback signal in both the uniaxial and the bending tests. Uniaxial tests with freely rotating platens were performed on specimens having a size of 100 x 200 x 40 mm [Fig. 2.1(a)] that were sawn from concrete prisms having a size of 100 x 200 x 400 mm to favor a three-dimensional distribution of the fibers. A single notch with a depth of 15 mm, a width of 4 mm and a tip with a triangular shape was sawn with a diamond blade. Four linear variable differential transducers (LVDTs) with a base length of 45 mm were located across the notched section to evaluate the relative displacement and rotation of the sections at each side of the crack surface [Fig. 2.1(a)]. In order to reduce undesired eccentricities, the specimens were carefully positioned (and then glued) on steel platens by adopting 4 instruments with a precision of 0.01 mm; this gave good alignment of the specimen along the loading axis [Fig. 2.1(b)]. The free rotation of the platens was obtained by means of two spherical hinges placed at 150 mm from the glued surface: in this way it was possible to localize the center of rotation at the specimen ends.

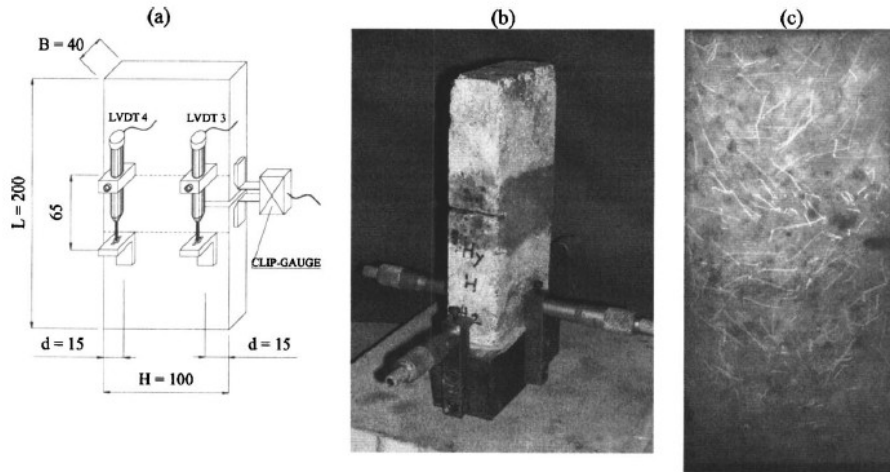


Figure 2.1: (a) Tensile test specimen instrumented with four linear variable differential transducers and one clip gauge; (b) setup for positioning the steel platens; and (c) fiber distribution from a x-ray picture

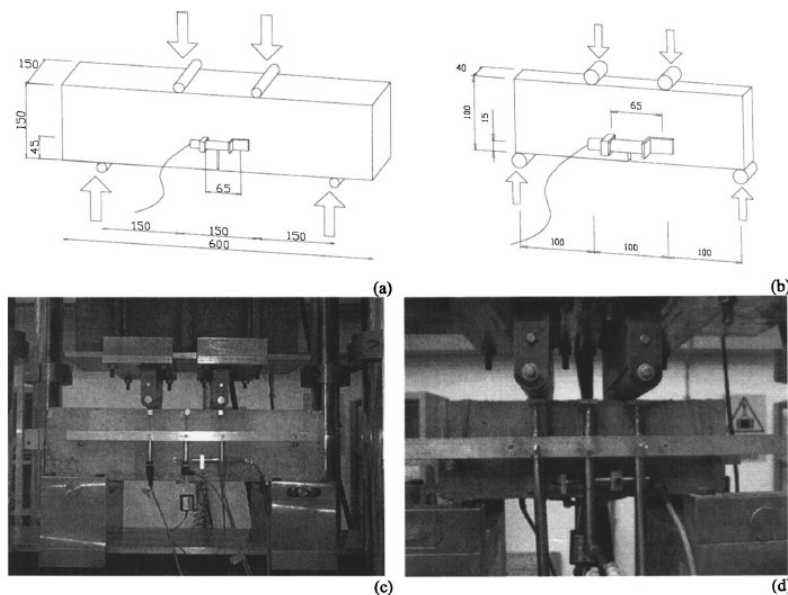


Figure 2. 2: (a, b) Specimen geometry and (c, d) testing setup for the larger and smaller beams, respectively

The tests were carried out by imposing a CMOD rate of $1 \mu\text{m}/\text{min}$ until the load–displacement curve had passed the peak and the fiber started activating. Afterwards, the CMOD rate was set to $2 \mu\text{m}/\text{min}$. Although it includes the elastic deformations of concrete, the average value of the displacement measured by the two LVDTs astride the notch was conventionally assumed as the crack tip opening displacement (CTOD) [Figure 2.1(a)]. The fiber distribution in a few specimens were checked before testing by means of x ray. From the x-ray image [Figure 2.1(c)] it is possible to observe the random distribution of fibers with the shadows of the macrofibers and the faint traces of the microfibers. Four point bending tests were performed on two different specimen sizes. The first one had a size of $150 \times 150 \times 600 \text{ mm}$ with a notch depth of 45 mm and was tested according to the Italian Standard [Figure 2. 2(a)] (UNI 2003). The second one had the same crack surface as the uniaxial tensile test specimen to study the strain gradient effects: these beams had a size of $100 \times 320 \times 40 \text{ mm}$ and were tested with a span length of 300 mm and a distance

between the load points of 100 mm [Figure 2. 2(b)]. Three LVDTs were used to measure the vertical displacement at mid-span and under the load points whereas two LVDTs were placed at the notch tip to measure the CTOD [Figure 2. 2(c and d)]. Further, a clip gauge was placed across the notch to measure the CMOD [Figure 2. 2(c)]. The CMOD rate was 50 $\mu\text{m}/\text{min}$ for the larger beams (UNI 2003) and 2.5 $\mu\text{m}/\text{min}$ for the smaller beams.

2.1.2 Results and discussion

Now we show the experimental test results and then apply the Bridged Crack Model to the study of these concrete beams. In order to obtain a clearer comparison between the different specimen geometries, experimental results from the bending tests are reported in terms of nominal stress (σ_N) given by:

$$\sigma_N = \frac{FL_{SP}}{B_b(H_b - a_0)^2} \quad (2.1)$$

where F = force; B_b and H_b = beam thickness and depth, respectively; L_{SP} = span length; and a_0 = notch depth [Figs. 2.2(a and b)]. At least four specimens for each material and each specimen geometry were tested.

Figs. 2.3 and 2.4 compares analytical (thicker curves) versus experimental results, showing the nominal stress versus the CTOD. The average values of $E_c=25127 \text{ N/mm}^2$ and $f_{cm}=38 \text{ N/mm}^2$ were utilized in all cases for the Bridged Crack simulations. Meanwhile the value of the critical stress intensity factor varies from 45 to 70 $\text{daN/cm}^{3/2}$, as shown in Table 2.3. The fibres length was assumed to be 3, 1.2 and 2.8 for macrofibres, microfibers and hybrid fibres respectively. One should remember that all the fiber reinforced specimens were characterized by the same volume fraction of fibers (0.38%).

	b	h	L	a ₀	l _f	V _f	E	f _{cm}	K _{IC}
	cm	cm	cm	cm	cm	%	daN/cm ²	daN/cm ²	daN/cm ^{3/2}
large specimen	15	15	60	4,5	3	0,38	251270	36	45
					1,2				70
					2,8				60
small specimen	4	10	32	1,5	3	0,38	251270	36	45
					1,2				55
					2,8				50

Table 2. 3: Fiber Combinations, Compressive Strength, and Workability (Slump) for the Concrete

The experimental versus numerical comparisons demonstrate that the proposed model can be successfully applied to the study of fibre-reinforced concrete, showing the key aspects. Indeed, it can be clearly seen that the fiber geometry has a marked influence on concrete toughness. Peak stress ($\sigma_{N,max}$) is only moderately influenced by the presence of macrofibers. Microfibers increase the peak and the post-peak strength for small crack openings but this residual strength rapidly decreases since fibers are pulled out from the matrix. On the other hand, macrofibers become efficient for larger crack openings. In the hybrid FRC, however the residual strength is enhanced for both smaller and larger crack openings. The same behavior can be observed in small beams tested under four point

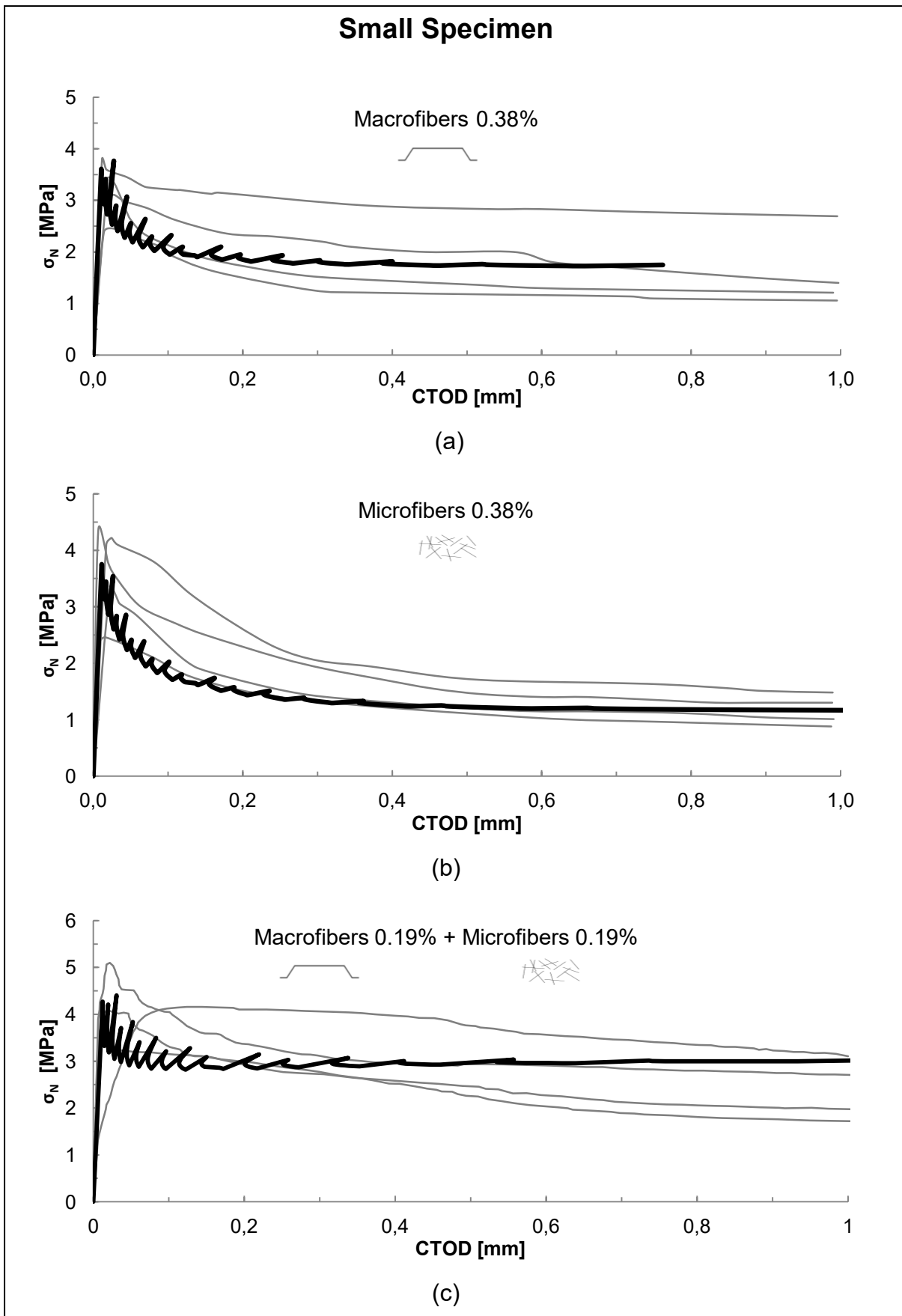


Figure 2.3: Experimental (grey) and Numerical (black) nominal stress versus crack tip opening displacement (CTOD) for (a) macro-FRC; (b) micro-FRC; (c) hybrid FRC from bending tests on small specimens

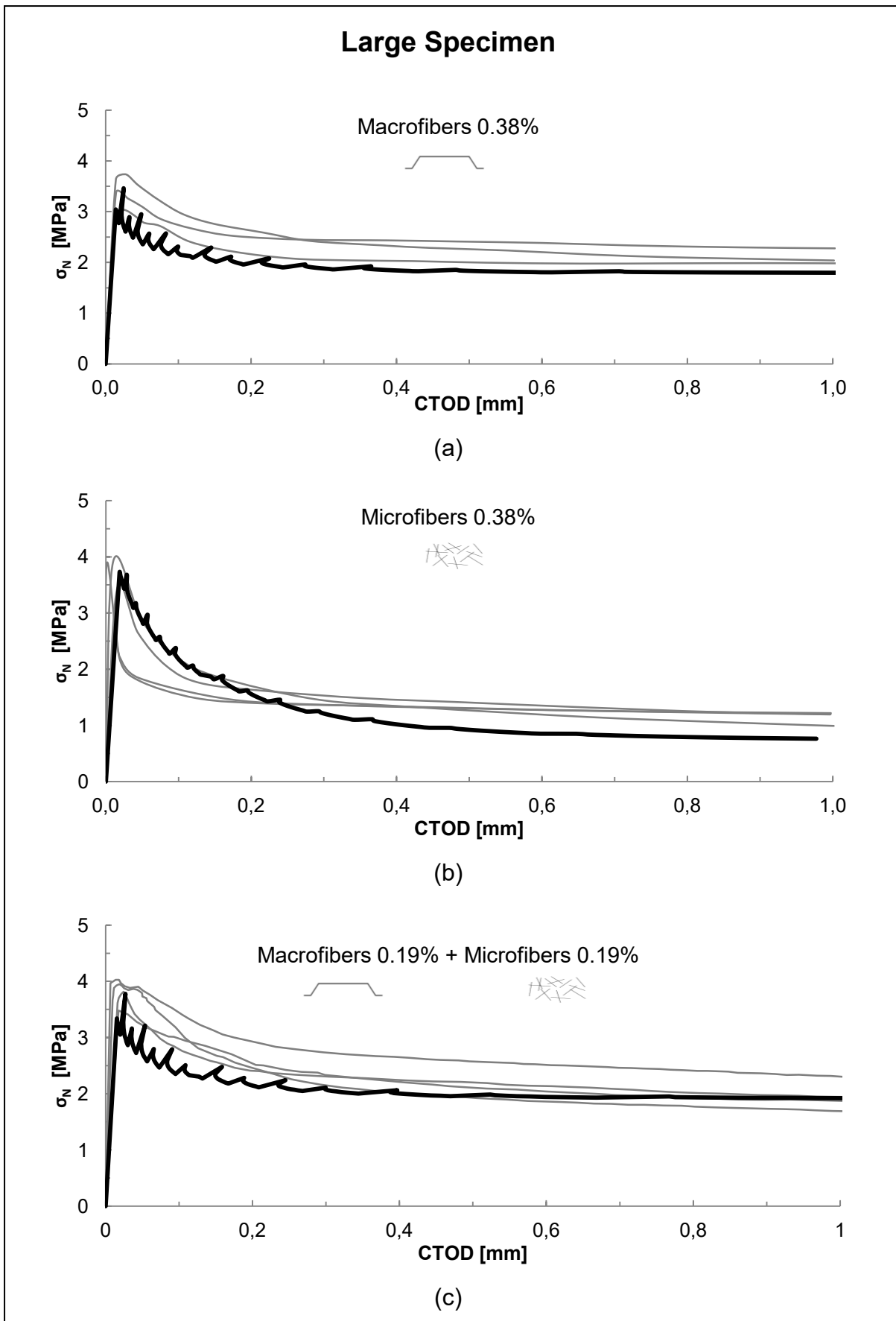


Figure 2.4: Experimental (grey) and Numerical (black) nominal stress versus crack tip opening displacement (CTOD) for (a) macro-FRC; (b) micro-FRC; (c) hybrid FRC from bending tests on large specimens

bending [Figs. 2.3(a and b)]. Also in this case, a small increase in the peak stress of concrete specimens with microfibers can be observed. Figs. 2.4(a and b) show curves from the larger beam specimens. An increase of about 15% in average peak strength will be noted in the hybrid specimens [Figs. 2.3(c) and 2.4(c)] compared to specimens with only macrofibers.

2.2 Carpinteri experimental work

This paper present a study where the analysis of fibre-reinforced concrete taking into account the nonlinear behavior of the material in tension and compression was addressed by a numerical approach based on the Cohesive–Overlapping Crack Model, in order to reveal the influence of fibre content in the flexural behavior of beams. Then the results of a numerical analysis and of an experimental campaign were compared in order to validate the proposed model.

Even then, the following is a description of the authors experimental tests. Last, results of this experimental campaign are compared to the numerical curves obtained through the Bridged Crack Model.

2.2.1 Material and experimental setup

The experimental investigation herein considered was carried out by Ventura and colleagues in 2003 at the Department of Structural Engineering and Geotechnics of the Politecnico di Torino. Four contents of steel fibres (from 0 kg/m³ (no fibres) to 40 kg/m³) and five contents of traditional steel bar reinforcement (from zero to 2Ø20) have been considered. For each case, four specimens have been tested for a total of 80 tests.

Specimens	P_u (kN)	M_u (kN mm)	f_t (MPa)	Mean f_t (MPa)
TC89-CC00-1	5.16	774.45	5.27	5.20
TC89-CC00-2	4.28	642.45	5.45	
TC89-CC00-3	4.20	629.85	5.13	
TC89-CC00-4	4.41	661.65	4.97	
TC89-CC10-1	5.14	770.55	5.67	5.52
TC89-CC10-2	5.14	770.70	5.54	
TC89-CC10-3	4.92	738.30	5.34	
TC89-CC20-1	6.56	984.00	7.38	6.96
TC89-CC20-2	4.98	747.30	5.60	
TC89-CC20-3	6.37	955.65	7.17	
TC89-CC20-4	6.84	1,026.45	7.70	
TC89-CC40-1	7.02	1,053.60	7.90	8.06
TC89-CC40-2	6.95	1,041.75	7.81	
TC89-CC40-3	8.38	1,257.60	9.43	
TC89-CC40-4	6.29	943.20	7.07	

Table 2. 4: Material tensile strengths, f_t , by varying the fibres content (see text)

The beams, characterized by a depth $h = 200 \text{ mm}$, a thickness $b = 100 \text{ mm}$, and a length $l = 1400 \text{ mm}$, have been subjected to a three-point bending test. The concrete cover was $c = 12 \text{ mm}$. A high performance concrete C60/75 with a maximum aggregate diameter $D_{max} = 20 \text{ mm}$ and steel fibers Bekaert Dramix RC-80/50-BN was utilized. Further tests were carried out in order to characterize the cementitious material: four concrete beams $80 \times 150 \times 700 \text{ mm}^3$ for each fibres content were subjected to a RILEM standard test and several concrete cubes $150 \times 150 \times 150 \text{ mm}^3$ were subjected to a standard test of compression.

Specimens	C_i (mm/N)	l (mm)	HO (mm)	α	V_1	E_c (N/mm ²)
TC89-CC00-1	0.0000098	600	15	0.38	2.05	19,484.51
TC89-CC00-2	0.0000129	600	15	0.43	2.37	20,586.27
TC89-CC00-3	0.0000090	600	15	0.42	2.31	27,673.32
TC89-CC00-4	0.0000103	600	15	0.40	2.16	21,051.35

Table 2.5: Values of E_c obtained in accordance with RILEM TC89

Specimen (no.)	P_c (kN)	A_c (mm ²)	R_c (N/mm ²)	Mean R_c (N/mm ²)	Mean f_c (N/mm ²)
Fibres 0 kg/m ³					
1	849.5	22,500	37.76	43.23	35.88
2	1,164.5	22,500	51.76		
3	1,296.5	22,500	57.62		
4	857	22,500	38.09		
5	981	22,500	43.60		
6	1,058	22,500	47.02		
7	900	22,500	40.00		
8	675.5	22,500	30.02		
Fibres 10 kg/m ³					
9	1,454	22,500	64.62	61.38	50.95
10	1,323	22,500	58.80		
11	1,016	22,500	45.16		
12	1,428	22,500	63.47		
13	1,602	22,500	71.20		
14	1,320	22,500	58.67		
15	1,373	22,500	61.02		
16	1,533	22,500	68.13		
Fibres 20 kg/m ³					
1	1,391	22,500	61.82	68.50	56.85
2	1,658	22,500	73.69		
3	1,065	22,500	47.33		
4	1,803	22,500	80.13		
5	1,789	22,500	79.51		
Fibres 40 kg/m ³					
6	1,297	22,500	57.64	55.30	45.90
7	1,282	22,500	56.98		
8	1,191	22,500	52.93		
9	1,270	22,500	56.44		
10	1,181	22,500	52.49		

Table 2.6: Average values of the material compressive strength, f_c , for each fibres content

Beams 80x150x700 mm³ were tested according to RILEM TC89-FMT, which recommends the use of three-point bending notched beams, and the relative load–displacement curves were obtained. From the maximum elastic load of the experimental curves, P_u , the material flexural strength, f_t , was determined according to the expression:

$$f_t = \frac{6M_u}{b(h - a_0)^2} \quad (2.2)$$

where $M_u = P_u l/4$, with the beam span $l = 600$ mm, b is the thickness of the cross-section, h is the beam depth and a_0 is the initial notch depth. The average values of each fibre content are reported in Table 2. .

The notation CCxx refers to fibre contents in kg/m³. Fracture energy was evaluated according to RILEM Technical Committee 50-FMC and the critical stress intensity factor was set to $K_{IC} = 60$ daN/cm^{3/2}. The values of E_c have been obtained on concrete beams without fibres and are reported in Table 2.. The average value of $E_c = 22,199$ N/mm² was utilized for the numerical simulations. The material compressive strength, f_c , for each fibre content was obtained from compression standard tests on concrete cubes 150 x 150 x 150 mm. The single and average values are reported in Table 2.6, where P_c is the resistant crushing force, A_c is the cube crosssection area, R_c is the cubic compressive strength and f_c is the cylindrical compressive strength, with $f_c = 0.83R_c$. As regards the ordinary steel bar reinforcement, the yielding strength, f_y , has been assumed equal to the ultimate strength, f_u , and has been varied with the bars diameter according to Table 2..

Bar diameter	f_y (MPa)	f_u (MPa)
Ø8	484	630
Ø12	572	646
Ø20	503	625

Table 2.7: Average values of steel yielding strength, f_y , and ultimate strength, f_u , by varying the bar diameter

2.2.2 Results and discussion

Now we discuss the results of the experimental campaign, then we check against the Bridged Crack Model. In order to compare the results, the analytical moment M versus rotation ϕ curves have been expressed as load P versus middle-span deflection δ curves, through the following relationships:

$$\delta = \frac{\phi l}{4} + \frac{Pl^3}{48E_c J} \quad (2.3)$$

$$P = \frac{4M}{l} \quad (2.4)$$

where J is the moment of inertia of the beam cross section. The former equation adds the elastic and localized contributions of the beam deflection.

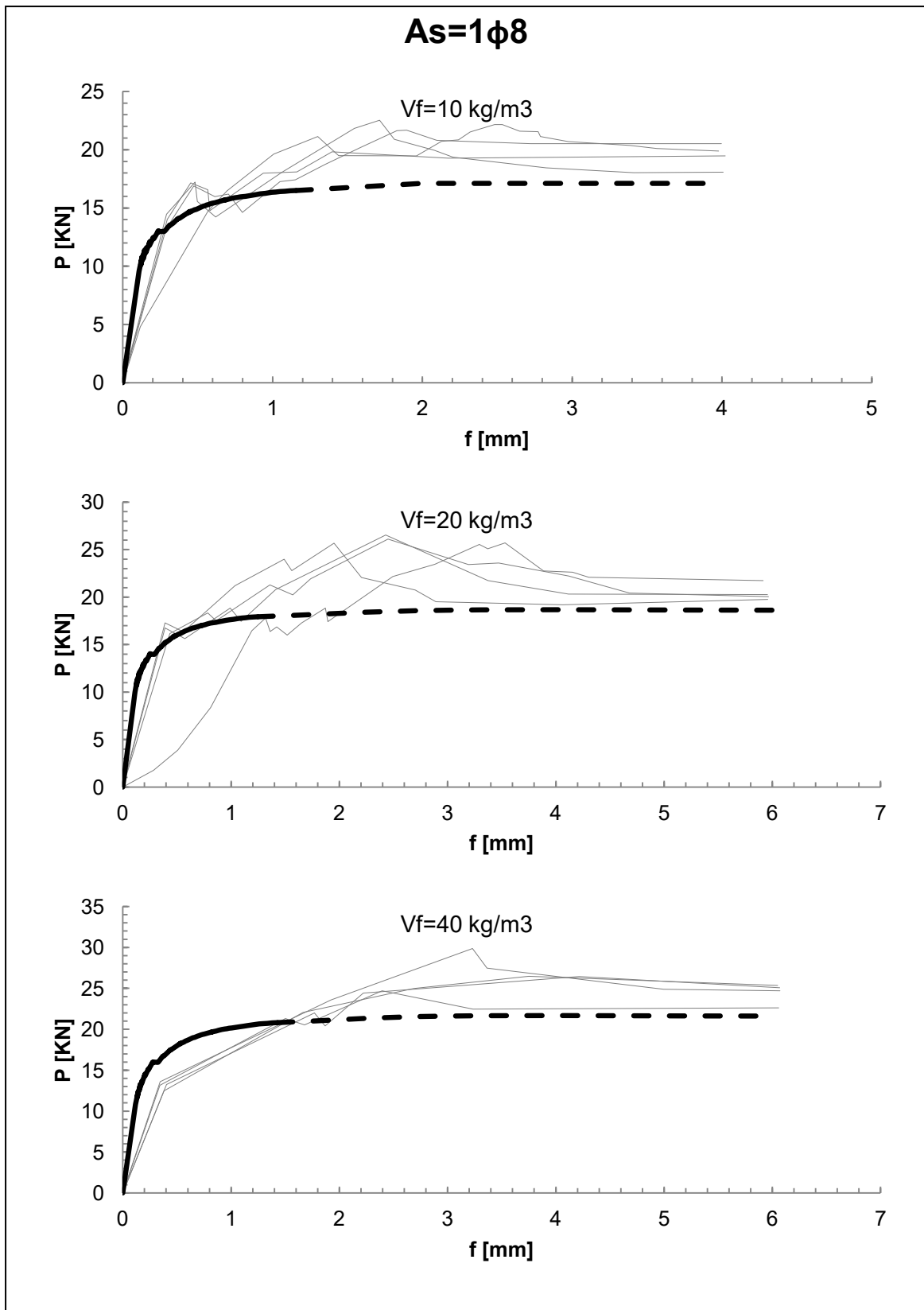


Figure 2.5: Numerical (thicker curve) versus experimental results for a traditional steel bar reinforcement of $1 \phi 8$

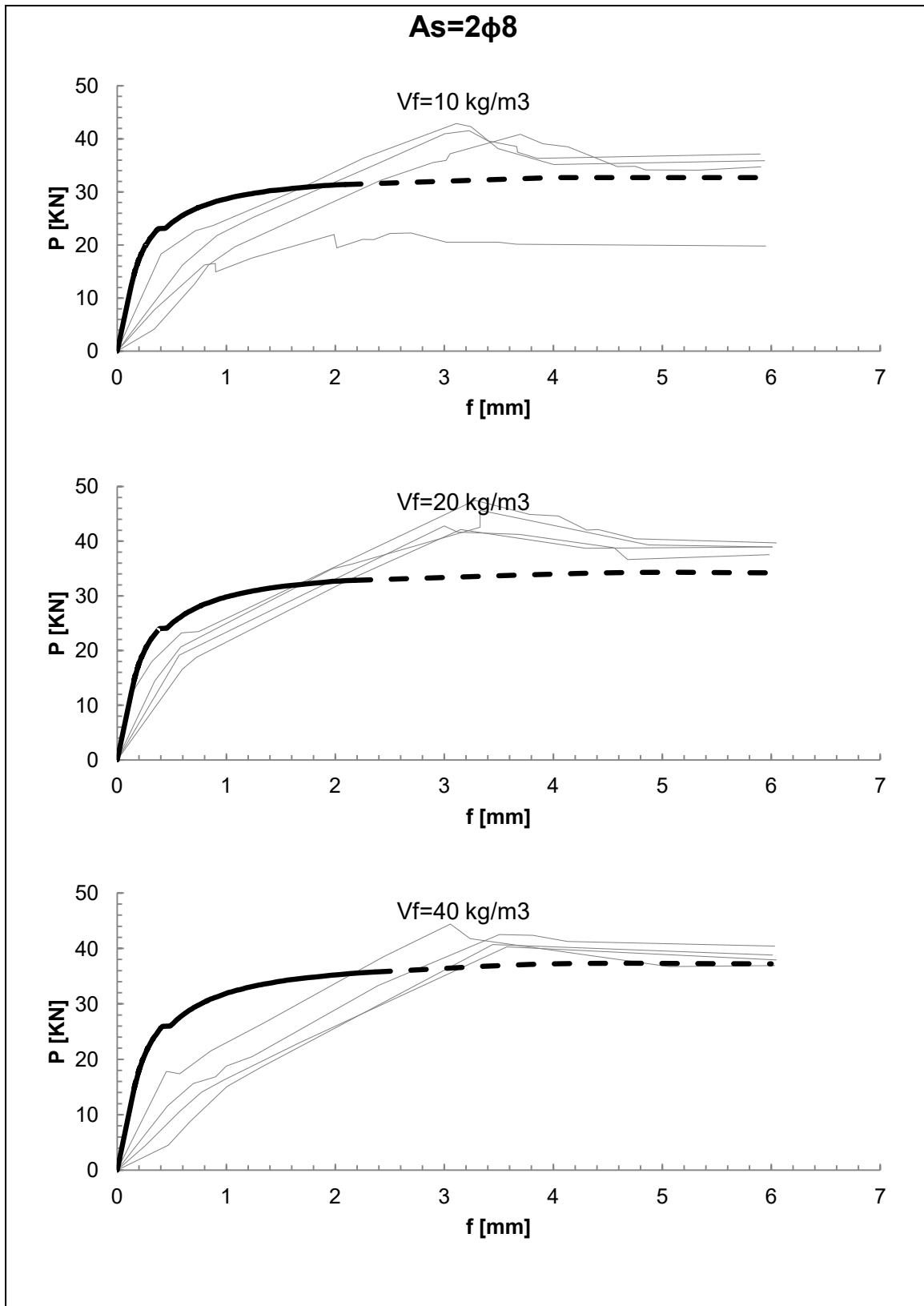


Figure 2.6: Numerical (thicker curve) versus experimental results for a traditional steel bar reinforcement of $2\phi 8$

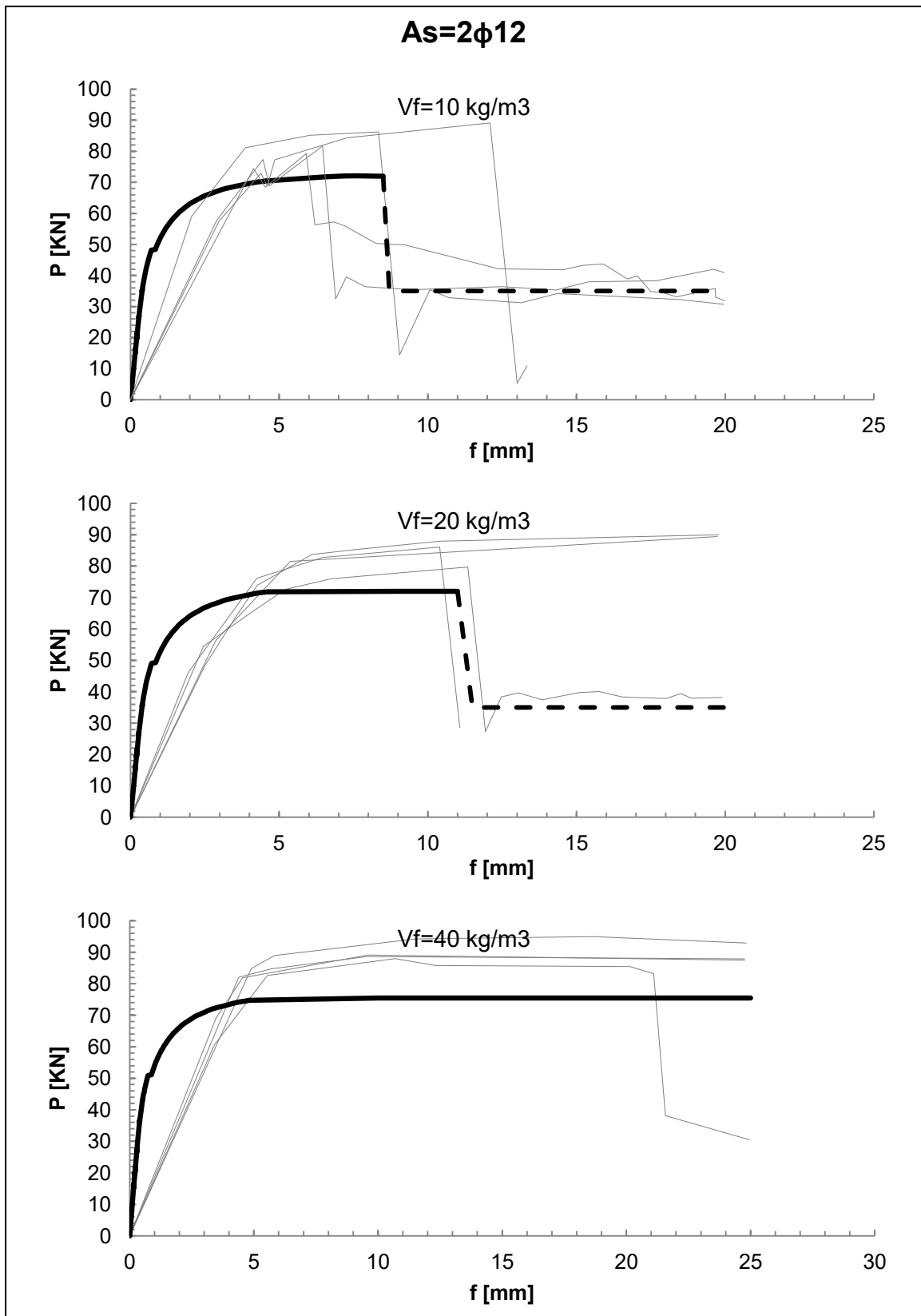


Figure 2.7: Numerical (thicker curve) versus experimental results for a traditional steel bar reinforcement of $2\phi 12$

The influence of the beam weight has been taken into account by considering the contribution of an equivalent applied load of constant value. The experimental values of the deflection had to be purified by the crushing of both the supports at the ends of the beam, by subtracting to the measured value of deflection the mean of the supports settlements, obtaining in this way the true deflection, purified from rigid body motion displacements.

Figs. (2.5), (2.6) and (2.7) represent the experimental versus numerical comparison. Generally, the numerical curves show a good approximation to the experimental results. Depending on the reinforcement percentage, it is possible to observe a transition from a pure flexural collapse to a crushing collapse of concrete in compression. In general, for low reinforcement percentages, such as $q = 0.25$ and 0.50 %, steel yielding precedes crushing of concrete in compression.

The first peak in the moment, M , versus rotation, δ , curve corresponds to the first crack formation, the concrete tensile strength being reached, while the second peak corresponds to steel yielding, which is always followed by a plastic plateau. On the other hand, for high reinforcement percentages, such as $q = 1.13$ and 3.14 %, crushing of concrete in compression precedes steel yielding in tension. In these cases, in fact, the moment, M , versus rotation, δ , curves show a descending branch that indicates the crushing phenomenon.

In the final analysis, the Bridged Crack Model is applied to the study of the flexural behavior of fibre reinforced concrete beams with the concurrent presence of ordinary reinforcement. The experimental versus numerical comparisons demonstrate that the proposed model can be successfully applied to the study of fibre reinforced concrete, revealing the influence of fibre content in the mechanical behavior of the beams in flexure. In fact, a more ductile behavior is evidenced by increasing the fibre content, however there is a threshold over that a further increment in the fibre content is no more favourable. Moreover, a transition in the failure phenomena, from a tensile collapse to a crushing collapse, is revealed by increasing the steel reinforcement.

2.3 Swamy experimental work

Tests are reported on the influence of fiber reinforcement on the deformation characteristics and ultimate strength in flexure of concrete beams made with 20 mm maximum size of aggregates and reinforced with bar reinforcement with specified minimum yield strengths of 460 and 617 N/mm², respectively. The fiber concrete was provided either over the whole depth of the beam or in the effective tension zone only surrounding the steel bars. It is shown that while ultimate strength is increased only marginally, the fibers arrest advancing cracks and increase post-cracking stiffness at all stages of loading up to failure which results in narrower crack widths and substantially less deformation. Last, authors include an ultimate strength theory based on British and American codes and taking into consideration the increased steel strains at failure.

We present below a synthetic overview of the experimental test and we use it to check Bridged Crack Model.

2.3.1 Material and experimental setup

The experimental work consisted of flexural tests on 15 reinforced concrete beams. All the beams were of the same size, 130 x 203 x 2500 mm. The main variables in the tests were the type and amount of tension steel (bar) reinforcement, and the volume and location of fibers in the concrete (Table 2.). Beams DR10 to DR14 and DR20 to DR24 were reinforced with hot-rolled steel reinforcement with a specified minimum yield strength of 460 N/mm². Beams DR10 to DR14 had a steel ratio of 0.99 percent which corresponds to about 50 percent of the balanced steel ratio; Beams DR20 to DR24 had steel ratios of 1.78 percent corresponding to about 90 percent of the balanced steel ratio. Beams DR30 to DR34 were provided with 0.99 percent of cold-worked high tensile steel with a specified minimum yield stress of 617 N/mm². The actual yield strengths of the bars varied from 460 to 470 N/mm² for the 460 steel and from 615 to 617 N/mm² for the 617 steel. The volume of fibers and location of the fiber concrete in the beams were also varied. Two fiber volumes, 0.5 and 1.0 percent, were used. Fibers were used either over the whole depth of the beam or over the effective tension zone of the beam only (i.e., over an area with the steel bars as centroid). All the beams were provided with 6 mm diameter stirrups at 125 mm centers over the whole of their length. Hot-rolled reinforcing bars with a specified minimum yield strength of 410 N/mm² were used for the stirrups. The tie bars for the stirrups at the top of the beams consisted of 10 mm diameter bars of 460 N/mm² specified minimum yield strength.

Beam no.	DR10	DR11	DR12	DR13	DR14	DR20	DR21	DR22	DR23	DR24	DR30	DR31	DR32	DR33	DR34
Type of concrete	A	B	B	C	C	A	B	B	C	C	A	B	B	C	C
Fiber percentage	0.0	0.5	1.0	0.5	1.0	0.0	0.5	1.0	0.5	1.0	0.0	0.5	1.0	0.5	1.0
Cube strength, N/mm ²	36.97 [‡]	39.48 [§]	40.0 [§]	37.50 [‡]	39.24 [‡]	38.88 [‡]	37.3 [§]	40.20 [§]	38.14 [‡]	38.04 [‡]	38.65 [‡]	39.03 [§]	40.88 [§]	37.00 [‡]	37.88 [‡]
Modulus of rupture, N/mm ²	3.48 [‡]	4.72 [§]	6.30 [§]	4.00 [‡]	4.55 [‡]	4.23 [‡]	4.58 [§]	5.91 [§]	4.27 [‡]	4.29 [‡]	4.23 [‡]	4.99 [§]	5.90 [§]	3.67 [‡]	4.24 [‡]
Effective depth, mm	176	176	176	176	176	174	174	174	174	174	176	176	176	176	176
Tension reinforcement	2-12*	2-12*	2-12*	2-12*	2-12*	2-16*	2-16*	2-16*	2-16*	2-16*	2-12'	2-12'	2-12'	2-12'	2-12'
Tension reinforcement, percent	0.99	0.99	0.99	0.99	0.99	1.78	1.78	1.78	1.78	1.78	0.94	0.94	0.94	0.94	0.94

*Torsteel bars $f_y = 460$ N/mm².

†High tensile steel bars $f_y = 617$ N/mm², crimped steel fibers 0.5 x 50 mm.

‡Plain concrete.

§Fiber concrete.

All beams were provided with two 10 mm diameter Torsteel bars in the compression zone.

Overall dimensions of the beams: 130 x 203.2 mm.

Span = 2250 mm.

Concrete types: A = plain concrete.

B = fibers located over whole depth of beam.

C = fibers located in effective tension zone only.

Table 2.8: Details of test beams

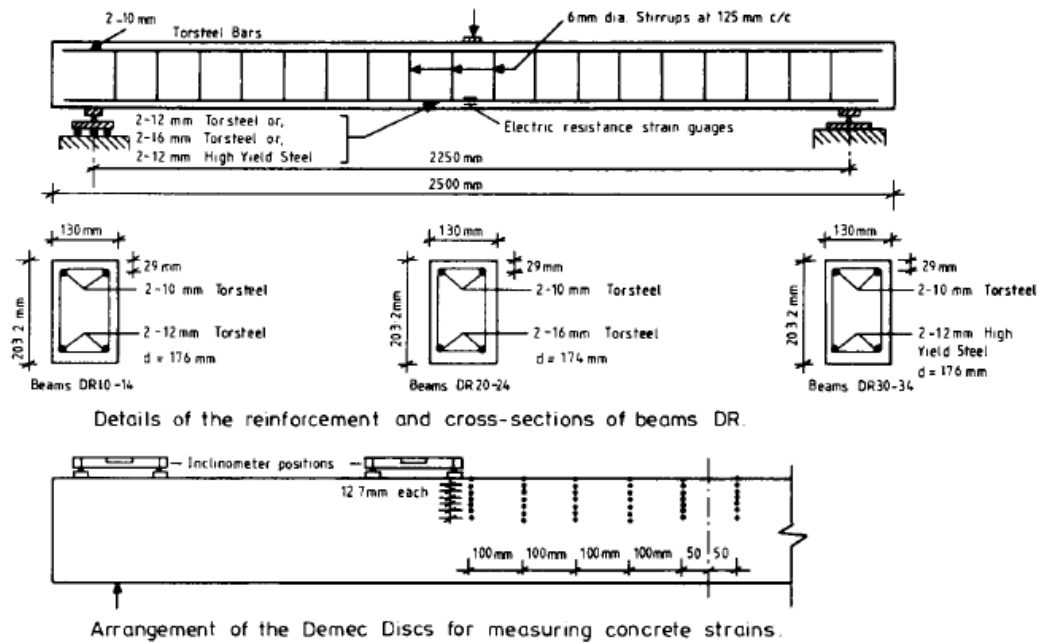


Figure 2.8: Details of test beams and strain measurements

Both the plain and fiber concrete mixes used in the beams were identical except for the presence of fibers in the latter. All concrete mixes contained fly ash, and consisted of mix proportions of 1 (cement + fly ash):2.0 (sand):2.5 (aggregate) with a water (cement + fly ash) ratio of 0.52, all by weight. Ordinary port-land cement was used in all the mixes; the fly ash had a specific surface of $3690 \text{ cm}^2/\text{g}$ and complied with British Standard BS 3892:1965" in chemical composition. The fly ash was used to substitute 30 percent by weight of cement. This ratio has been shown to give the optimum strength and elasticity properties." Natural river sand with a fineness modulus of 2.78 was used in all the mixes. The coarse aggregate was graded river gravel with a 20 mm maximum size; it varied from rounded to angular in shape and had a fineness modulus of 6.52 to 6.65. The steel fibers used in this study were low carbon crimped steel $0.50 \times 50 \text{ mm}$ with a tensile strength of 1050 N/mm^2 and an elastic modulus of 210 kN/mm^2 . A water-reducing agent was used with the fiber concrete mixes at a dosage of 3.2 cc per kg of (cement + fly ash). Typically, the plain concrete mixes had a slump of 130 mm while the fiber concrete mixes with 0.5 and 1.0 percent fiber volumes had slumps of 100 mm and 80 mm, respectively. The fly ash concrete mixes were designed to give about the same one day compressive strength as mixes without fly ash; this one day strength varied from 8.0 to 10.0 N/mm^2 . The plain and fiber concrete mixes were designed to give 35 N/mm^2 at 28 days. The development of compressive strength with time was investigated, and this showed that the strength stabilized at about 500 to 600 days, and that the ratio of the strength at this age to that at 28 days ranged from 1.58 to 1.60. At 1000 days the compressive strength averaged 60 N/mm^2 . The compressive and flexural strengths at 28 days of the concrete in the beams are shown in Table 2.. The compressive strength of the plain and fiber concretes varied from 37.0 to 41.5 N/mm^2 while the modulus of rupture varied from 4.4 to 5.2 N/mm^2 and 5.9 to 6.4 N/mm^2 for concretes with 0.5 and 1.0 percent fiber volumes, respectively. The

28 day static modulus of the plain and fiber concretes was, respectively, 28.13 kN/mm², 28.35 kN/mm² (0.5 percent fiber volume), and 29.82 kN/mm² (1.0 percent fiber volume).

The beams were cast in steel molds and compacted by internal vibration. They were cured, along with control specimens, under uncontrolled internal environment. The beams were tested at 28 days under center point loading over a span of 2250 mm. Extensive measurements of concrete strain, steel strain, deflection, and rotation were taken at various sections of the beam throughout the loading range. Typical location of the various measurements, are shown in Figure 2.8. Therefore a large amount of data was obtained from the tests. Only load-deflection graphs are relevant to this paper and are presented here.

2.3.2 Results and discussion

As shown in Figure 2.9, the increase in the experimental ultimate flexural strength of the beams due to the presence of steel fibers was only marginal, the maximum increase being 10.5 percent, probably due to the very high yield strength bars used in the beams. This is very much less than the reduction in deformation and increase in flexural rigidity obtained with the fibers.

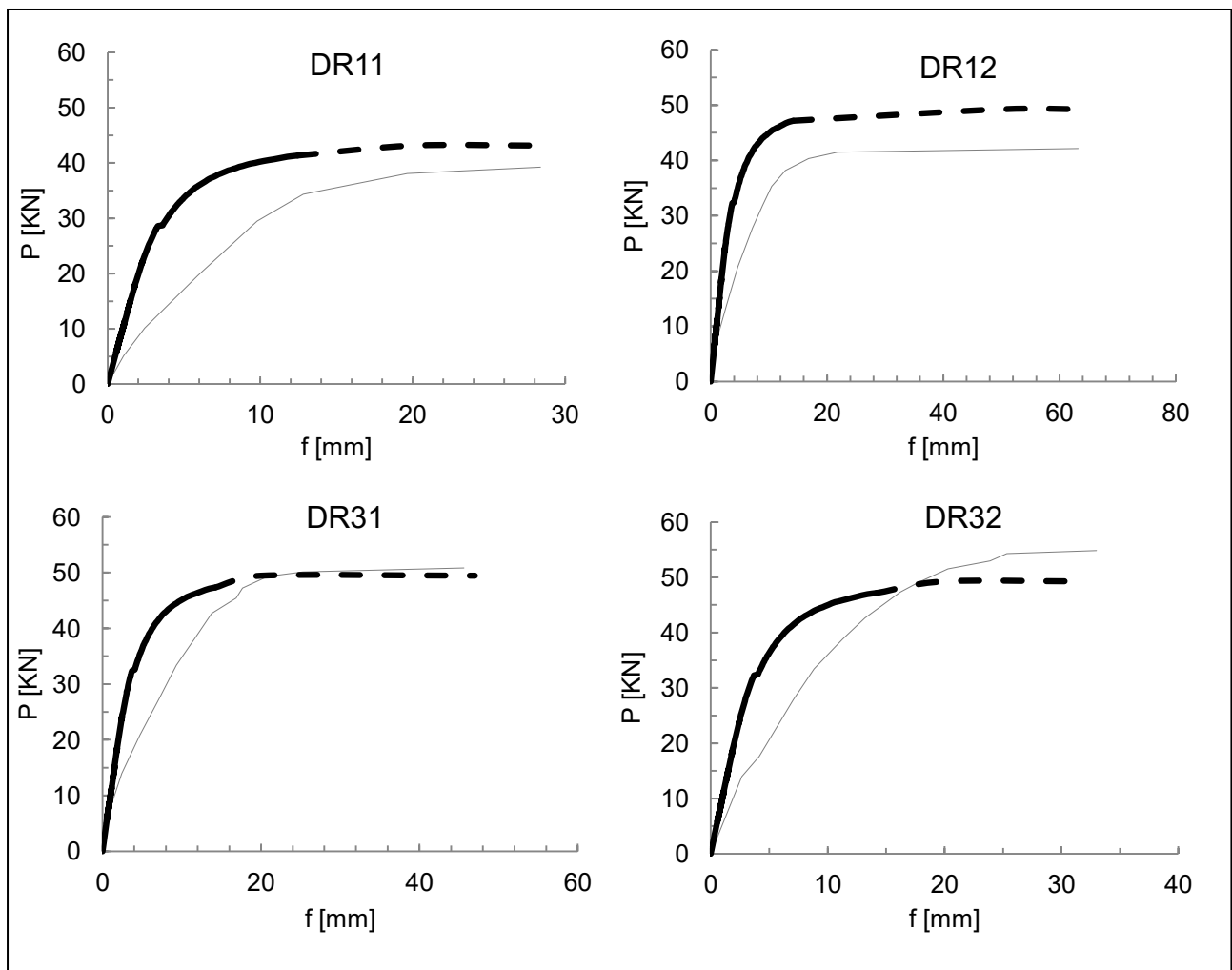


Figure 2. 9: Analytical (thicker curve) versus experimental results, for beams DR11, DR12, DR31 and DR32

It is thus clear that the value of fiber reinforcement lies not so much in strength improvement as in controlling cracking and deformation at all stages of loading, particularly at service loads, and increasing the post-cracking stiffness right up to failure. Since ultimate strength increments are only modest, the use of fibers may not be the most economical means of achieving high ultimate strengths in conventional reinforced concrete beams.

2.4 Olivito experimental work

This paper deals with steel fiber reinforced concrete mechanical static behavior and with its classification with respect to fibers content and mix-design variations. A number of experimental tests were conducted to investigate uniaxial compressive strength and tensile strength. Different mixtures were prepared varying both mix-design and fiber length. Fibers content in volume was of 1% and 2%. Mechanical characterization was performed by means of uniaxial compression tests with the aim of deriving the ultimate compressive strength of fiber concrete. Four-point bending tests on notched specimens were carried out to derive the first crack strength and the ductility indexes. The tensile strength of steel fiber reinforced concrete (SFRC) was obtained both from an experimental procedure and by using an analytical modelling. The experimental tests showed the different behavior of SFRC with respect of the different fiber content and length.

2.4.1 Material and experimental setup

The mixtures adopted for the present work were prepared to provide a cubic compressive strength for concrete higher than 30 N/mm^2 , taking into account all factors affecting the mechanical behavior of fiber reinforced concrete, such as dosage and mechanical properties of components, fibers type, water-to-cement ratio, aggregates quality and dosage, and taking into account the current codes. Six different mixtures were prepared, Tab. (2.9), varying the following parameters: fiber content in volume, fiber length, aggregate fractions and cement content. The aggregates added to the mix were sharp edge type. An accurate sieving has been done by means of square net sieves to obtain the material granulometric curve. In particular, aggregate maximum size was equal to 4 mm and 15 mm for fine and course aggregate respectively. According to CNR DT 204/2006 Guidelines, mixtures granulometric curve has been designed with respect to fiber length: in fact, fiber length and the maximum aggregate size are closely connected to assure a uniform and effective fiber distribution. For this reason, maximum aggregate size should not exceed 0.5 times the fiber length. Portland cement type CEM I, strength class 42.5R, has been used;. Steel fibers were type II supplied from FIBROCEV, Fig. (2.10). Their aspect ratio l_f/d_f (ratio between fiber length and its equivalent diameter) was equal to 50 and their length equal to 22, 30 and 44 mm, Tab. (2.10). Fibers content in volume has been set equal to 1% and 2%, corresponding to 78 and 157 kg/m^3 respectively. Water-to-cement ratio has been set equal to 0.55, such as to provide good mechanical strength and adequate workability of the mixtures. Tab. (2.9) shows the SFRC mix-design, while Tab. (2.10) shows steel fibers properties.

Components e characteristics	Mixtures					
	A1	B1	C1	A2	B2	C2
Cement CEM-I 42.5R (kg/m ³)	400	440	470	400	440	470
Course aggregates 1 (10–15 mm) (kg/m ³)	338	–	–	338	–	–
Course aggregates 2 (10–12 mm) (kg/m ³)	–	155	–	–	155	–
Course aggregates 3 (4–10 mm) (kg/m ³)	534	584	719	534	584	719
Fine aggregates (0–4 mm) (kg/m ³)	909	970	953	909	970	953
Steel fibers 22 mm ($l_f/d_f=50$) (kg/m ³)	–	–	78	–	–	157
Steel fibers 30 mm ($l_f/d_f=50$) (kg/m ³)	–	78	–	–	–	–
Steel fibers 44 mm ($l_f/d_f=50$) (kg/m ³)	78	–	–	157	157	–
Water (kg/m ³)	220	242	258	220	242	258
Fiber content in volume	1%	1%	1%	2%	2%	2%
Water-to-cement ratio	0.55	0.55	0.55	0.55	0.55	0.55

Table 2.9: Mix-design of SFRC

Type	Length (l_f) (mm)	Equivalent diameter (d_f) (mm)	Aspect ratio (l_f/d_f)	Tensile strength (MPa)	Young's modulus (GPa)
F – DUE 22/50	22	0.44	50	360–410	210
F – DUE 30/50	30	0.60	50	360–410	210
F – DUE 44/50	44	0.88	50	360–410	210

Table 2.10: Steel fibers properties

Specimens have been prepared using metallic moulds properly designed. According to the following specimens have been realized:

- Twenty four cubic specimens having dimensions 150 x 150 x 150 mm³, four specimens for each mixture, designated for compressive tests.
- Twenty four prismatic specimens having dimensions 150 x 150 x 600 mm³, four specimens for each mixture, to be subjected to four-point-bending tests.
- Eight prismatic specimens having dimensions 30 x 80 x 350 mm³, only types B and C mixtures with 1% fiber content in volume, at present, to be subjected to direct tensile tests.



Figure 2.10: Steel fibers adopted for the experimentation

Tab. (2.11) shows the number and types of specimens prepared. Mixtures and specimens preparation followed the current codes, both during the mixing and moulds filling phases and during the compaction phase occurred by means of a vibrating board. The slump of fresh reinforced concrete was also measured by means of Abrams cone method (Slump Test) to define its consistency class and designation. Twenty-four hours after the mixtures preparation, the specimens were taken out of the moulds and cured in standard conditions, covering them with damp sand in a closed room at 20 °C temperature and

relative humidity of 90%. Specimens were taken out of the curing room 48 hours before tests started.

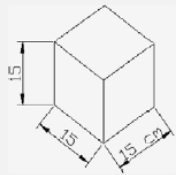
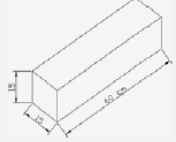
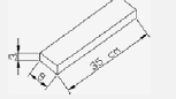
Number of specimens	Type	Dimensions (mm)	Experimental test	Mixture (%)	Specimen scheme
4	Cubic	150 × 150 × 150	Compression	A1	
4	Cubic	150 × 150 × 150	Compression	B1	
4	Cubic	150 × 150 × 150	Compression	C1	
4	Cubic	150 × 150 × 150	Compression	A2	
4	Cubic	150 × 150 × 150	Compression	B2	
4	Cubic	150 × 150 × 150	Compression	C2	
4	Prismatic	150 × 150 × 600	4-Point-bending	A1	
4	Prismatic	150 × 150 × 600	4-Point-bending	B1	
4	Prismatic	150 × 150 × 600	4-Point-bending	C1	
4	Prismatic	150 × 150 × 600	4-Point-bending	A2	
4	Prismatic	150 × 150 × 600	4-Point-bending	B2	
4	Prismatic	150 × 150 × 600	4-Point-bending	C2	
4	Prismatic	30 × 80 × 350	Direct tensile	B1	
4	Prismatic	30 × 80 × 350	Direct tensile	C1	

Table 2.31: Number and type of specimens

Experimental tests were carried out at the Official Materials and Structures Testing Laboratory of University of Calabria. Three different tests were conducted: uniaxial compression tests, direct tensile tests and four-point-bending tests.

In order to evaluate the influence of fibers on concrete strength, four-point-bending tests were conducted on prismatic specimens of dimensions 150 x 150 x 600 mm³, by means of a universal electro-mechanic testing machine with a capacity of 100 kN. The testing machine was connected to a data acquiring device and a personal computer. Load velocity has been set equal to 0.3 mm/min in order to simulate quasi-static conditions. The static scheme adopted allows the specimens to be subjected to bending moment only between loading points, and none shear force, Fig. (2.11a). Loads were disposed at a distance of 150 mm from supports (1/3 of total span) and were applied by means of metallic cylinders of 24 mm diameter, on which a rigid metallic plate was positioned in order to equally distribute the applied load. Specimens were supported by means of other two identical metallic cylinders spaced 450 mm Fig. (2.11b). The whole system was fixed to a steel beam HE 160 A type, 2500 mm long, also fixed to the testing machine. Experimental tests were conducted in crack mouth opening displacement (CMOD) control dealing with steel fiber reinforced concretes. For this reason, after being cured, in the middle part of one side of the specimens, next to the casting surface, a V type notch was made by means of a diamond grinding wheel. The notch was 45 mm deep, such as to have a0/h ratio equal to 0.3 ± 0.01, and width equal to 3–5 mm Fig. (2.11b). Four-point-bending tests were carried out on notched specimens in order to investigate crack opening both at the tip side, crack tip opening displacement (CTOD), and at the bottom side, CMOD, and to define first crack strength and material's ductility indexes D₀ e D₁. Such indexes denote SFRC ductility in a defined range of crack mean opening displacement, included between (0–0.6 mm) relatively to D₀ and (0.6–3 mm) for D₁ index respectively, and are derived from the experimental load–CTOD diagram. For this reason, specimens were properly instrumented. In particular, CTOD was evaluated as the mean value between CTOD₁ and

CTOD₂ checked by means of two linear inductive displacement transducers W₁₀, placed on both lateral sides of the specimens between two Plexiglas bases fixed to the specimens by means of glue as measuring base for strains. CMOD was evaluated by means of a linear inductive displacement transducer W₁₀ placed on bottom side of the specimen. Loading point displacements were investigated by means of four linear inductive displacement transducers W_{A20}, placed on a steel bar fixed to both sides of the specimen along loading direction Fig. (2.11a). All instruments were connected to a data acquiring device to record strains during the test Fig. (2.11b and 2.11c).

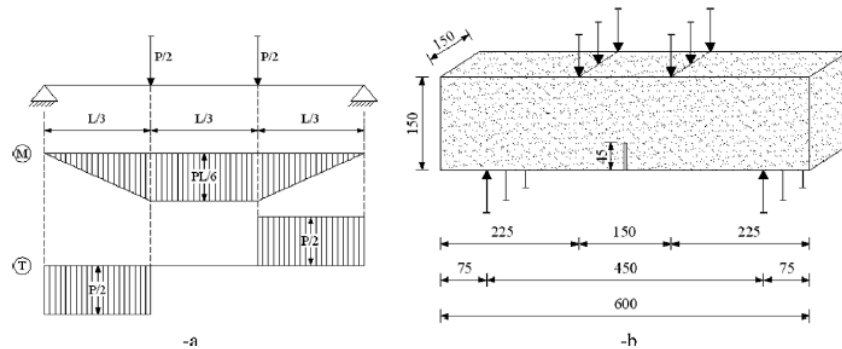


Figure 2. 10: Four-point-bending test. (a) Static condition. (b) Geometry, support and load position

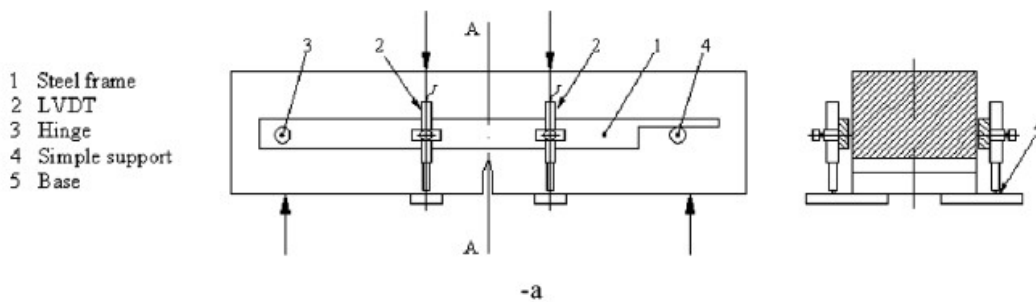


Figure 2.11: Four-point-bending test. (a) Transducers position scheme. (b) Specimen. (c) Experimental equipment

2.4.2 Results and discussion

Four-point-bending tests were carried out on notched specimens in order to classify and characterize the SFRC tested. These kind of experimental tests are usually performed to

investigate fibers performances and to evaluate their possible use for the design of structural members, by means of the derivation of ductility and tenacity of the material. Fig. (2.12a and b) shows load–CTOD_m diagrams related to one specimen for each series tested: from the curves a different mechanical behavior between the series can be seen, due to the different SFRC mix-design.

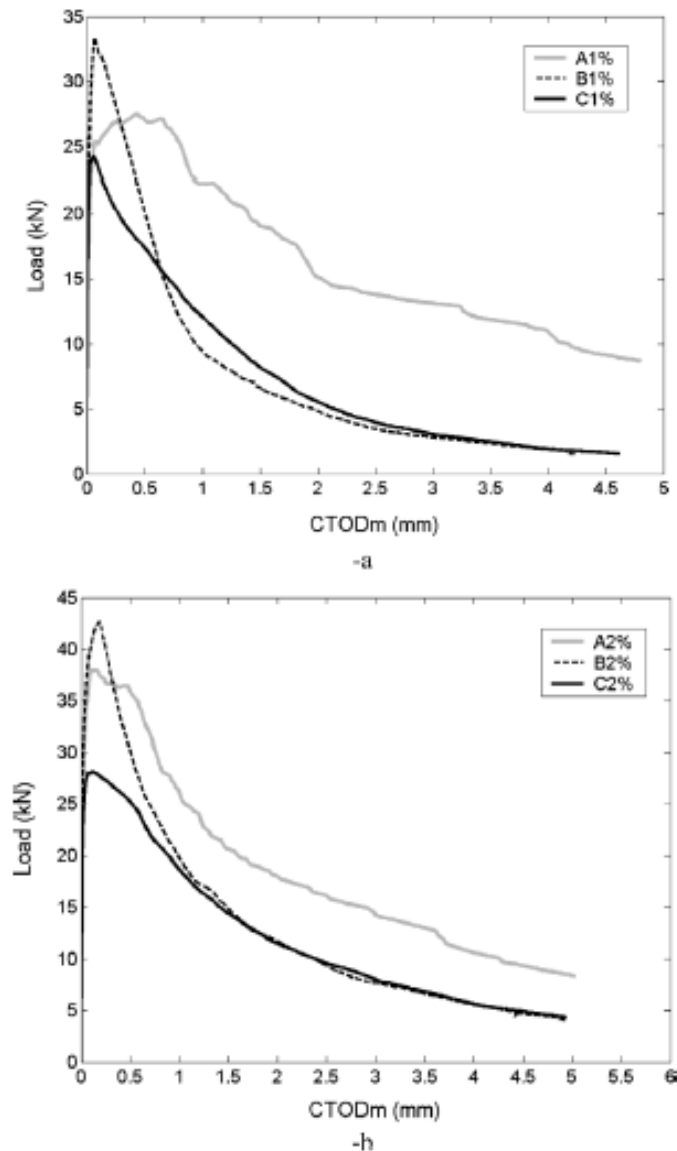


Figure 2.12: Load–CTOD_m diagram. (a) Mixtures with 1% fiber content in volume. (b) Mixtures with 2% fiber content in volume

Such curves also show how A type mixtures, which were realized adding longer fibers to the mix, have a different post-cracking behavior: this can be evaluated in terms of the area under the curve, which is higher for A type specimens. According to the above mentioned codes, first crack strength and ductility indexes were evaluated for the different mixtures from experimental data and from load–CTOD_{net} diagram; CTOD_{net} indicates CTOD mean value deducted of CTOD₀ value (CTOD₀ = CTOD mean value relative to first crack formation for basic normal concrete). Because no experimental tests were conducted on basic normal concrete, CTOD₀ was set equal 0.025 mm as a conventional value.

SFRC first crack strength, f_{lf} , has been derived from the maximum load value (P_{lf}) of load–CTOD_m curve for CTOD included between 0 and CTOD₀, see Fig. (2.13a), by means of the following relationship:

$$f_{lf} = \frac{P_{lf} \cdot l}{b(h - a_0)^2} \text{ [MPa]} \quad (2.5)$$

where P_{lf} is first crack load (N), l is the spacing between supports (mm), b ; the specimen base (mm), h ; the specimen height (mm) and a_0 is the notch depth (mm). Ductility indexes D_0 and D_1 were derived by means of the following equations:

$$D_0 = \frac{f_{eq(0-0,6)}}{f_{lt}} \quad (2.6)$$

where $f_{eq(0-0,6)}$ is the equivalent strength (MPa) calculated when the mean crack opening value is included between 0 and 0.6 mm, $f_{eq(0,6-3)}$ is the equivalent strength (MPa) calculated when the mean crack opening value is included between 0.6 and 3 mm, derived from the following relationships:

$$D_1 = \frac{f_{eq(0,6-3)}}{f_{eq(0-0,6)}} \quad (2.7)$$

where U_1 and U_2 (10^{-3} J) are the areas under load–CTOD_m curve for CTOD_{net} intervals equal to 0–0.6 mm and 0.6–3 mm respectively, Fig. (2.13b). Such areas are approximately proportional to the energy dissipated in the mean crack opening intervals considered. Table (2.12) shows the four-point-bending test results (A₁% first specimen results were not considered due to the fact that the first test was used for the instruments setting operations).

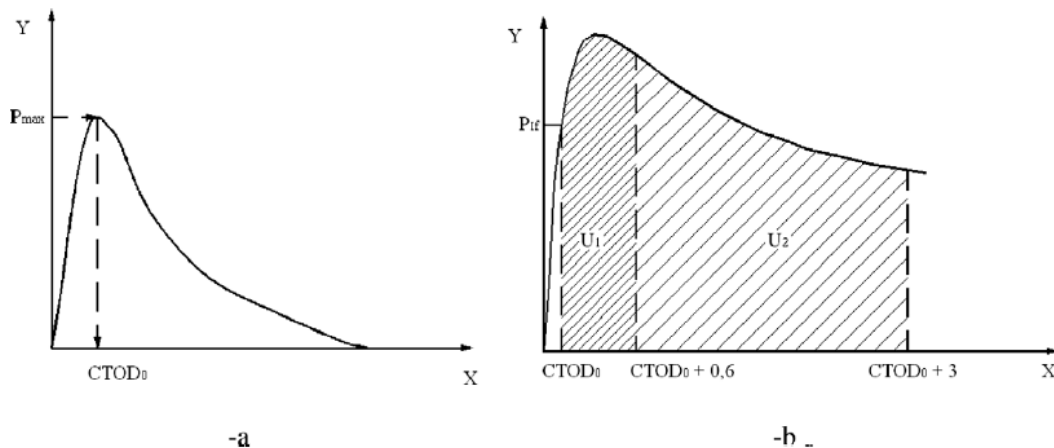


Figure 2.13: (a) Basic concrete load–CTOD_m diagram: CTOD₀ meaning. (b) Load–CTOD diagram: U_1 e U_2 determination

Specimen (%)	P_{fr} (kN)	f_{fr} (MPa)	U_1 (10^{-3} J)	U_2 (10^{-3} J)	$f_{eq(0-0.6)}$ (MPa)	$f_{eq(0.6-3)}$ (MPa)	D_0	D_1
A1_2	21.05	5.73	15,452	41,489	7.01	4.70	1.22	0.67
A1_3	25.90	7.05	18,546	44,368	8.41	5.03	1.19	0.60
A1_4	18.67	5.08	14,598	34,268	6.62	3.89	1.30	0.59
A2_1	22.68	6.17	18,350	51,697	8.32	5.86	1.35	0.70
A2_2	20.98	5.71	19,351	60,592	8.78	6.87	1.54	0.78
A2_3	28.53	7.76	22,741	50,723	10.31	5.75	1.33	0.56
A2_4	23.61	6.42	23,372	92,267	10.6	10.46	1.65	0.99
B1_1	22.81	6.21	14,991	17,753	6.80	2.01	1.10	0.30
B1_2	25.88	7.04	15,251	14,932	6.92	1.69	0.98	0.24
B1_3	28.88	7.86	15,886	10,751	7.20	1.22	0.92	0.17
B1_4	20.21	5.50	13,245	9779	6.01	1.11	1.09	0.18
B2_1	21.46	5.84	19,555	50,876	8.87	5.77	1.52	0.65
B2_2	22.88	6.23	18,446	41,909	8.37	4.75	1.34	0.57
B2_3	29.75	8.10	22,013	41,806	9.98	4.74	1.23	0.47
B2_4	30.59	8.32	21,631	34,196	9.81	3.88	1.18	0.40
C1_1	18.83	5.12	8559	11,333	3.88	1.28	0.76	0.33
C1_2	23.30	6.34	11,870	18,055	5.38	2.05	0.85	0.38
C1_3	25.22	6.86	12,028	13,439	5.45	1.52	0.79	0.28
C1_4	27.24	7.41	11,944	12,036	5.42	1.36	0.79	0.25
C2_1	17.26	4.70	15,334	31,827	6.95	3.61	1.48	0.52
C2_2	22.90	6.23	16,118	35,039	7.31	3.97	1.17	0.54
C2_3	24.22	6.59	16,453	33,504	7.46	3.80	1.13	0.51
C2_4	28.74	7.82	20,977	35,300	9.51	4.00	1.22	0.42

Table 2.42: Four-point-bending test results

In conclusion, the present experimental analysis was carried out in order to investigate steel fiber reinforced concrete mechanical behavior with respect to mix-design variations and different fiber content in volume values. From the experimental results, an important aspect could be noticed, which is the ductility and tenacity increase of SFRC when fiber content in volume increases and, at the same fiber content, when fiber length increases. This phenomenon is due to the higher deformability and energy absorption of SFRC during the cracking phase; SFRC shows a higher bending stiffness and a different cracking pattern than normal concrete. Moreover, post-cracking behaviour is affected by the different fiber length: in fact, specimens realized with short fibers showed a softening behaviour, while specimens realized longer fibers showed a plastic or a hardening behaviour as well as a maximum load increment. Therefore, an increment of fiber content in volume produces: ductility, first crack strength and flexural strength increase, but none indicative variation for compressive strength.

2.5 Kang experimental work

This paper presents a study of the tensile fracture properties of Ultra High Performance Fiber Reinforced Concrete (UHPFRC) considering the effects of the fiber content. To investigate the impact of fiber content, notched 3-point bending tests were executed, where the fiber volume ratio was varied from 0% to 5%. From the bending tests, it was found that the flexural tensile strength of UHPFRC linearly increases with increasing fiber volume ratio and the rule of mixture can be applied to UHPFRC. Furthermore, an inverse analysis was performed to determine the tensile fracture model of UHPFRC and a tri-linear tensile softening model is suggested. The suggested model successfully represents the increase of the stress-constant bridging zone and the decrease of the stress-resisting zone with increasing fiber content. The proposed model for various fiber content levels is simple and versatile and can be readily applied to structural design or numerical analysis of UHPFRC.

Cement content (kg/m ³)	Relative weight ratios to cement						Steel fiber ^a (V _f , %)
	Cement	Water	Silica fume	Fine aggregates	Filler	Superplasticizer	
821.7	1.00	0.25	0.25	1.10	0.30	0.018	0
813.1							1
804.9							2
796.7							3
788.5							4
780.3							5

Table 2.53: Mix design of UHPFRC

Material	Specific surface (cm ² /g)	Density (g/cm ³)	Chemical composition (%)					
			SiO ₂	Al ₂ O ₃	Fe ₂ O ₃	CaO	MgO	SO ₃
OPC	3413	3.15	21.01	6.40	3.12	61.33	3.02	2.3
Silica fume	200,000	2.10	96.00	0.25	0.12	0.38	0.1	-

Table 2.14: Physical and chemical properties of cement and silica fume

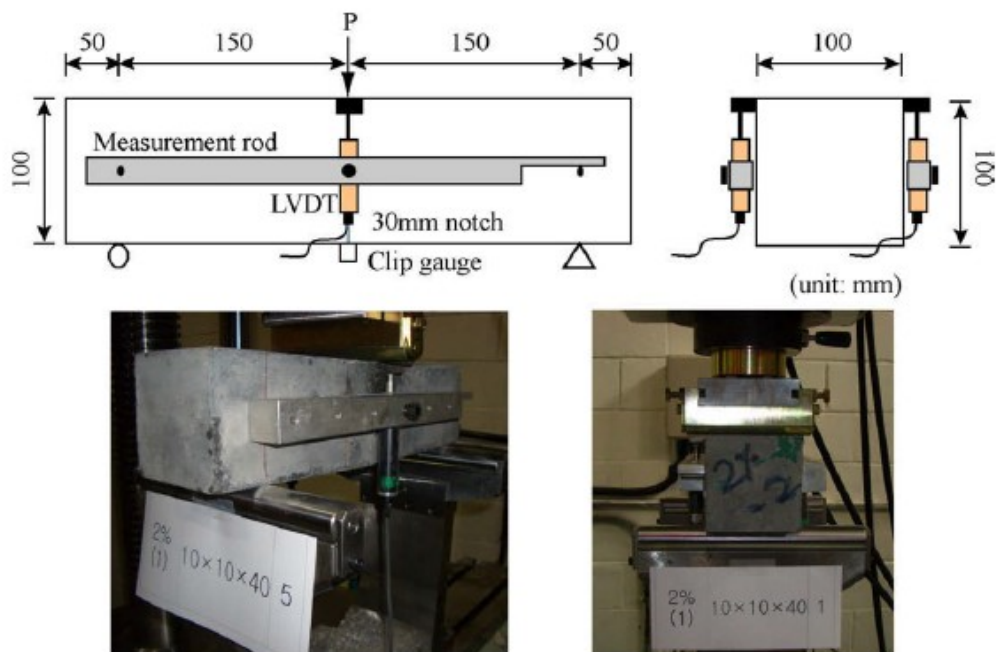


Figure 2.34: Specimen configuration and experimental setup

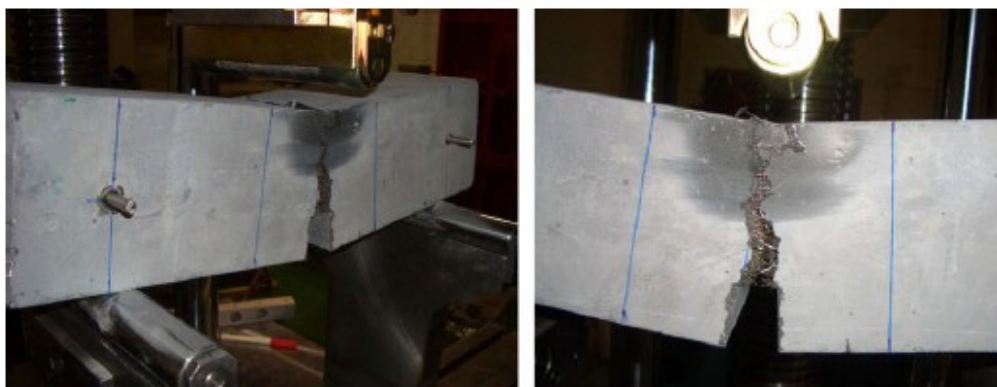


Figure 2.45: Failure configuration after test

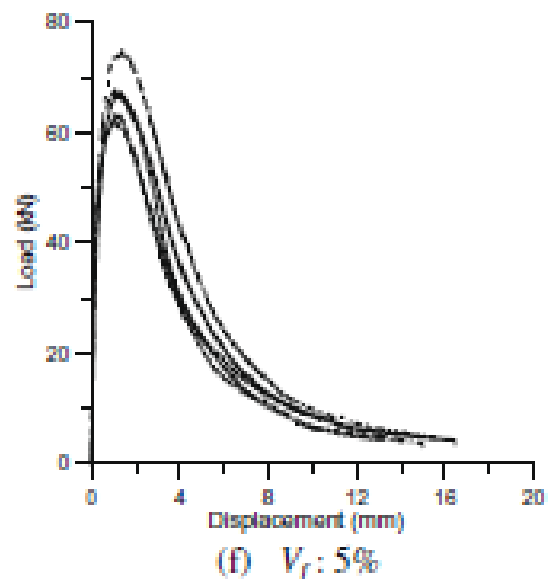
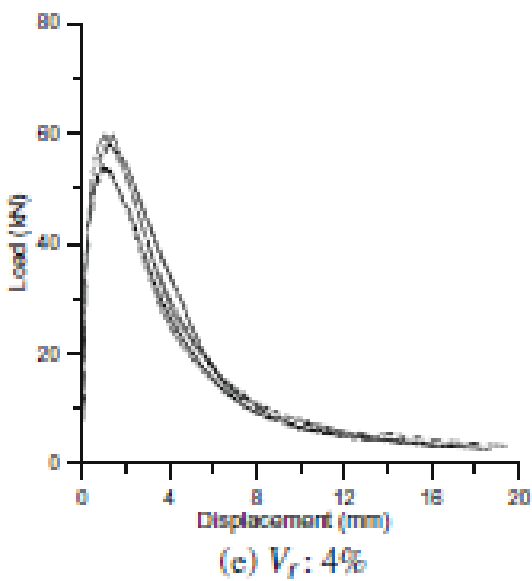
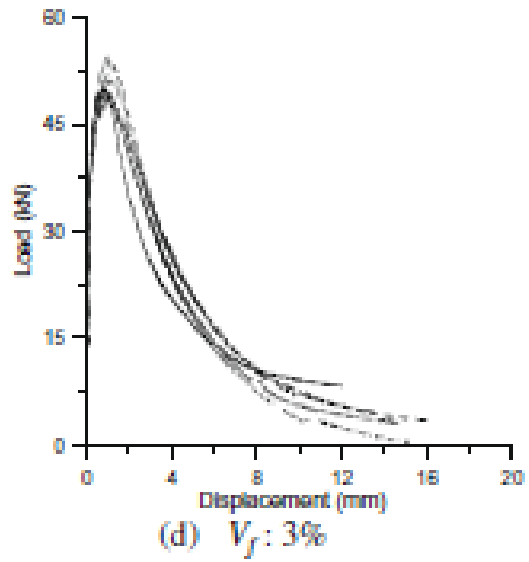
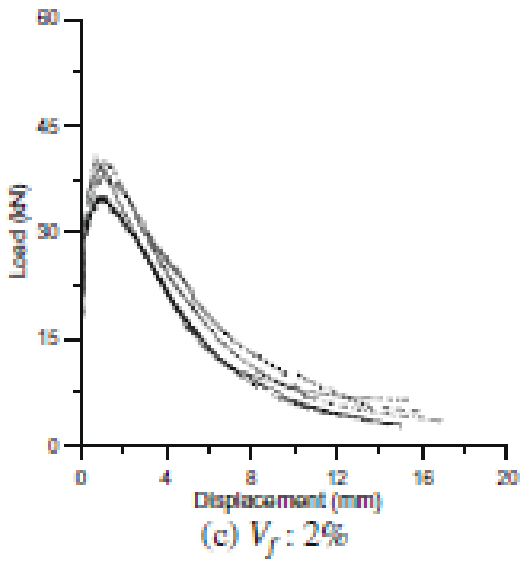
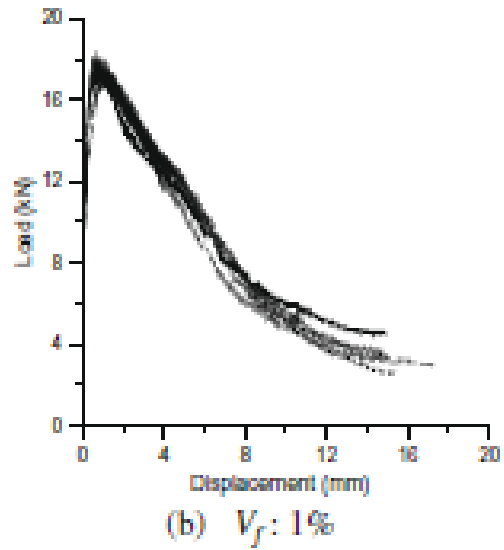
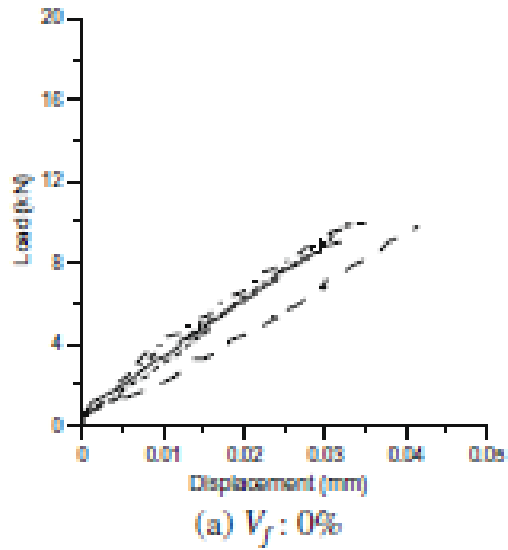


Figure 2.165: Load–displacement experimental results

2.5.1 Material and experimental setup

The mix design of UHPFRC differs significantly from that of normal and high-strength concretes. UHPFRC mix compositions are characterized by high cement, superplasticizer, and silica fume content. The concrete mixture proportions applied in this study are tabulated in Tab. (2.13). The water–binder ratio is determined as $w/b = 0.20$, and a high percentage of silica fume (25% of cement weight) is implemented. Furthermore, in order to achieve sufficient strain-hardening behavior, various percentages of steel fibers in excess of 1% were incorporated. In this study, fiber content was selected as the main test variable and was classified into five groups corresponding to volume ratio, which was increased in increments of 1% from 1% to 5%. Generally, the use of filler through the partial replacement of cement provides enhanced strength at early age and durability. Therefore, siliceous filler was used in the concrete mix design. More specific material characteristics used in the concrete mix are as

- (1) Cement and reactive powder The cement and reactive powder adopted in this study are ordinary Portland cement (OPC) and silica fume, the physical and chemical properties of which are listed in Tab. (2.14).
- (2) Aggregates Fine aggregates with a density of 2.62 g/cm^3 and sand with a mean particle size below 0.5 mm were utilized. Coarse aggregates were not used.
- (3) Superplasticizer Polycarboxylate superplasticizer (density 1.01 g/cm^3 , dark brown) was used.
- (4) Filler Siliceous filler with a mean particle size of 26.6 μm was applied.
- (5) Steel fibers High strength steel fibers (density 7.8 g/cm^3 , length 13 mm, diameter 0.2 mm, tensile strength 2500 MPa) were selected to improve toughness with respect to the tensile and flexural behavior.

The test methods employed to determine the tension softening property of UHPFRC are the bending test, uniaxial tensile test, and compact tension (CT) test, corresponding to those widely applied for ordinary concrete. Among them, the bending test is the most widely adopted method, owing to its simplicity. While the uniaxial tensile test offers the advantage of directly determining the tension softening curve, difficulties are encountered in securing accuracy. The CT test presents a noticeable advantage in being practically free from the effects of the self-weight of the specimen owing to the large failure area produced in specimens with small volumes. However, with this method the tension softening curve is determined indirectly, as with the bending test, and is rarely applied due to the need of special equipment. This study performed a 3-point bending test for the determination of the tension softening properties and curves of UHPFRC. For each concrete mixture shown in Tab. (2.13), five test specimens with dimensions of 100 mm x 100 mm x 400 mm are manufactured. The specimens were cut with a notch at mid-length using a diamond cutter prior to the execution of the test and after completion of concrete curing. The notch was set with a constant width of 4 mm. A universal testing machine with a capacity of 2000 kN was used for the bending test. Load was applied through displacement control at a speed

of 1/1500 of the specimen span length (300 mm) per minute. One LVDT with a capacity of 10 mm was installed at both sides to measure the deflection of the center of the specimen during the test. A clip gage was attached at the bottom of the specimen to measure the crack width at the notch. Fig. (2.14) illustrates the characteristics of the bending test specimens and equipment.

2.5.2 Results and discussion

Fig. (2.15) shows a typical failure configuration after the 3-point bending test. After failure, it is shown that one large crack exists, accompanying fibers, which play an important role in bridging two crack faces. Due to the bridging mechanism of fibers, UHPFRC can provide superior performance especially under tension as compared to UHPC without fibers. Fig. (2.16) shows the experimentally obtained load–displacement curves with respect to fiber volume ratios. As seen in Fig. (2.16), higher fiber volume ratio results in larger scatter among the load–displacement curves for the same fiber volume. The large scatter with a high volume ratio is attributed to the intrinsic scatter at high strength levels and the degree of dispersion of fibers. Fig. (2.17) presents a comparison of load–displacement curves for five fiber volume ratios. It is revealed that the initial stiffness does not undergo a significant change with an increase of fiber content, while the maximum load increases gradually together with a gradual change to brittle behavior in the softening section. Although the structural ductility increases with fiber content for FRC, the displacement at peak load does not have an obvious trend with the fiber volume ratios in the case of UHPFRC.

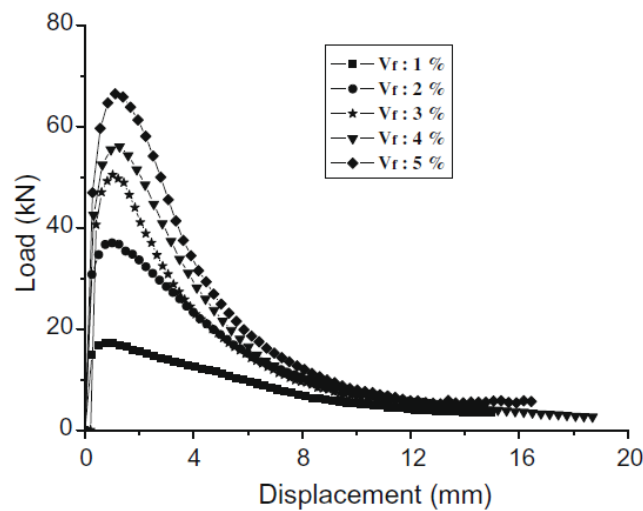


Figure 2.176: Load–displacement curves with respect to fiber volume ratio

However, it is seen that UHPFRC reflects the superior behaviors of both UHPC and FRC with respect to high strength and ductility, respectively. The flexural strength of UHPFRC was obtained by Eq. (2.8).

$$\sigma_b = \frac{3P_{max}L}{2b(h - a_0)^2} \quad (2.8)$$

where P_{max} is the maximum load; b and h the beam thickness and height, respectively; a_0 the notch depth and L is the span length. With the development of FRC, the tensile performance of FRC in comparison with that of ordinary concrete has been studied by many researchers. Shah and Rangan, Naaman, Swamy et al. and Mai suggested the rule of mixture to consider the fiber content in calculating the flexural strength for FRC, given below as Eq. (2.9).

$$\sigma_{bf} = A\sigma_{bf0}(1 - V_f) + BV_f(l_f/d_f) \quad (2.9)$$

where σ_{bf} and σ_{bf0} is the flexural strength with fiber and without fiber, respectively; V_f the fiber volume ratio; l_f and d_f the length and diameter of fiber, respectively; and A and B is the experimental coefficients. Eq. (2.9) shows the linear dependence of the flexural strength (σ_{bf}) of FRC on the fiber volume ratio (V_f) and fiber shape (l_f/d_f). Rearranging each term in Eqs. (2.9) and (2.10) can be obtained to clarify this linearity.

$$\sigma_{bf} = V_f[B(l_f/d_f) - A\sigma_{bf0}] + A\sigma_{bf0} \quad (2.10)$$

For a given fiber geometry (l_f/d_f), the flexural strength (σ_{bf}) is solely linearly dependent on the fiber volume ratio (V_f). It should, however, be verified that Eq. (2.10) for FRC is directly applicable to UHPFRC, which has an ultra-high concrete matrix strength and a relatively lower contribution of fiber than conventional FRC. The experiments performed in this study cover a large range of fiber volume ratios, from 1% up to 5%, and therefore the fiber content contribution to flexural strength can be examined with this equation.

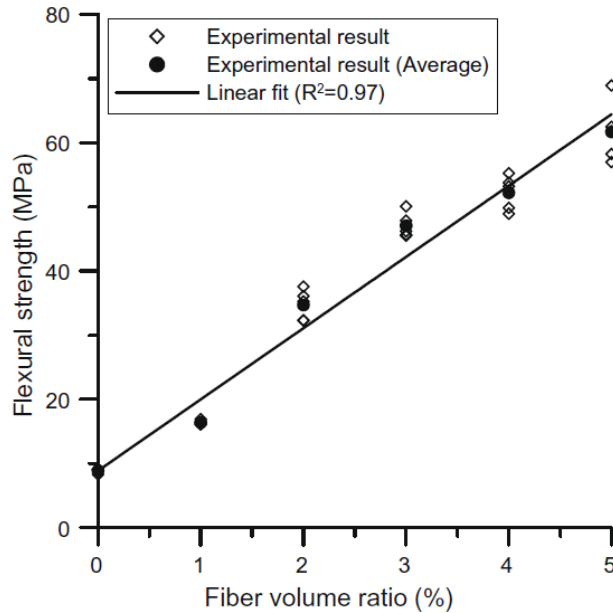


Figure 2.18: Variation of flexural strength with respect to fiber volume ratio

Fig. (2.18) shows the relationship between the average flexural strength and the corresponding fiber volume ratio obtained from the experiment. The flexural strength of UHPFRC is linearly dependent on the fiber content with high reliability, i.e. the coefficient of determination (R^2) is 0.97.

Formularizing this relationship, Eq. (2.11) is obtained as follows:

$$\sigma_{bf} = 11.1V_f + \sigma_{bf0} \quad (2.11)$$

where $\sigma_{bf0} = 8.88$ (MPa) and V_f is the fiber volume ratio by percentage.

For the same fiber geometry ($l_f/d_f = 13/0,2$) used in this study, comparing Eq. (2.11) with Eq. (2.10), the experimental coefficients A and B can be deduced as 1.0 and 0.307, respectively. From the above derivation of Eq. (2.11), it is concluded that the rule of mixture for flexural strength represented by Eq. (2.9) can be applied to UHPFRC with satisfactory confidence under the same fiber geometry conditions.

In conclusion, this study investigated the effects of fiber content on the tensile fracture behavior of UHPFRC and a numerical model is suggested based on the experimental results.

From notched 3-point bending tests, it is observed that the flexural tensile strength of UHPFRC linearly increases as the fiber volume ratio increases from 0% to 5% and the rule of mixture holds for the flexural strength of UHPFRC.

3. Experimental validation of the Bridged Crack Model

Since the results of the bibliographic research have provided a limited number of figures, an experimental campaign has been carried out during my thesis. This work has been made possible through the collaborative effort with AZICHEM srl and FABLAB TORINO. In this chapter, the experimental work conducted during the past months at Fracture Mechanics Laboratory of Politecnico di Torino is described in detail.

It must be said that, not all the specimens made have yet been tested. Nevertheless the work will be continued in the future.

3.1 Material

The experimental work consisted on flexural tests on 24 fiber reinforced concrete beams (Fig 3.1): 12 FRC beams were made of pre-dosed concrete for structural use, BETONPIU'-GRAS CALCE srl, with an elastic modulus of 210 kN/mm^2 and a compressive strength of 30 N/mm^2 at 28 days.

Steel fibers, supplied from AZICHEM srl, have been adopted in this case. In order to have an efficient control of the cracking process, three different types of steel fiber reinforcement have been considered (Fig 3.2): READYMESH MX-500, READYMESH MS-350 and READYMESH MM-150. A specific yield strength equal to 1100 N/mm^2 and a diameter equal to $0,75 \text{ mm}$ characterizes these fiber reinforcements. Length varies from $1,5 \text{ mm}$ to 5 mm . As shown in Tab. 3.1, fibers MX-500 and MM-150 have been used to carry out the $20 \times 10 \text{ mm}$ and $10 \times 10 \text{ mm}$ beams. On the other hand, $5 \times 5 \text{ mm}$ beams have been provided with MS-350 and MM-150 fibers.



Figure 3.1: Overview of some of specimens realized in this Master Thesis work



Figure 3.2: Detail of the steel fibers adopted for the experimentation, from left to right: READYMESH MX-500, READYMESH MS-350 and READYMESH MM-150

	Length [mm]	Diameter [mm]	E [N/mm ²]	f _y [N/mm ²]
MX-500	5	0,75	210000	1100
MS-350	3,5	0,75	210000	>1100
MM-150	1,5	0,75	210000	>1100

Table 3.1: Steel fibers proprieties

The main variables in the tests were the beam size and the volume of the fibers in the concrete (Tab 3.2). Three beam sizes have been considered: 5 x 5 x 30 cm; 10 x 10 x 60 cm; 20 x 10 x 120 cm. All the three were provided with initial notch (Fig. 3.3).

Fiber reinforcements, with the aim of investigate the minimum reinforcement content, have been added to the concrete matrix in four different volume fractions: 0.08%; 0.20%; 0.96%; 1.28%. In the notation FCR-xx-yy, xx and yy refer to the beam size and the fiber volume fraction respectively.

ID	Height h [cm]	Depth b [cm]	Length L [cm]	Notch a [cm]	Fibers tot.		Fiber MX-500	Fiber MS-350	Fiber MM-150
					V _f [%]	V _f [kg/m ³]			
FRC-5-04	5	5	30	1,5	0,08	6,2	-	4,2	2,1
FRC-5-15					0,20	15,6	-	10,4	5,2
FRC-5-75					0,96	74,9	-	49,9	25,0
FRC-5-100					1,28	99,8	-	66,6	33,3
FRC-10-04	10	10	60	3	0,08	6,2	4,2	-	2,1
FRC-10-15					0,20	15,6	10,4	-	5,2
FRC-10-75					0,96	74,9	49,9	-	25,0
FRC-10-100					1,28	99,8	66,6	-	33,3
FRC-20-04	20	10	115	5	0,08	6,2	4,2	-	2,1
FRC-20-15					0,20	15,6	10,4	-	5,2
FRC-20-75					0,96	74,9	49,9	-	25,0
FRC-20-100					1,28	99,8	66,6	-	33,3

Table 3.2: Mix design of Steel Fiber Reinforced Concrete

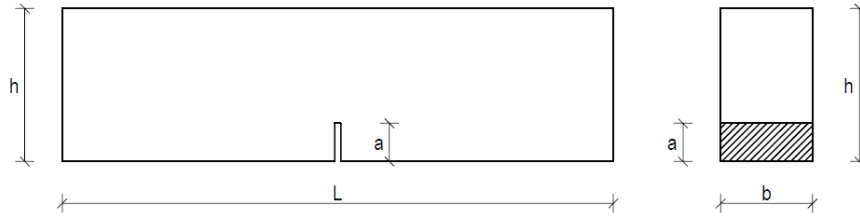


Figure 3.3: Specimens geometry

The second stage of the experimental campaign involves 12 FRC beams made of high performance concrete ($R_{ck} > 120 \text{ N/mm}^2$) and brass fiber reinforcements ($f_y = 135 \text{ N/mm}^2$), both provided by AZICHEM srl. Also in this case, three beam sizes have been considered: 5 x 5 x 30 cm; 10 x 10 x 60 cm; 20 x 10 x 120 cm. Four specimens have been made for every size but the volume of the fibers in the concrete has been kept constant and equal to 120 kg/m^3 (1,54%) in this second batch. Due to their enhanced high-bonding capability, brass fibers are supposed to increase the load carrying capacity of FRC members. Brass fibers substantially reduce the brittleness of the concrete matrix, and improve its engineering properties, such as tensile, flexural, impact resistance, fatigue, load bearing capacity after cracking, and toughness.

3.2 Experimental results and numerical simulations

In order to evaluate the influence of fibers on the cracking of concrete, three point bending tests were conducted on specimens by means of a electro-mechanic testing machine with a capacity of 250 kN. The test machine was connected to a data acquiring device and a personal computer. Load velocity has been set equal to 0.4 mm/min in order to simulated quasi-static conditions. Loads were applied by means of metallic cylinder and specimens were supported by means of others two identical metallic cylinders. The span length has been set equal to $L_{span} = 0,95L$. Figs. (3.4) and (3.7) illustrate the various stages of the test, from the removal of the scaffolding to the end of the three-point bending test.

Experimental tests were conducted in deflection control and the results have been expressed as load P versus middle-span deflection δ . In figs. (3.8) and (3.9), experimental results (grey curves) are reported and compared to analytical figures obtained by implementing a slippage constitutive law to the fiber content (black curves). In most cases analytical curves show a good approximation to the experimental ones. A less good approximation is evidence for small specimens, it might be due to dimensional scale effect Eq. (1.88). Nonetheless there has been success in predict the amount of fiber required to attain the minimum reinforcement condition in both cases, about 75 kg/m^3 .

To sum up, the experimental versus numerical comparisons demonstrate that the proposed model can be successfully applied to the study of fiber reinforced concrete, revealing the influence of fiber content in the mechanical behavior of the beams in flexure. In fact, it can be clearly seen that the collapse mechanism shows a transition from brittle to ductile as the fibers content increases.



Figure 3.4: Process of the removal the scaffolding

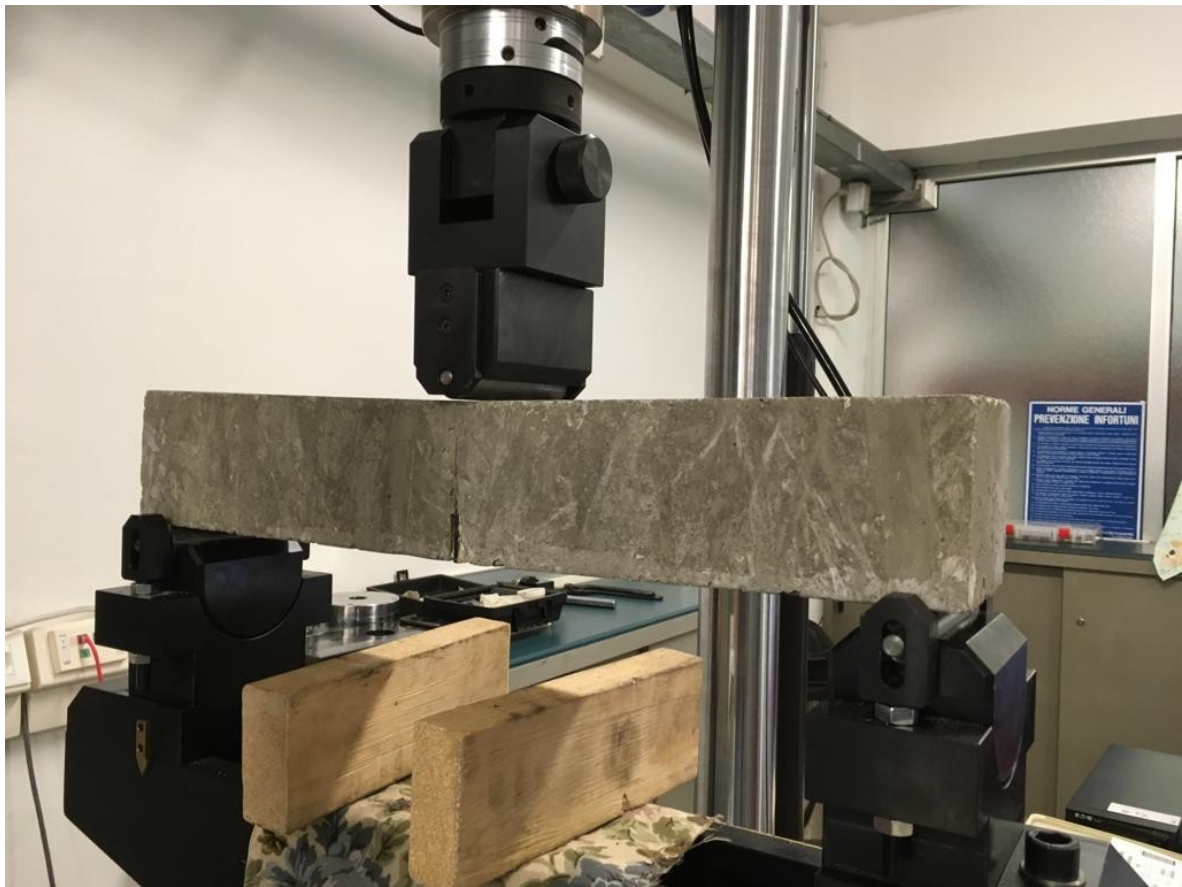


Figure 3.5: Three-point bending test setup

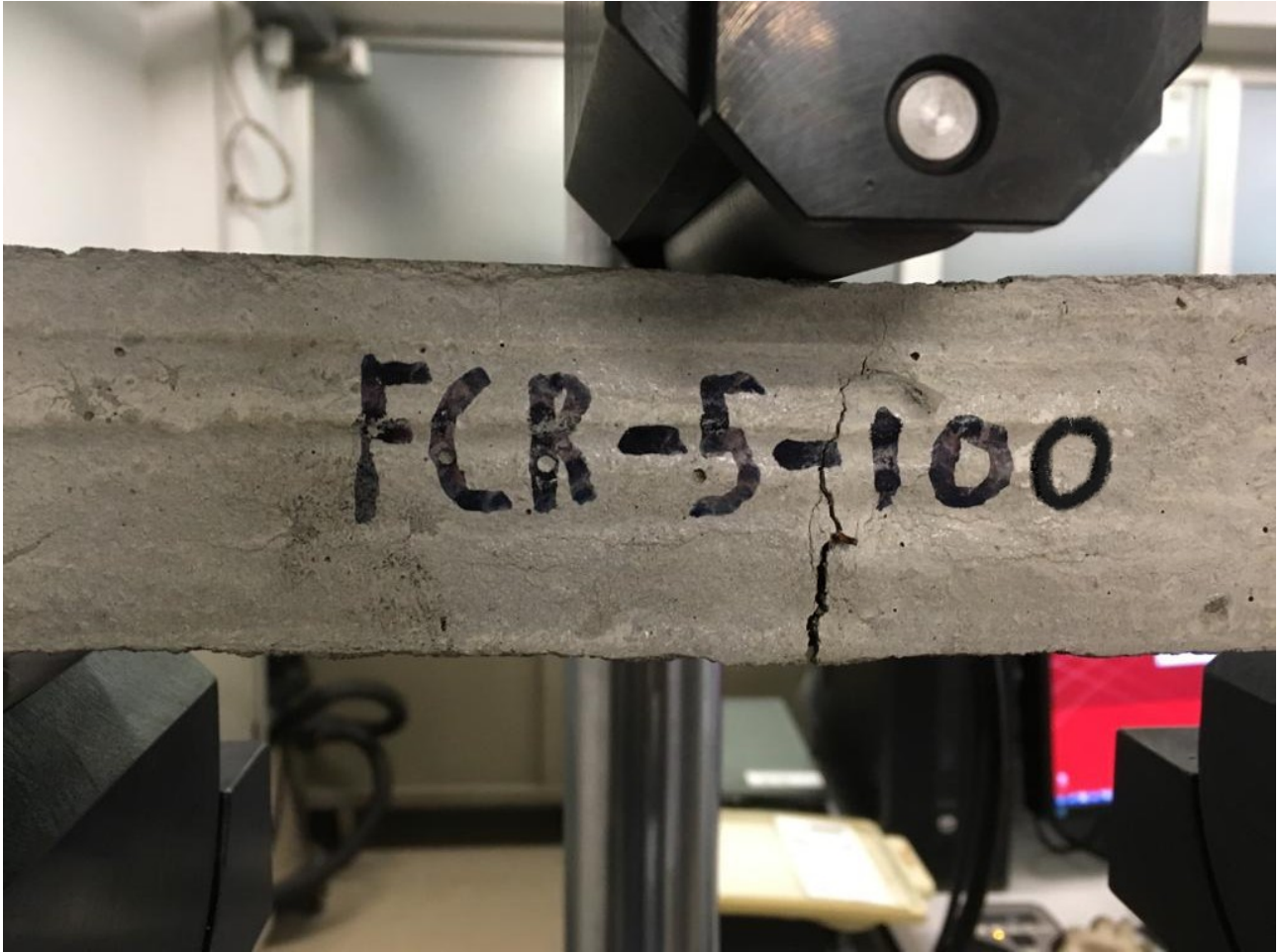


Figure 3.6: Detail of crack advancement



Figure 3.7: Failure of the specimen

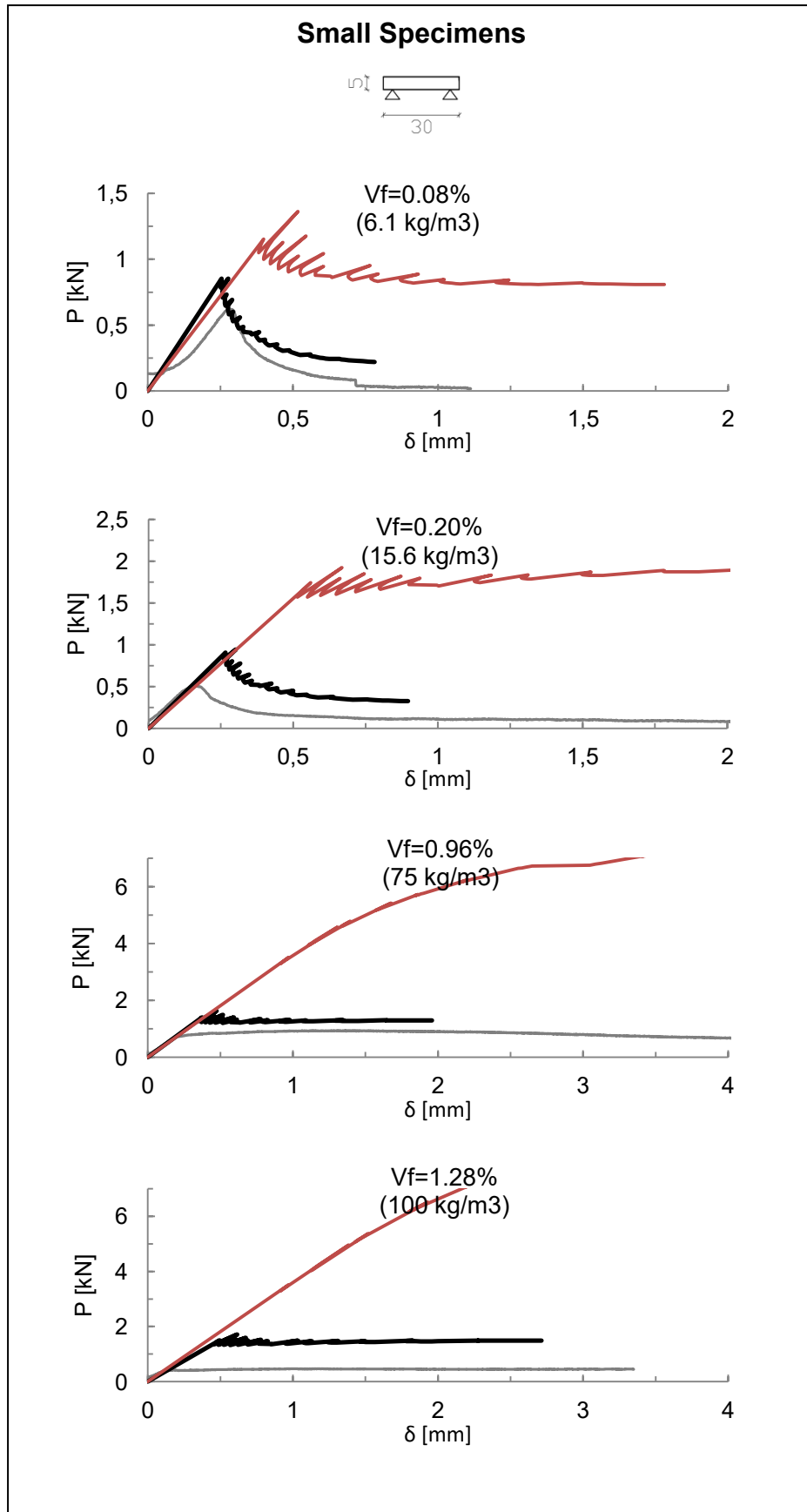


Figure 3.8: Experimental (grey) versus analytical results from bending tests on 5x5x30 cm specimens. The Bridged Crack Model analysis has been performed by implementing both the yielding (red) and slippage (black) constitutive law to the fiber reinforcement.

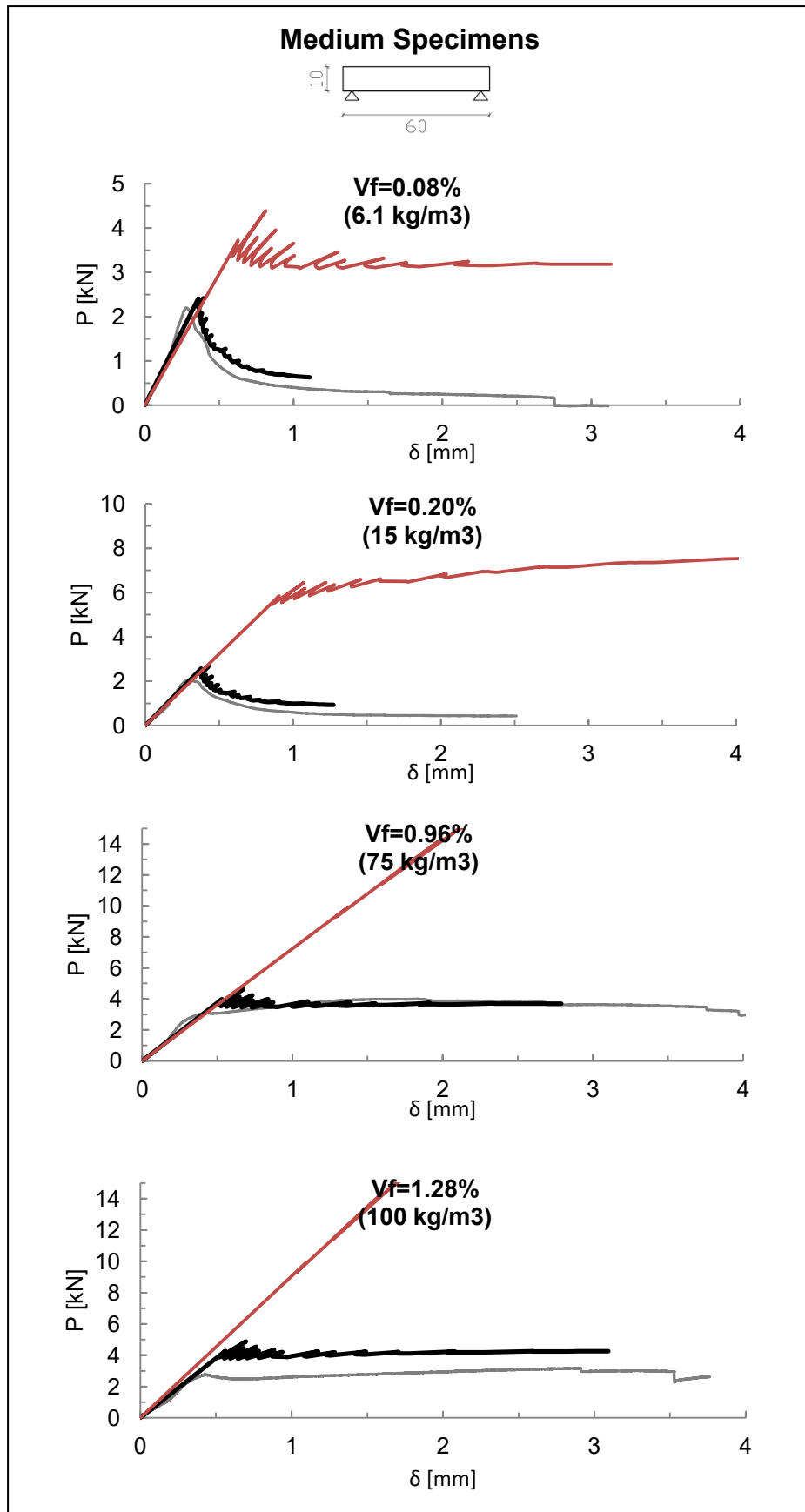


Figure 3.9: Experimental (grey) versus analytical results from bending tests on 10x10x60 cm specimens; The Bridged Crack Model analysis has been performed by implementing both the yielding (red) and slippage (black) constitutive law to the fiber reinforcement

3.3 Discussion and conclusions

The main issue during the test campaign design was understand which one constitutive law should be assigned to the steel fibers.

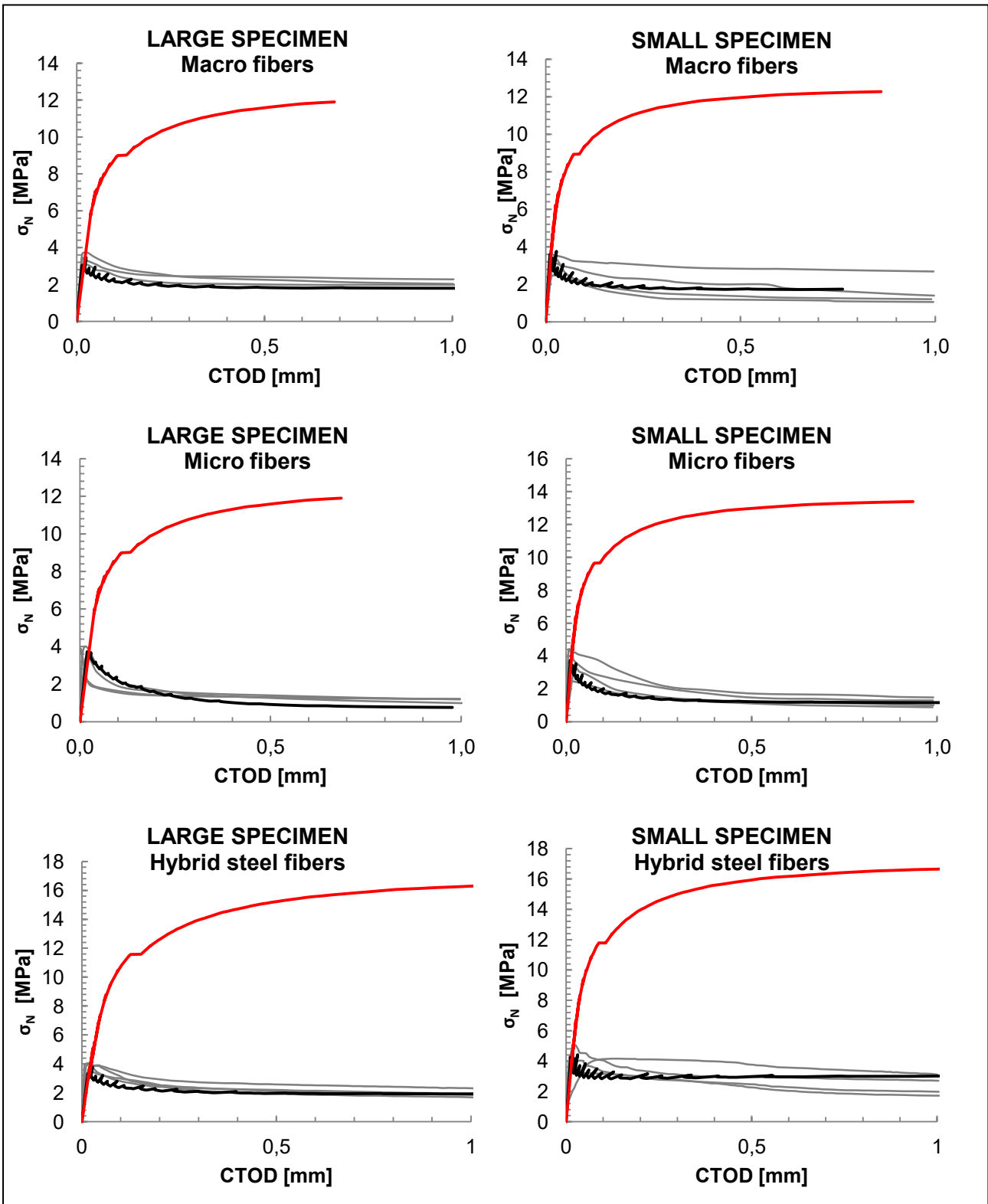


Figure 3.10: Comparison of Plizzari experimental tests (grey), Bridged Crack analysis employing the slippage law (black) and Bridged Crack analysis employing the yielding law (red)

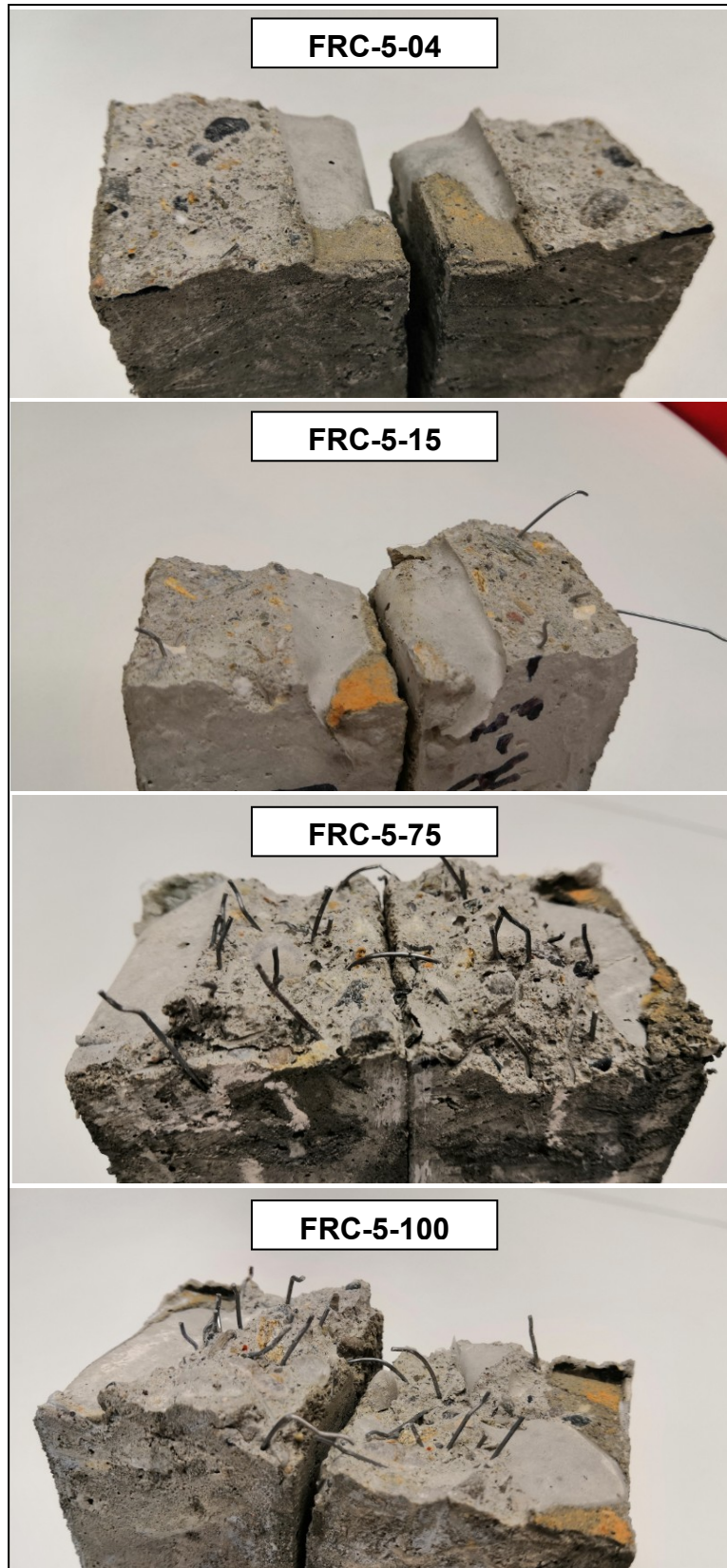


Figure 3.11: Detail of the fracture surface for specimens 5x5x30 cm at the end of the three-point bending test

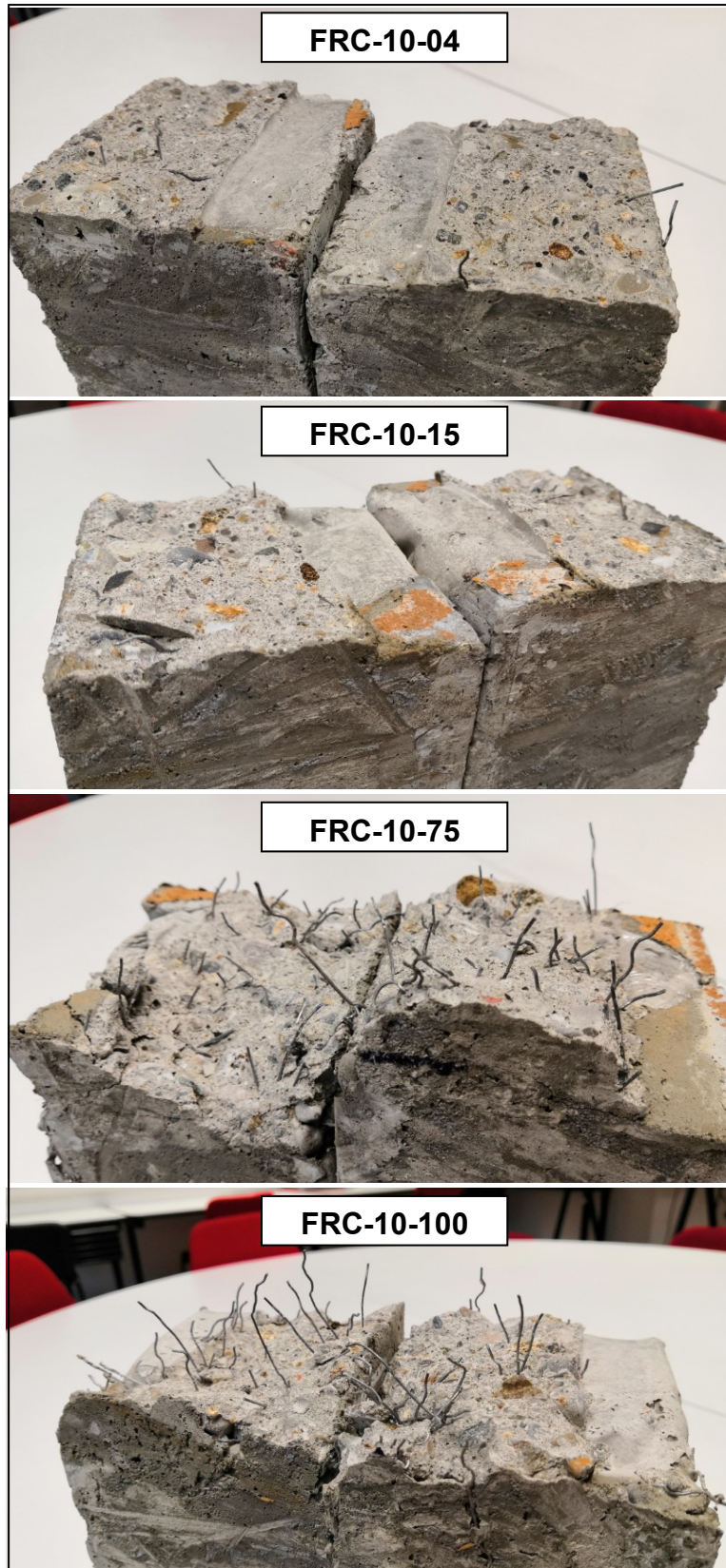


Figure 3.12: Detail of the fracture surface for specimens 10x10x60 cm at the end of the three-point bending test

Fundamental for this purpose was the check with Plizzari experimental results, from which seemed clear that the slippage law mastered the problem Fig. (3.10).

Nevertheless there was always the unknown factor linked to the shape of the MX-500 fibers used in this experimental campaign, because they were designed to improve the grip. In the end, the fiber contents were chosen in such a way as to obtain significant results, whatever the fibers failure mechanism. But, as with Plizzari et al., the slippage law best approximate the experimental results obtained in this master thesis work, see Figs. (3.8) and (3.9) whereas the red curves have been obtained by the Bridged Crack Model in case of yielding of the fiber reinforcement. This finding was also reinforced from watching the specimen fracture surface at the end of the three-point bending tests, in Fig. (3.11) and (3.12) shows the fracture surface of the tested specimens. It can be clearly seen that the fibers were intact.

One should remember that the algorithm presented in this paper implements a simplification of the pull-out law proposed by Model Code 2010, (Fig. 3.13), as mentioned in [1.3.1]. Therefore the implementation of a constitutive slippage law more refined could cover further developments.

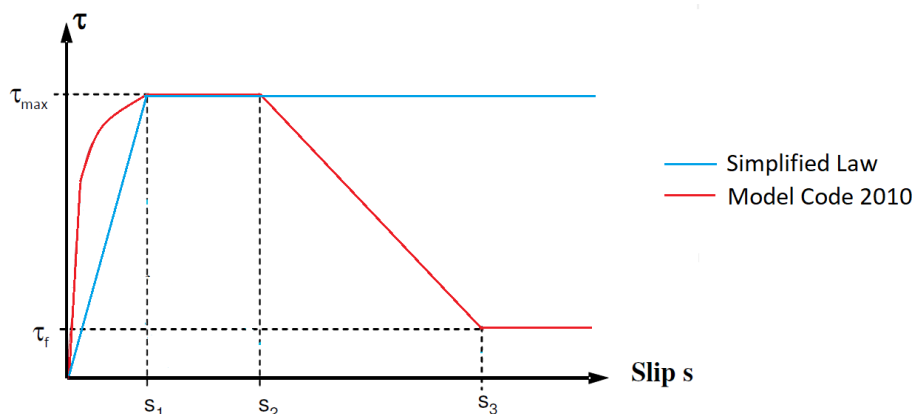


Figure 3.13: Model Code 2010 constitutive law versus rigid-perfectly plastic simplified slippage law implemented in the Bridged Crack algorithm

3.4 Concluding remarks

In conclusion, this study investigated the effects of fiber content and dimensional scale on the bending fracture behavior of FRC. The results can be summarised as follows:

- The slippage between the matrix and the reinforcement was the failure mechanism in all cases investigated in this paper
- There is a clear transition in the failure phenomena from brittle to ductile as the fiber content increases
- Using a yielding constitutive law for the fiber, when the structural size decreases the percentage of fibers, ρ , to get the minimum reinforcement increases. This can be explained by the Brittleness Number (Eq. 1.71)

- In the load versus deflection diagram, the load peak moves up and to the right when K_{IC} increases. At the same time, the asymptotic behavior doesn't change. In the case of strong hardening behavior, the role played by K_{IC} is negligible
- Load peak and asymptote move up when f_y (or τ) increases
- For $m > 20$, the condition of complete diffusion of the fibers is represented ($m = \infty$). N_p value involving a ductile-to-brittle transition depends on the initial crack length a (concrete cover). i.e. for $m > 20$: when $a/h \cong 0.1$, we get $N_p = 1.3$; when $a/h \cong 0.3$, we get $N_p = 0.8$.
- When the initial crack length, a , is small compared to the beam height, h , the global structural behavior is brittle. Consequently, the ductile-to-brittle transition arises for high values of N_p , and hence also of ρ . On the other hand, when a is large, the structural behavior appears to be ductile. Consequently, the ductile-to-brittle transition arises for low values of N_p . In conclusion, we need to set an initial crack length larger than $\frac{1}{4} \div \frac{1}{3} h$ in order to have a ductile behavior.

References

- Agrawal, G.L., Tulin, L.G., Gerstle, K.H. (1965) "Response of Doubly Reinforced Concrete Beams to Cyclic Loading", *ACI Journal*, 62: 823-834.
- Ballarini, R., Muju, S. (1991) "Stability Analysis of Bridged Cracks in Brittle Matrix Composites", *ASME Paper*, 91-GT-094.
- Ballarini, R., Shah, S. P., and Keer, L. M. (1984) "Crack Growth in Cement Based Composites", *Engineering Fracture Mechanics*, 20: 433–445.
- Barenblatt, G. I. (1962) "The Mathematical Theory of Equilibrium Cracks in Brittle Fracture", *Adv. Appl. Mech.*, 7: 55–129.
- Bosco, C., Carpinteri, A. (1992) "Fracture behavior of beam cracked across reinforcement", *Theoretical and Applied Fracture Mechanics*, 17:61-68.
- Bosco, C., Carpinteri, A. (1995) "Discontinuous constitutive response of brittle matrix fibrous composites", *Journal of the Mechanics and Physics of Solids*, 43:261-274
- Bosco, C., Carpinteri, A., Debernardi, P.G. (1990a) "Fracture of reinforced concrete: Scale effects and snap-back instability", *Engineering Fracture Mechanics*, 35:665-677.
- Bosco, C., Carpinteri, A., Debernardi, P.G. (1990b) "Minimum reinforcement in high strength concrete", *Journal of Structural Engineering (ASCE)*, 116:427-437.
- Budiansky, B., Hutchinson, J. W., Evans, A. G. (1986) "Matrix Fracture in Fiber-Reinforced Ceramics", *J. Mech. Phys. Solids*, 34: 167–189.
- Cachim, P.B., Figueiras, J.A., Pereira, P.A.A. (2002) "Numerical modelling of fibre-reinforced concrete fatigue in bending", *International Journal of Fatigue*, 24: 381-387
- Carpinteri, A. (1981) "A fracture mechanics model for reinforced concrete collapse", *Proceedings of the I.A.B.S.E. Colloquium on Advanced Mechanics of reinforced Concrete*, Delft, pp. 17-30
- Carpinteri, A. (1984a) "Interpretation of the Griffith instability as a bifurcation of the global equilibrium", *Proceedings of the N.A.T.O. Advanced Research Workshop an Application of Fracture Mechanics to Cementitious Composites*, 287-316.
- Carpinteri, A. (1984b) "Stability of fracturing process in RC beams", *Journal of Structural Engineering (ASCE)*, 110: 544-558.
- Carpinteri, A. (1986) "Mechanical Damage and Crack Growth in Concrete: Plastic Collapse to Brittle Fracture", *Martinus Nijhoff, Dordrecht*.
- Carpinteri, A. (1988) "Snap-back and hyperstrength in lightly reinforced concrete beams", *Magazine of Concrete Research*, 40:209-215.

- Carpinteri, A. (1989a) "Post-peak and post-bifurcation analysis of cohesive crack propagation", *Engineering Fracture Mechanics*, 32:265-278.
- Carpinteri, A. (1989b) "Cusp catastrophe interpretation of fracture instability", *Journal of the Mechanics and Physics of Solids*, 37: 567-582.
- Carpinteri, A. (1992) "Reinforced Concrete Beam Behavior under Cyclic Loadings", In Al. Carpinteri, editor, *Applications of Fracture Mechanics to Reinforced Concrete*, Elsevier Applied Science, London and New York, pp. 547-578
- Carpinteri, A. (1999) "Nonlinear Crack Models for Nonmetallic Materials", Kluwer Academic Publishers, Dordrecht, The Netherlands.
- Carpinteri, A., Carpinteri, An. (1984) "Hysteretic behavior of RC beams", *Journal of Structural Engineering (ASCE)*, 110: 2073–2084.
- Carpinteri, A., Colombo, G. (1989) "Numerical analysis of catastrophic softening behaviour (snap-back instability)", *Computers and Structures*, 31: 607–636.
- Carpinteri, A., Corrado, M., Paggi, M., Mancini, G. (2009) "New model for the analysis of size-scale effects on the ductility of reinforced concrete elements in bending", *J. Eng. Mech.*, 135, 221-229.
- Carpinteri, A., Massabò, R. (1996) "Bridged versus cohesive crack in the flexural behavior of brittle-matrix composites", *International Journal of Fracture*, 81: 125-145.
- Carpinteri, A., Massabò, R. (1997a) "Continuous vs discontinuous bridged crack model of fiber-reinforced materials in flexure", *International Journal of Solids and Structures*, 34: 2321-2338.
- Carpinteri, A., Massabò, R. (1997b) "Reversal in failure scaling transition of fibrous composites", *Journal of Engineering Mechanics (ASCE)*, 123: 107-114.
- Carpinteri, A., Puzzi, S. (2003) "Hysteretic flexural behaviour of brittle matrix fibrous composites: the case of two fibers", *Proc. of 16th National (Italian) Congress of Theoretical and Applied Mechanics (AIMETA)*, CD-ROM, File 102, Ferrara.
- Carpinteri, A., Puzzi, S. (2004) "The Bridged Crack Model for the Analysis of FRC Elements Under Repeated Bending Loading," *Fibre-Reinforced Concretes*, Proc. of 6th RILEM Symposium on Fibre Reinforced Concrete, Varenna, Italy, R.I.L.E.M. Publications S.a.r.l., Bagneux, M. Di Prisco, R. Felicetti, and G. A. Plizzari, eds., pp. 767–776.
- Carpinteri, A., Puzzi, S. (2007) "The bridged crack model for the analysis of brittle matrix fibrous composites under repeated bending loading", *Journal of Applied Mechanics*, 74: 1239-1246.

- Carpinteri, An., Spagnoli, A., Vantadori, S. (2004) "A fracture mechanics model for a composite beam with multiple reinforcements under cyclic bending", *International Journal of Solids and Structures*, 41: 5499-5515.
- Carpinteri, An., Spagnoli, A., Vantadori, S. (2005) "Mechanical Damage of Ordinary or Prestressed Reinforced Concrete Beams Under Cyclic Bending," *Eng. Fract. Mech.*, 72, pp. 1313–1328.
- Carpinteri, An., Spagnoli, A., Vantadori, S. (2006) "An elastic-plastic crack bridging model for brittle-matrix fibrous composite beams under cyclic loading", *International Journal of Solids and Structures*, 43: 4917-4936.
- Cotterell, B., Paravasivam, P., Lam, K. Y. (1992) "Modelling the Fracture of Cementitious Composites," *Mater. Struct.*, 25, pp. 14–20.
- Cox, B. N. (1991) "Extrinsic Factors in the Mechanics of Bridged Cracks," *Acta Metall. Mater.*, 39: 1189–1201.
- Cox, B. N., Marshall, D. B. (1991a) "Crack Bridging in the Fatigue of Fibrous Composites," *Fatigue Fract. Eng. Mater. Struct.*, 14: 847–861.
- Cox, B. N., Marshall, D. B. (1991b), "Stable and Unstable Solutions for Bridged Cracks in Various Specimens," *Acta Metall. Mater.*, 39: 579–589.
- Dugdale, D. S. (1960), "Yielding of Steel Sheets Containing Slits," *J. Mech. Phys. Solids*, 8: 100–104.
- Erdogan, F., Joseph, P. F. (1987) "Toughening of Ceramics Through Crack Bridging by Ductile Particles," *J. Mech. Phys. Solids*, 35: 262–270.
- Foot, R. M. L., Mai, Y. W., Cotterell, B. (1986) "Crack Growth Resistance Curves in Strain-Softening Materials," *J. Mech. Phys. Solids*, 6: 593–607.
- Guinea, G.V., Pastor, J.Y., Planas, J., Elices, M. (1998) "Stress intensity factor, compliance and CMOD for a general three-point-bend beam", *International Journal of Fracture*, 89: 103-116.
- Hillerborg, A. (1980) "Analysis of Fracture by Means of the Fictitious Crack Model, Particularly for Fibre Reinforced Concrete," *Int. J. Cem. Comp.*, 2: 177–184.
- Hillerborg, A., Modeer, M., and Petersson, P. E. (1976) "Analysis of Crack Formation and Crack Growth in Concrete by Means of Fracture Mechanics and Finite Elements," *Cem. Concr. Res.*, 6: 773–782.
- Jenq, Y. S., Shah, S. P. (1985) "A Two-Parameter Fracture Model for Concrete," *J. Eng. Mech.*, 111: 1227–1241.
- Li, V. C., Liang, E. (1986) "Fracture Processes in Concrete and Fiber Reinforced Cementitious Composites," *J. Eng. Mech.*, 112: 566–586.

- Mai, Y. W. (1991) "Fracture and Fatigue of Non-transformable Ceramics: The Role of Crack-Interface Bridging," *Fracture Processes in Concrete, Rock and Ceramics*, J. G. M. Van Mier, ed., E.&F.N. Spon, London, pp. 3–26.
- Marshall, D. B., Cox, B. N. (1987) "Tensile Fracture of Brittle-Matrix Composites: Influence of Fiber Strength," *Acta Metall.* 35: 2607–2619.
- Marshall, D. B., Cox, B. N., Evans, A. G. (1985) "The Mechanics of Matrix Cracking in Brittle Matrix Fiber Composites," *Acta Metall.*, 33: 2013–2021.
- Massabò, R. (1993) "Meccanismi di rottura nei materiali fibrorinforzati", PhD. Thesis, Scuola di Dottorato, Politecnico di Torino.
- Matsumoto T., Li V.C. (1999) "Fatigue life analysis of fiber reinforced concrete with a fracture mechanics based model", *Cement and Concrete Composites*, 21: 249-261
- Milne, I., Ritchie, R.O., Karihaloo, B. (2003) *Comprehensive structural integrity: fracture of materials from nano to macro / eds. in chief I. Milne, R.O. Ritchie and B. Karihaloo* Amsterdam: Elsevier
- Murakami, Y. (1987) *Stress Intensity Factors Handbook*, Pergamon Press, Oxford.
- Paris, P. C., Erdogan, F. (1963) "A Critical Analysis of Crack Propagation Laws," *ASME J. Basic Eng.*, 85: 528–534.
- Paris, P. C., Sih, G. C. (1965) "Stress analysis of cracks", *Fracture Toughness Testing and its Applications*, ASTM STP, 381:30-81.
- Petersson, P. E. (1981) "Crack Growth and Development of Fracture Zones in Plain Concrete and Similar Materials," Ph.D. thesis, Lund. Institute of Technology, Lund, Denmark.
- Puzzi, S. (2004) "Mechanics of grained or fibrous heterogeneous materials", PhD. Thesis, Scuola di Dottorato, Politecnico di Torino.
- Reis, J. M. L., Ferreira, A. J. M. (2003) "Fracture Behaviour of Glass Fiber Reinforced Polymer Concrete," *Polym. Test.*, 22: 149–153.
- Rich, T. P., Cartwright, D. J. (1977). *Case studies in fracture mechanics* (No. AMMRC-MS-77-5). Army Materials And Mechanics Research Center Watertown Ma.
- Ruiz, G. (2001) "Propagation of a Cohesive Crack Crossing a Reinforcement Layer," *Int. J. Fract.*, 111: 265–282.
- Shah, S. P. (1988) "Fracture Toughness of Cement-Based Materials," *Mater. Struct.*, 21: 145–150.
- Sinclair, G.B., Messner, T.W., Meda, G. (1996) "Stress intensity factors for deep edge cracks in bending", *Engineering Fracture Mechanics*, 55: 19-24.

- Tada, H., Paris, P.C., Irwin, G. (1985) *The Stress Analysis of Cracks*, Paris Productions Incorporated (and Del Research Corporation), St. Louis, Missouri.
- Visalvanich, K., Naaman, A. E. (1983) "Fracture Model for Fiber Reinforced Concrete," *ACI J.* 80: 128–138.
- Wecharatana, M., Shah, S. P. (1983) "A Model for Prediction of Fracture Resistance of Fiber Reinforced Concrete," *Cem. Concr. Res.*, 13: 819–829.
- Wilson, W. K. (1970) "Stress intensity factors for deep cracks in bending and compact tension specimens", *Engineering Fracture Mechanics*, 2: 169-171.
- Zhang J., Stang H., Li V.C. (1999) "Fatigue life prediction of fiber reinforced concrete under flexural load", *International Journal of Fatigue*, 21: 1033-1049
- Zhang J., Stang H., Li V.C. (2001) "Crack bridging model for fibre reinforced concrete under fatigue tension", *International Journal of Fatigue*, 23: 655-670
- Zhang, J., Li, V. C. (2004) "Simulation of Crack Propagation in Fiber-Reinforced Concrete by Fracture Mechanics", *Cem. Concr. Res.*, 34: 333–339.
- Sorelli, L. G., Meda A., Plizzari G. A. (2005) "Bending and Uniaxial Tensile Tests on Concrete Reinforced with Hybrid Steel Fibers", *Journal of Materials in Civil Engineering*
- Carpinteri, A., Cadamuro, E., Ventura, G. (2015) "Fiber-reinforced concrete in flexure: a cohesive/overlapping crack model application", *Materials and Structures*
- Swamy, R.N., Al-Ta'an, S. A. (1981), "Deformation and ultimate strength in flexure of reinforced beams made with steel fibre concrete", *Journal of the American Concrete Institute*
- Olivito, R.S., Zuccarello, F.A. (2009), "An experimental study on the tensile strength of steel fiber reinforced concrete", *Composites: Part B*, 41: 246:255
- Kang, S.T. , Lee, Y., Park, Y.D., Kim, J.K. (2009), "Tensile fracture properties of an Ultra High Performance Fiber Reinforced Concrete (UHPFRC)", *Composites Structures*, 92: 61-72